SUMMER ATMOSPHERIC HEAT SOURCES OVER THE TIBETAN PLATEAU

A DISSERTATION SUBMITTED TO THE
GRADUATE DIVISION OF THE
UNIVERSITY OF HAWAI‘I AT MĀNOA
IN PARTIAL FULFILLMENT OF THE
REQUIREMENTS FOR THE DEGREE OF

DOCTOR OF PHILOSOPHY

IN

ATMOSPHERIC SCIENCES

December 2021

By

Zhiling Xie

Dissertation Committee:
Bin Wang, Chairperson
Tim Li
Fei-Fei Jin
Christina Karamperidou
Niklas Schneider

ACKNOWLEDGEMENTS

Throughout the work of this dissertation, I have received a great deal of assistance. I would first like to express my sincere gratitude to my advisor, Prof. Bin Wang, for his dedicated guidance and continuous support. I appreciate his patience and encouragement during my Ph.D. study. I would like to thank my committee members, Professors Tim Li, Fei-Fei Jin, Christina Karamperidou, and Niklas Schneider, for their time devoted and their insightful comments and suggestions on this dissertation. Many thanks also go to the members of Prof. Wang's research group and my colleagues in the Department of Atmospheric Sciences for their generous sharing, beneficial discussion, and kind help. Lastly, I am deeply grateful to my family for their unwavering support and belief in me.

ABSTRACT

The spatial-temporal characteristics of the summer atmospheric heat sources over the Tibetan Plateau (TP) are revisited in the first part of this dissertation, applying various bias-corrected datasets, including reanalyses, gauge observations, and satellite products. Verification-based selection and ensemble-mean methods are taken to combine multiple datasets. Compared to previous studies focused on the eastern TP, this study pays special attention to the heat sources over the data-void western plateau. A climatological minimum in the total heat is found in the high-altitude region of the northwestern TP. The TP total heat showed insignificant trends over the eastern and central TP (ETP/CTP) during 1984–2006, whereas exhibited an evident increasing trend over the western TP (WTP). The interannual variation of total heat over the central-eastern TP is dominated by the variation of latent heat from precipitation. However, over the western TP, the variation of the total heat is highly correlated with net radiation and surface sensible heat.

The remote forcings and impacts of the interannual variations in summer heat sources over the eastern, central, and western TP are investigated in the second and third parts with observational analyses and numerical model experiments. The summer heat source variability is affected by different remote forcings across the TP from east to west. The ETP precipitation (i.e., latent heating) is likely modulated by North Atlantic Oscillation (NAO) and associated SST anomalies through large-scale wave trains propagating from Western Europe to East Asia. On the other hand, the increased CTP precipitation is primarily driven by a developing La Niña through generating southerly wind anomalies to the south of the CTP, enhancing moisture transport and precipitation over the southern CTP. The increased WTP sensible heating is linked to the tropical western Pacific cooling, central Pacific warming, and North Atlantic cooling. These anomalous SST conditions produce a high-pressure anomaly over the WTP, raising the ground-air temperature difference, thereby enhancing the WTP sensible heat.

The results in the third part show that the ETP, CTP, and WTP heat sources have different impacts on regional climate and teleconnection. A warming center in northwestern Asia and a cooling center in western Europe are connected with the ETP heating. The CTP heating is related to northeastern Asian warming and East Asia cooling. The WTP heating is linked to the warming in southeastern China and the polar region of Asia. The linear wave-train responses to the TP heating forcings exhibit notable differences. The ETP heating generates an upper-level wave train propagating eastward to the northwestern Pacific. The wave train excited by the CTP heating propagated far eastward to central North Pacific. The WTP heating produces a wave train that splits into two branches, the northern one propagating northeastward to the Arctic region and the southern one propagating eastward to coastal northwestern Pacific.

The fourth part of this dissertation presents 22 CMIP6 models' performances and future projections for the eastern-TP summer precipitation and sensible heat flux. Nearly all models can well simulate the observed climatological precipitation pattern (1979–2014) but overestimate the mean by 65%. For sensible heat, nearly half of the models can hardly capture the spatial structure. The multimodel ensemble mean of selected high-performance models projects that, under the medium emission scenario (SSP2-4.5), the summer precipitation will likely increase by 2.7% per degree Celsius global warming due to the future enhancement in surface evaporation and vertical moisture transport that are partially offset by weakening ascending motion. The projected sensible heat will likely remain unchanged, associated with the likely unaltered surface wind speed.

TABLE OF CONTENTS

LIST OF TABLES

LIST OF FIGURES

LIST OF ABBREVIATIONS

TP	Tibetan Plateau
WTP/CTP/ETP	Western TP/ Central TP/ Eastern TP
TH	Total Heat source
SH	Sensible Heat flux at surface
LH	Condensational Latent Heat from precipitation
RD	Net Radiation flux
JJA	June-July-August
SST	Sea Surface Temperature
SSTA	Sea Surface Temperature Anomaly/Anomalies
NAO	North Atlantic Oscillation
ENSO	El Niño-Southern Oscillation
MC	Maritime Continent
WP	Western Pacific
CP	Central Pacific
TNA	Tropical North Atlantic
AGCM	Atmospheric General Circulation Model
CAM4	Community Atmosphere Model version 4
LBM	Linear Baroclinic Model
CMIP5/CMIP6	Coupled Model Intercomparison Project – Phase 5/6
PCC	Pattern Correlation Coefficient
NRMSE	Normalized Root-Mean-Square Error

Chapter 1. Introduction

The Tibetan Plateau (TP), also named the Qinghai-Xizang Plateau in China, stands over central-eastern Asia, covering about one-quarter of the entire territory of China (Fig. 1.1). It is the world's highest and largest plateau above sea level, with an average elevation exceeding 4000 m and an area of 2.5 million km^2. The TP is known as the "Roof of the World", being surrounded by massive mountain ranges with the world's two highest summits, Mount Everest and K2. The plateau is bordered to the south by the Himalayas, to the north by the Kunlun Mountains, and to the northeast by the Qilian Mountains. The TP is a critical region for the Asian hydrological cycle. It contains great glaciers and supplies headwaters of the major rivers in Asia, including the Yangtze, Yellow, Mekong, Brahmaputra, Ganges and Indus rivers. The TP is sometimes called the "Third Pole" because its ice fields contain the largest freshwater reserve outside the polar regions.

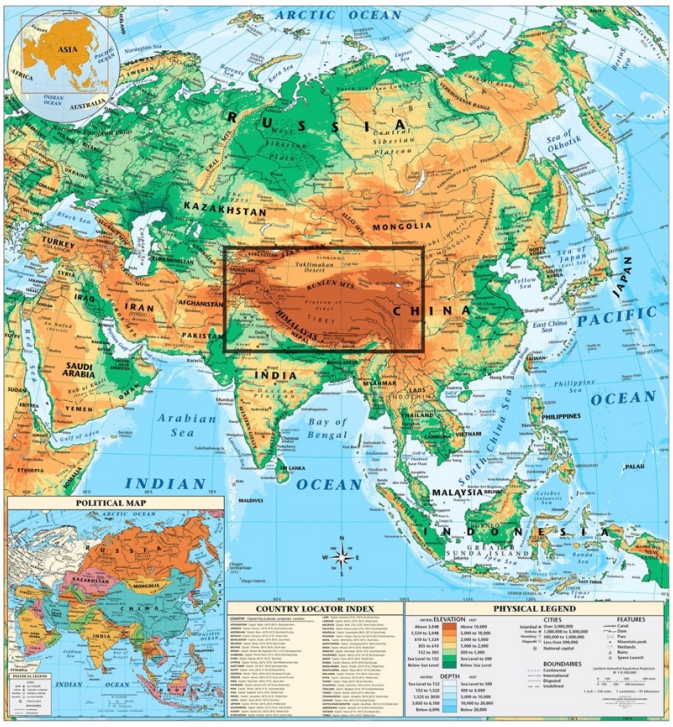

Fig. 1.1. Physical map of Asia for geography (downloaded from https://roundtripticket.me/). The black rectangular frame denotes the location of the Tibetan Plateau.

1.1. Mechanical and Thermal Effects of the Tibetan Plateau

The TP, a high and huge terrain located in the subtropical westerly jet in winter and between the westerly winds to the north and easterlies to the south in summer, has a great impact on atmospheric circulation. Mechanically the TP, posing a physical obstacle, can block atmospheric flows, split the wintertime westerlies into the northern and southern branches, and thus favors the generation of the Great Trough over East Asia (Yeh 1950; Bolin 1950). In the downstream of the plateau, the north and south branches of the westerly merge into one jet stream, becoming the strongest in the World (Koo 1951). The TP also has a crucial effect on lee cyclogenesis and associated northerly cold surges in winter (Murakami and Nakamura 1983). The TP serves as a giant barrier that blocks cold outbreaks from the north and confines the winter monsoon to eastern and southern Asia (Chang et al. 2006).

Using then available observations, Yeh et al. (1957) calculated each term of the heat budget equation and found that the TP is a weak heat sink in winter but a large heat source in summer. In the same year, Flohn (1957) also discovered the summer heating nature of the TP. The mean TP altitude lies above 40% of the atmosphere. While the TP receives strong solar radiation at the surface, the other parts of Asia at such a level are in the cold middle troposphere. The elevated summer heat sources over the TP profoundly influence atmospheric circulation and regional-to-global weather and climate. Early researches mainly focus on the roles of the TP heat source in climatological mean circulations. The TP heating helps maintain the Tibetan or South Asian High (Flohn 1981; Zhang et al. 2002) and form a strong upper-tropospheric negative vorticity source (Ye and Wu 1998; Liu et al. 2001) in summer. The TP heat source also serves as a huge air pump driven by the surface sensible heating over the TP (Wu et al. 1997, 2004) and contributes substantially to the Asian monsoon onset and the abrupt seasonal transition (Li and Yanai 1996; Ueda and Yasunari 1998; Wu and Zhang 1998).

1.2. Interannual Variations in Summer Heat Sources over the Tibetan Plateau

Recent studies pay more attention to the striking impacts of the interannual variations in the TP heat source on circulation and precipitation (e.g., Zhao and Chen 2001; Wang et al. 2014; Hu and Duan 2015). Chen et al. (2015) found a linkage between the year-to-year evolution of summer diabatic heating over the TP and the deep convection over eastern China with the downstream moisture transport. Duan et al. (2017) suggested that the surface sensible heating over TP influenced the interannual variation of the western Pacific subtropical high. Through a modeling study, Lu et al. (2018) showed that the TP surface heating could also affect the 'upstream' climate over West Asia, North Africa, South Europe, and North Atlantic through the intensified and westward-extended South Asian High. Moreover, some authors used the snow cover or snow depth on the TP as a proxy of the thermal condition of the TP, especially the western TP (WTP), to investigate the climate effects of its variability (e.g., Y.-S. Zhang et al. 2004). Z. Wu et al. (2016) discovered that the WTP snow cover in summer could influence the interannual variations of summer heatwave frequencies over Eurasia through a southern Europe-northeastern Asia (SENA) teleconnection. Xiao and Duan (2016) demonstrated that the winter or spring snow cover anomalies over the WTP and the Himalayas could last until summer and further influence the East Asia summer rainfall variability by modulating the moisture transport to Eastern China. In contrast to the widely known role of the central-eastern (CE)-TP heat sources in Asian summer monsoon system (e.g., Gao et al. 1981, Yanai et al. 1992, Ye and Wu 1998, Hsu and Liu 2003, Rajagopalan and Molnar 2013, Z. Wang et al. 2016), the distinct importance of the WTP heating in the climate system has been recently documented but remains poorly understood. Therefore, it is critical to distinguish the effects of WTP heating from CE-TP heating for evaluating climate models and further improving climate prediction.

Compared to the major focus on the impacts of the TP thermal forcing, much less attention has been paid to the origins of the variability of the TP heating. The North Atlantic Oscillation (NAO) is considered to be one important source for the precipitation variability over the TP at the interannual timescale (Liu and Yin, 2001; Z. Wang et al. 2018). During the latest decade, more studies have worked on finding the controlling factors. Bothe et al. (2010) found a linkage between positive (negative) El Nino/Southern Oscillation and Indian Ocean Dipole episodes and the extreme dryness (wetness) over the TP. Cui et al. (2015) found that the North Atlantic sea surface temperature anomaly in early spring could change the spring wind speed and circulation over the TP through the eastward propagation of Rossby waves and thus influence the in-situ sensible heat variability. Jiang et al. (2016) pointed out that the convection around the western Maritime Continent could modulate the interannual variation of summer LH over the southeastern TP. Dou et al. (2017) found that the May Southern Hemisphere annular mode exhibits a significant positive relationship with the interannual variations in the WTP snow cover during summer through both atmospheric bridge and oceanic bridge. Considering that each previous study always focused on one or two factor(s) that influence the TP heating and few works separately studied the origins for the ETP, CTP, and WTP heating, it is our interest to find possible different remote forcings for the interannual variations of the ETP, CTP, and WTP summer heat sources.

1.3. Climate Change on the Tibetan Plateau

As the “Third Pole” in the world, the TP is particularly sensitive to climate change (Liu and Chen 2000; Cheng and Wu 2007; Yao et al. 2019). Wang et al. (2008) found that the surface temperature on the CE-TP increased by 1.8 °C during 1960–2007, and the TP surface warming can enhance the frontal rainfall in East Asia through two Rossby wave trains and an isentropic uplift to the east of the TP. Besides, the reduction in the TP sensible heating connected with the TP

tropospheric warming can regulate summer rainfall changes over eastern China and weaken the East Asian summer monsoon circulation (Duan and Wu 2009; Duan et al. 2013).

Due to the notable impacts of climate change on the TP, it is critical to understand how the TP heat sources will change in the future. General circulation models (GCMs) are the primary tools for projecting future climate change. The Coupled Model Intercomparison Project (CMIP) makes plentiful standardized model outputs publicly available, considerably facilitating multimodel analyses. Previous works found that both surface air temperature and precipitation are projected to increase over the TP under the CMIP5 RCP-based scenarios in the 21st century (Su et al. 2013; Chen and Frauenfeld 2014a, b; Jia et al. 2019a, b). However, much less attention has been directed at the projection of the surface sensible heat over the TP. Moreover, few studies have further explored what factors contribute to the future change of both precipitation (i.e., condensational latent heat) and sensible heat over the TP. Therefore, the future projections of the TP summer heat sources with the contributors to those future changes need to be further examined using the newest CMIP6 model products.

1.4. Research Goals and Scientific Questions

Our further understanding of the TP thermal forcing is hampered by the sparseness and the lack of observational data over the complex topography, especially over the western TP. To accurately quantify the summer heat sources is still a major topic of TP meteorology. Early works using short-term experimental data or only one set of reanalysis data have great uncertainty in the TP heat source diagnostics (Yanai et al. 1992; Zhao and Chen 2001; Duan and Wu 2005). Recent studies utilized the relatively long-term station data (Duan and Wu 2008; Yang et al. 2011), but the surface observation stations on the TP cannot cover the entire plateau region; in particular, stations are scarce in the WTP. Existing research works have shown the considerable differences between

heat sources over the eastern TP and the western TP (Luo and Yanai 1984; Wu et al. 2007; Chen et al. 2015; Jiang et al. 2016). Thus, it is necessary to investigate their characteristics separately using a reliable dataset covering the whole plateau.

The major goals of this dissertation are (1) to develop a new dataset of summer heat sources over the entire TP region (Chapter 2), (2) to explore the origins and impacts of the interannual variations in the western, central, and eastern-TP heat sources (Chapter 3 and 4), and (3) to investigate the future changes of the TP heat sources (Chapter 5). Specific questions addressed in each chapter are described below.

In Chapter 2: Are the summer climatology patterns and long-term trends of the WTP heat sources different from those of the CE-TP heat sources? What are the possible causes for those differences?

In Chapters 3 and 4: Are the origins and impacts of the interannual variations in the WTP heat sources different from those of the interannual variations in the CE- TP heat sources? How do those remote forcings regulate the variations of the TP heat sources, and how do the TP heat sources influence the circulation and climate?

In Chapter 5: Are the performance of CMIP6 models on the TP heat sources significantly improved compared to CMIP5 models? What are the future changes of the TP heat sources, and what are the contributors to those changes?

Chapter 2. An Integrated Analysis of Summer Heat Sources over the Entire Tibetan Plateau Region

2.1. Abstract

Multiple bias-corrected top-quality reanalysis datasets, gauge-based observations, and selected satellite products are synthetically employed to revisit the climatology and variability of the summer atmospheric heat sources over the Tibetan Plateau (TP). Verification-based selection and ensemble-mean methods are utilized to combine various datasets. Different from previous works, this chapter pays special attention to estimating the total heat source (TH) and its components over the data-void western plateau (70° - 85°E), including the surface sensible heat (SH), latent heat released by precipitation (LH), and net radiation flux (RD).

Consistent with previous studies, the climatology of summer SH (LH) typically increases (decreases) from southeast to northwest. Generally, LH dominates TH over most of the TP. A notable new finding is a minimum TH area over the high-altitude region of the northwestern TP, where the Karakoram Mountain Range is located. It is found that during the period of 1984-2006, TH shows insignificant trends over the eastern and central TP, whereas exhibits an evident increasing trend over the western TP that is attributed to the rising tendency of LH before 1996 and that of RD after 1996. The year-to-year variation of TH over the central-eastern TP is highly correlated with that of LH, but that is not the case over the western TP where the TH is significantly correlated with RD and SH. It is also worth noting that the variations of TH in each summer month are not significantly correlated with each other, suggesting remarkable subseasonal variations in the TP heat sources.

2.2. Introduction

The total heat source (TH) is a physical quantity used to express the diabatic heating in an air column. For a given location, an atmospheric TH is the net heat gain or loss within a given period. It is therefore defined as the sum of three components (Yanai et al. 1973; Luo and Yanai 1984; Duan and Wu 2008): local surface sensible heat flux transferred to the atmosphere from land or ocean surface (SH), latent heat released to the atmosphere by total precipitation (LH), and net radiation flux of the air column (RD). Variations of different components are associated with distinct land and atmospheric processes.

Much effort has been devoted to investigating the vertical structure, spatial pattern and temporal variation of atmospheric heat sources over the TP (e.g., Wang et al. 2012; Zhu et al. 2012; Shi and Liang 2014). Luo and Yanai (1984) calculated the vertical profiles of apparent heat source (Q_1) and moisture sink (Q_2) over the WTP and the eastern TP (ETP) in June and found that the diabatic heating is intense in the surface layer over the WTP, while almost half of the ETP heating is contributed by latent heat release. Showing the spatial pattern of July climatological heat sources over the TP, Duan and Wu (2005) indicated that LH is dominant over the central, southern and eastern TP, while SH is comparable to LH over the WTP, and intensity of radiative cooling exceeds that of SH over the main body of the plateau. Wu et al. (2007) studied the seasonal evolution of thermal forcing over the TP. They found that LH is significant in summer and becomes much weaker in autumn and winter, while the near-surface SH is still very strong, thus the shape of the TH profile follows that of SH quite well in all seasons. Recent works paid more attention to the interannual variations of TH and its components over the TP. Chen et al. (2015) investigated the year-to-year evolution of vertically integrated Q_1 and Q_2 over the TP and eastern China, and they suggested that the deep convection over eastern China is linked with the convection over the ETP through downstream moisture transportation. Using a set of state-of-the-art estimations of the heat

sources in the period of 1984-2004 developed by Yang et al. (2011), Jiang et al. (2016) also studied the interannual variation of summer heat sources over the station-covered TP region. They pointed out that the convection around the western Maritime Continent could modulate summer TH over the southeastern TP by modulating LH.

Previous works have indicated considerable differences between heat sources over the ETP and the WTP, thus it is necessary to investigate their variations separately. In contrast to the widely known crucial role of the CE-TP thermal forcing played in Asian climate, the distinct importance of the western TP (WTP) total heating has been documented (e.g. Wu et al. 2016; Xiao and Duan 2016) but remains poorly understood. Hence, a reliable estimate of the heat sources over the WTP is in urgent need since it's critical for distinguishing the role of the WTP heating in regional to global climate system from that of the CE-TP heating, for evaluating climate models, and further for improving the climate prediction.

This chapter revisits the summer climatology, linear trends, and interannual variations of TH and its three components over the whole TP region. So far, how to quantify the heat sources is still a major topic of the TP meteorology. Reliable estimation of the heat sources over the TP is a basis for representing their characteristics and further understanding their impacts on climate. Some early works applied only one set of reanalysis data, which has great uncertainty in TP diagnostics. For instance, Duan and Wu (2005) pointed out that SH is probably underestimated while precipitation is overestimated in the NCEP/NCAR data. Others utilized biased satellite datasets and oversimplified methods (e.g., Ye and Gao 1979; Yanai et al. 1992; Zhao and Chen 2001), which also induce errors. Most of the recent studies, instead, adopted the more accurate station data (e.g., Duan and Wu 2008; Jiang et al. 2016). Yang et al. (2011; hereafter Yang11) developed a set of new estimations of the TP heat sources based on observational station data, an updated land surface model and selected satellite data. However, surface observation stations on the TP

cannot cover the entire TP region; in particular, stations are scarce in the western part of the TP due to the harsh natural conditions in mountainous areas (Fig. 2.1). In order to investigate the heat sources over the ETP and WTP simultaneously, this chapter synthetically applies the station/gauge-based observations, carefully selected satellite products and multiple bias-corrected reanalysis datasets to estimate the heat sources over the entire TP.

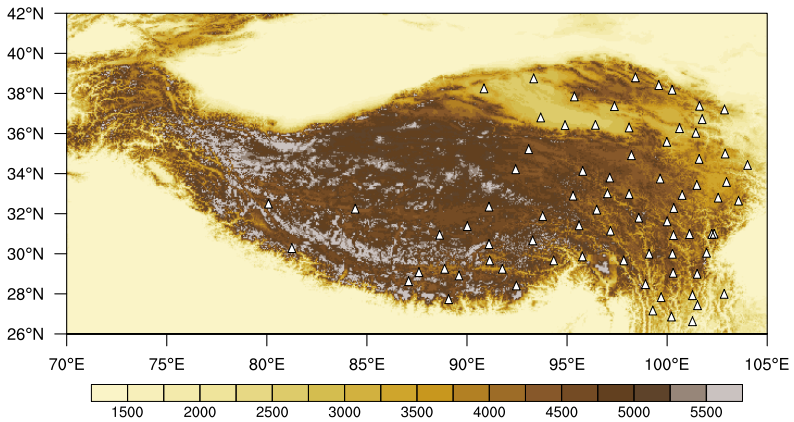

Fig. 2.1. Topography (m) of the Tibetan Plateau and the locations of 77 Chinese Meteorological Administration (CMA) stations on the TP (white triangles).

This chapter is organized as follows. A thorough description of the data and analysis procedures used in this chapter is given in section 2.3. Section 2.4.1 introduces the summer climatology and variance of TH and the contributions from its three components. Section 2.4.2 presents the long-term trends and year-to-year variations of heat sources over different sub-regions of the TP. The discussion and conclusions are presented in section 2.5 and 2.6, respectively.

2.3. Data and Methods

2.3.1. Estimating sensible heat flux

(1) CONVENTIONAL METHOD

Due to the lack of direct observations on surface heat fluxes, SH is conventionally calculated from station data by the following bulk aerodynamic method (e.g., Duan and Wu 2008):

$$SH = C_p \rho_a C_{DH} U_0 (T_s - T_a), \quad (2.1)$$

where ρ_a (kg m^{-3}) is the air density, C_p (=1004 J kg^{-1} K^{-1}) is the specific heat of air at constant pressure, U_0 (m s^{-1}) is the observed near-surface wind speed, T_s (K) is the ground skin temperature, T_a (K) is the surface air temperature, and C_{DH} is the bulk heat transfer coefficient. The wind speed U_0 and the ground-air temperature difference (T_s - T_a) are the two key factors influencing SH. This method is limited by the deficient station data over the WTP, and also obviously depends on the empirical selection of C_{DH}. This coefficient is affected by surface roughness and atmospheric stability, thus varies from location to location and also changes with time (Yang et al. 2011). The chosen values of C_{DH} differ widely among different studies (e.g., Ye and Gao 1979; Li et al. 2000; Duan and Wu 2008). Improper choice of the C_{DH} value may lead to a large bias in the results.

(2) NEW METHOD

In this study, we apply a merged method to carefully selected outputs of surface sensible heat flux (W m^{-2}) in multiple high-quality reanalysis datasets.

i) Data

Since the reanalysis products have assimilated observations for constraining models, it is reasonable to use the reanalysis data as a substitute for the observations in the station-rare region. However, the reanalysis data are commonly known as biased particularly for the highland like the TP. Therefore, verification and bias correction are necessary before selecting the datasets.

SH from eight candidate widely-used reanalysis datasets are first tested, including NCEP-DOE Reanalysis 2 (NCEP-R2, Kanamitsu et al. 2002; T62 Gaussian, 1979-present), NCEP Climate Forecast System Reanalysis (CFSR, Saha et al. 2010; 0.5°×0.5°, 1979-2010), ECMWF Interim Reanalysis (ERA-Interim or ERA-I hereafter, Dee et al. 2011a; 1°×1°, 1979-present), Japanese 25-year Reanalysis (JRA-25, JMA 2008; 1.125°×1.125°, 1983-2008), Japanese 55-year Reanalysis (JRA-55, JMA 2013; 1.125°×1.125°, 1958-2013), Modern-Era Retrospective Analysis

for Research and Application Version 2 (MERRA-2, Gelaro et al. 2017, GMAO 2015; 0.5°×0.625°, 1980-present), Global Land Data Assimilation System Version 2 with Noah Land Surface Model 3.3 (GLDAS-2, Rodell et al. 2004, Beaudoing and Rodell 2015; 1°×1°, 1948-2010), and FLUXNET (Global network of flux tower sites, NASA)-Model Tree Ensemble (FN-MTE, Jung et al. 2011; 0.5°×0.5°, 1982-2009).

ii) Bias correction procedures

Yang11's estimation of SH uses an updated land surface model with the input of high-resolution station data, and it has been evaluated against experimental data. Zhu et al. (2012) verified that Yang11's SH is almost equivalent with their observed result calculated by Chinese Meteorological Administration (CMA) station data using the bulk aerodynamic method. So, we take Yang11 as the observed ground truth, then compare each reanalysis dataset with Yang11's result over the CE-TP, and finally choose the best of them to make a merged SH estimation. Since the criterion data from Yang11 only covered the period of 1984-2006 and the following satellite products also ended in 2007, the time ranges and the grids of all datasets used in this study are uniformed to 1984-2006 and 1°×1°. The boreal summer season [June-August (JJA)] is chosen.

Patterns of JJA climatology of SH in eight reanalysis datasets and Yang11 are shown in Fig. 2.2. The dark dots in Fig. 2.2(i) denote the locations of 77 CMA stations. Over the CE-TP, almost all datasets show that the northwest is higher than the southeast, except the two JMA reanalysis datasets. The magnitudes of SH in some datasets are generally higher than that in Yang11, especially in MERRA-2 and GLDAS-2. Over the western corner of the plateau, the differences among different datasets are significant. Some are very small or even negative, while others are very large. In spite of this, most of the datasets have a minimal value region over there. This feature cannot be speculated by just looking at the spatial pattern of the CE-TP heating, which, again, stresses the significance of finding accurate data over the WTP.

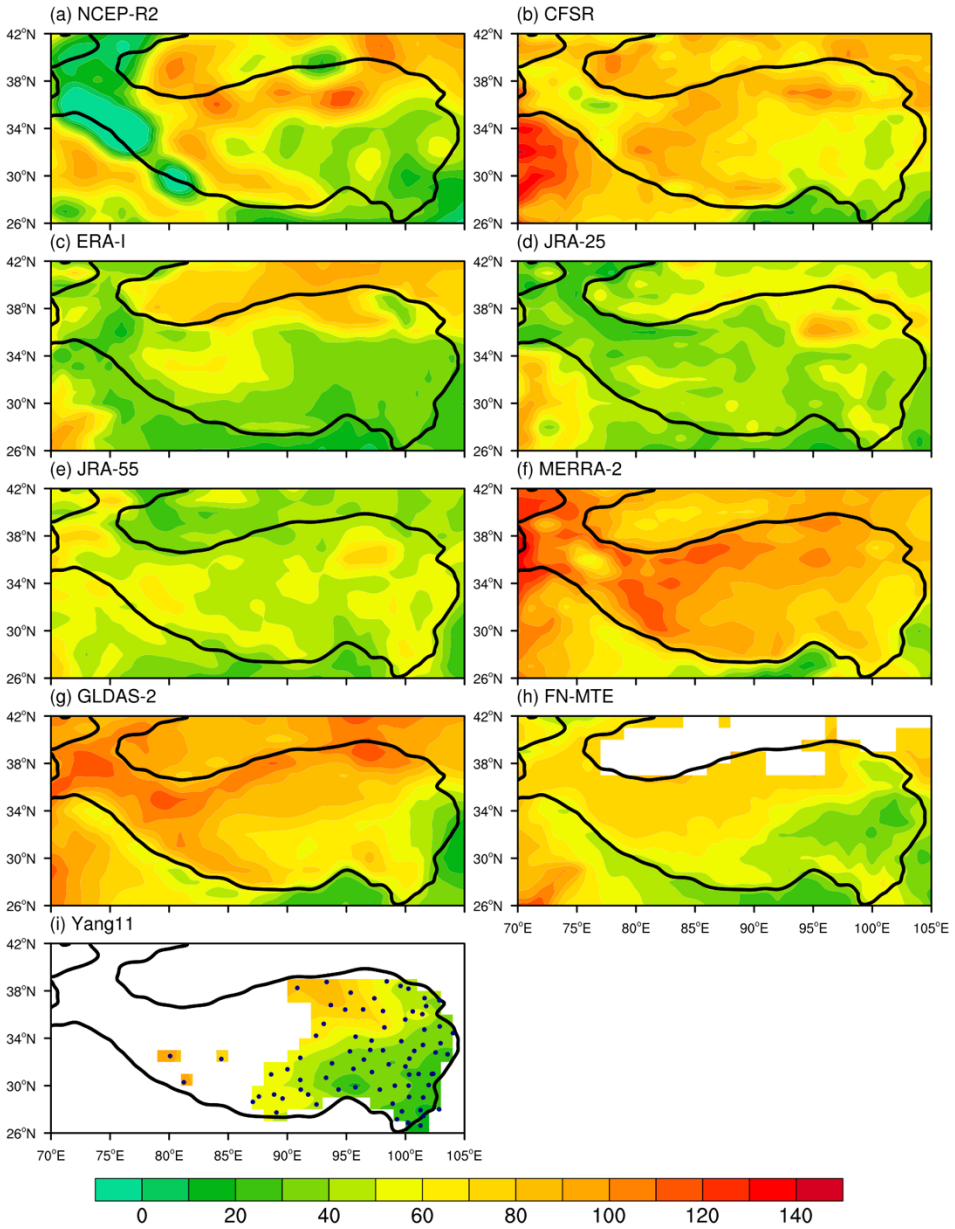

Fig. 2.2. Patterns of JJA mean SH (W m^{-2}) over the TP from nine datasets. The black curve outlines the TP region with height over 2500 m. The dots in (i) denote the CMA stations.

After masking out the areas without stations, we can quantitatively compare the station-covered-area-mean (see "Mean" in Table 2.1), pattern correlation coefficient (PCC) and normalized root mean square error (NRMSE-0) between SH in each reanalysis dataset and in Yang11 (Table 2.1). Apparently, the values of PCC/NRMSE substantially differentiate from each other. Thus, 5 datasets with the highest PCCs are selected first: MERRA-2 (0.82), CFSR (0.77),

GLDAS-2 (0.75), ERA-I (0.7) and FN-MTE (0.7). However, some of their NRMSEs are not small (larger than 1) owing to large area-mean difference (see "Bias" in Table 2.1).

Table 2.1. Comparison between JJA SH in each reanalysis dataset and in Yang11. The units of mean and bias are W m^{-2}.

	Mean	Bias	PCC	NRMSE-0	NRMSE-1	Correlation
Yang11	49.5	-	-	-	-	-
NCEPR-2	51.6	2.1	0.51	1.06	1.05	0.68
CFSR	65.1	15.6	0.77	1.00	0.64	0.79
ERA-I	42.1	-7.4	0.70	0.81	0.72	0.91
JRA-25	48.4	-1.1	0.32	0.98	0.98	0.52
JRA-55	49.7	0.2	0.13	1.03	1.03	0.89
MERRA-2	82.7	33.2	0.82	1.72	0.58	0.86
GLDAS-2	69.2	19.7	0.75	1.19	0.70	0.78
FN-MTE	52.3	2.8	0.70	0.72	0.70	0.73
Merged	49.5	0.0	0.87	-	0.50	0.93

These non-ignorable mean biases are mainly due to the imperfect model representations of the complex TP topography as well as the terrain-dependent physical processes in reanalyses. In order to retain those datasets that have advantages in spatial variations, mean bias correction is performed for each reanalysis dataset, which is to remove the mean difference (bias) from the original SH value (Fig. 2.3 a-h). Consequently, NRMSEs have been reduced significantly (NRMSE-1 in Table 2.1). Then the 5 datasets with the highest PCCs also have the lowest NRMSEs.

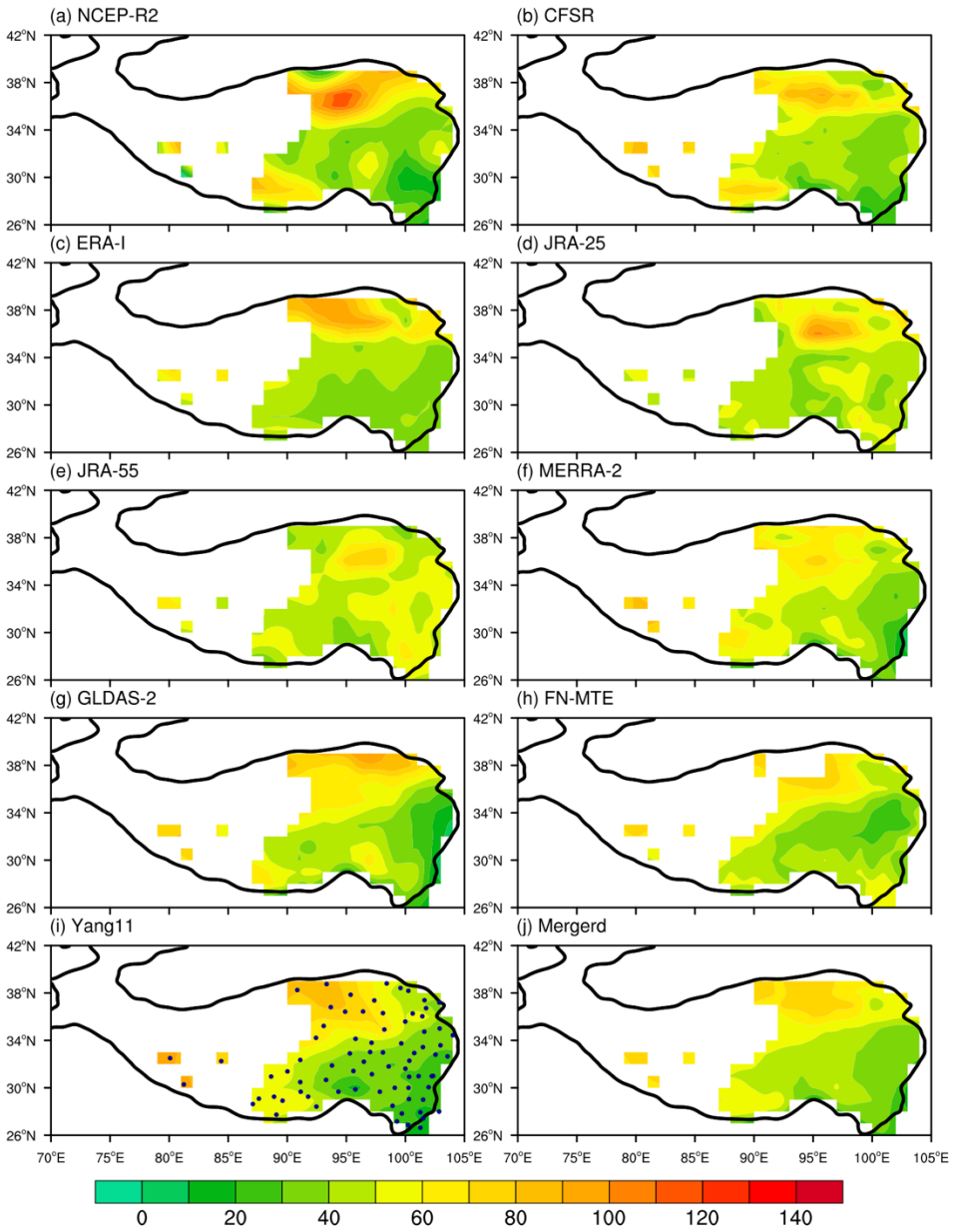

Fig. 2.3. (a-i) Same as Fig. 2.2, except for bias-corrected SH (W m^{-2}). (j) Merged SH by averaging b, c, f, and g.

Apart from climatology, we also care about the long-term trend and year-to-year variation of the heat source. The temporal variations of station-covered-area-average SH in eight reanalysis datasets and Yang11 are presented in Fig. 2.4 (mean biases are not removed in this figure). Consistent with previous studies (e.g., Duan and Wu 2008; Yang et al. 2010; Wang et al. 2012; Zhu et al. 2012), almost in all datasets, including Yang11's, SH shows a clear decreasing trend, except

for JRA-25 and FN-MTE. The correlation coefficients between the time series of each reanalysis dataset and Yang11 are given in Table 2.1 (see Correlation). The five datasets we choose before also have high temporal correlations. JRA-55 has high correlation coefficient as well but its PCC is too low. Another special case is FN-MTE, which has a very small year-to-year variation. Therefore, we eliminate FN-MTE, and merge the rest four best datasets (CFSR, ERA-I, MERRA-2 and GLDAS-2) using arithmetic average (Fig. 2.3 j). The merged SH has the highest PCC, lowest NRMSE and highest correlation coefficient (Table 2.1). For this 4-set ensemble, the signal to noise ratio (SNR), i.e., the standard deviation of the ensemble series divided by the time average of the spread in each year, is 1.51 (Fig. 2.5).

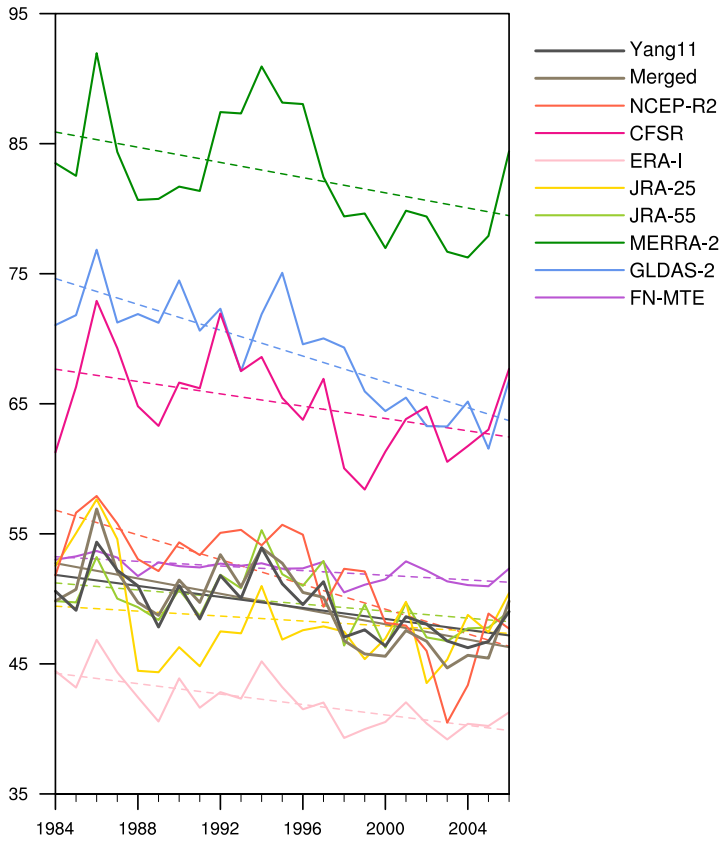

Fig. 2.4. Linear trends and interannual variations of summer SH (W m^{-2}) averaged over the station-covered area on the TP from multiple datasets recorded during 1984-2006.

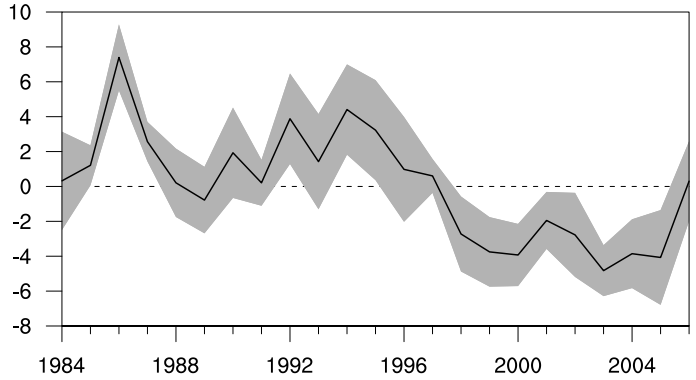

Fig. 2.5. Time evolution of the mean-removed 4-dataset-merged JJA SH (black line; W m^{-2}) over the station-covered TP area plus/minus one ensemble standard deviation (grey shading; W m^{-2}).

The selected four reanalysis datasets have their respective strengths contributing to their better performances in SH over the TP. CFSR is the only reanalysis based on a coupled atmosphere-ocean-land-sea-ice forecast model (Zhang et al. 2013). ERA-I uses an optimal interpolation (OI) scheme to directly analyze observations of 2m-temperature (T) and humidity (q) from surface stations (Dee et al. 2011b), thus its superior near-surface T and q assimilations may favor the better estimation of surface SH. In MERRA-2, the observation-corrected precipitation data is applied directly as part of the forcing for the land surface parameterization (Reichle and Liu 2014). GLDAS-2 utilizes a high-quality vegetation classification map considering the fluxes of energy and water at the land surface is strongly tied to the properties of the vegetation (Rodell et al. 2004).

We further assume that the bias is systematic: in one dataset, no matter whether over the western or eastern TP, a uniform bias value is removed for all grid points over the whole TP. Therefore, the merged SH is obtained by averaging the four bias-corrected datasets.

2.3.2. Estimating latent heat release by precipitation

LH is calculated by total precipitation via the following formula:

$$\mathrm{LH} = \mathrm{Pr} \times L_w \times \rho, \tag{2.2}$$

where Pr includes convective and large-scale precipitation, $L_w = 2.5\times10^{-6}$ J kg^{-1} is the condensation heat coefficient, and $\rho = 10^3$ kg m^{-3} is the density of liquid water.

For Pr, we take an average of the following four gauged-based/merged precipitation datasets:

(1) NOAA's Precipitation Reconstruction over Land (PREC/L, Chen et al. 2002): Interpolation of gauge observations over land (1°×1°, 1948-present);

(2) APHRODITE's (Asian Precipitation – Highly-Resolved Observational Data Integration Towards Evaluation) continental-scale product (Yatagai et al. 2012): Apply a dense network of rain-gauge data for Asia including the Himalayas (0.5°×0.5°, 1951-2007);

(3) GPCP Version 2.2 Combined Precipitation Data Set (Adler et al. 2003): Data from rain gauge stations, satellites, and sounding observations have been merged to estimate monthly rainfall (2.5°× 2.5°, 1979-2015);

(4) CPC Merged Analysis of Precipitation (CMAP, Xie and Arkin 1997): Multiple satellite estimates and gauge data are merged (2.5°× 2.5°, 1979-present).

For the precipitation, the better representation by gauge-based and merged datasets than reanalysis over the TP has been confirmed by many previous studies (Tong et al. 2014; You et al. 2015; Song et al. 2016). Thus, we also utilized the above four such better datasets for merging precipitation, i.e. for estimating LH over the TP. The climatological patterns and temporal evolutions of LH from the four gauged-based datasets and the 4-merged data are shown in Figs. 2.6 and 2.7. The JJA-mean LH in each dataset is highly correlated with each other (high PCC). There is an increasing trend in the total-TP averaged LH (Fig. 2.7). In addition, the SNR of the four gauge-sets ensemble is 1.54 (Fig. 2.8), indicating the high quality of the G-merged LH estimation.

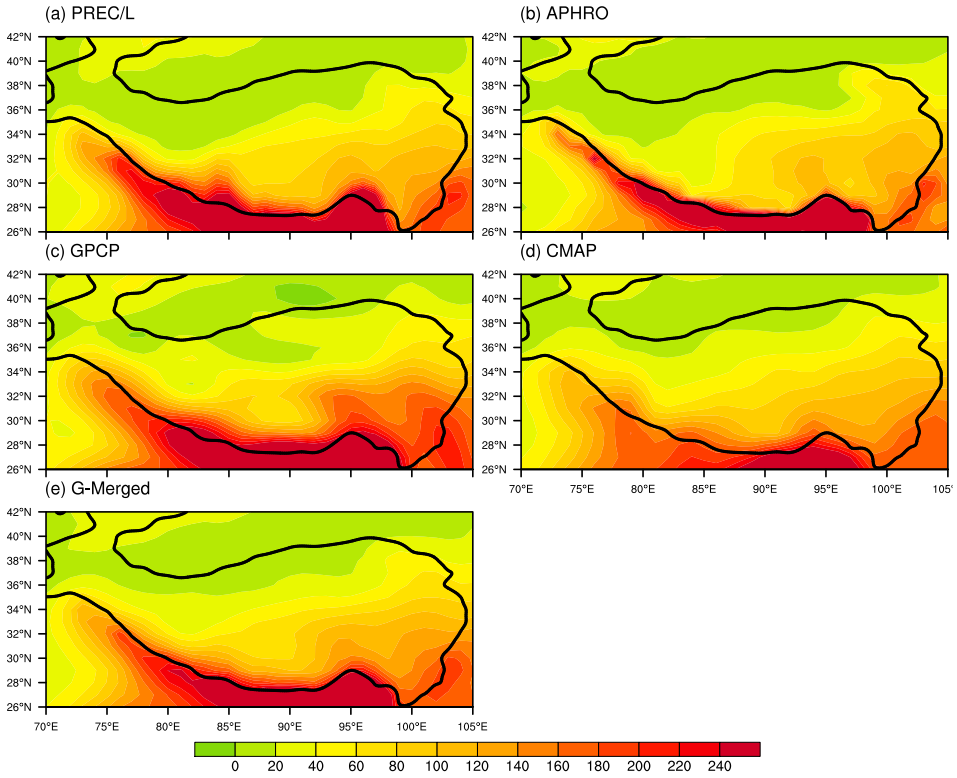

Fig. 2.6. Patterns of the summer climatology of LH (W m^{-2}) over the TP obtained from the four gauge-based datasets (a–d) and the gauge-merged data (e; G-merged) that is the ensemble mean of (a) to (d).

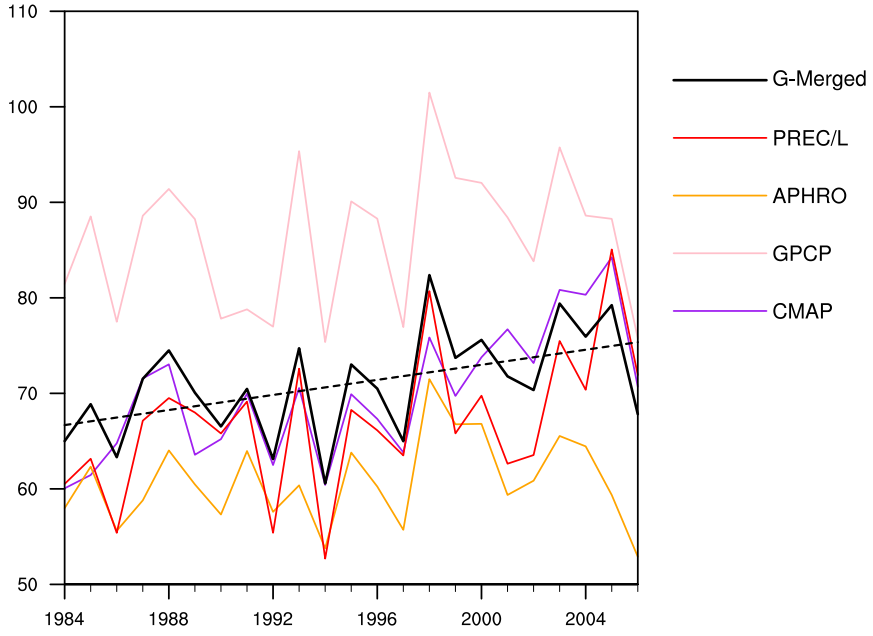

Fig. 2.7. Temporal evolutions of summer LH (W m^{-2}) averaged over the whole TP region (altitude > 2500 m) in multiple datasets.

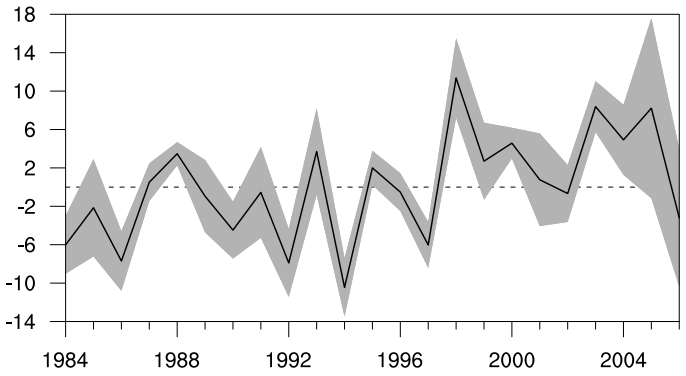

Fig. 2.8. Time series of the mean-removed G-merged JJA LH (black line; W m^{-2}) over the total TP area plus/minus one ensemble standard deviation (grey shading; W m^{-2}).

2.3.3. Estimating net radiation flux

RD is defined by the expression:

$$\begin{aligned} \mathrm{RD} &= \mathrm{RD}^{\downarrow}_{\mathrm{toa}} - \mathrm{RD}^{\downarrow}_{\mathrm{sfc}} \\ &= \left(\mathrm{SW}^{\downarrow}_{\mathrm{toa}} - \mathrm{SW}^{\uparrow}_{\mathrm{toa}} - \mathrm{LW}^{\uparrow}_{\mathrm{toa}}\right) - \left(\mathrm{SW}^{\downarrow}_{\mathrm{sfc}} - \mathrm{SW}^{\uparrow}_{\mathrm{sfc}} + \mathrm{LW}^{\downarrow}_{\mathrm{sfc}} - \mathrm{LW}^{\uparrow}_{\mathrm{sfc}}\right), \end{aligned} \tag{2.3}$$

where $\mathrm{RD}^{\downarrow}_{\mathrm{toa}}$ and $\mathrm{RD}^{\downarrow}_{\mathrm{sfc}}$ are net downward radiative fluxes at the top of the atmosphere (toa) and at the ground surface (sfc), respectively. The superscript ↓ (↑) represents downward (upward) transport, and the variable SW (LW) denotes shortwave (longwave) radiative flux.

We calculate RD using radiative fluxes from the following two satellite products that are the major global data sets for the radiation budget:

1) NASA/GEWEX Surface Radiation Budget Release-3.0/3.1 (SRB, SRB Science Team 2010 and 2012; 1° × 1°, 1983-2007);

2) International Satellite Cloud Climatology Project Flux Data (ISCCP–FD, Y.-C. Zhang et al. 2004; 2.5°×2.5°, 1983-2007).

From earlier studies, we know that there are some discrepancies between these two satellite datasets (Yang et al. 2011; Wang et al. 2012), so we look into each term of RD to see where the differences are. It can be found that the difference is much larger at the surface (SFC) than at the

top of the atmosphere (TOA) (Fig. 2.9). The PCC between SRB and ISCCP net radiation at TOA is 0.74 while that at SFC is only 0.40, and the correlation coefficient of the time-series is 0.73 at TOA but near zero at SFC. Thus, we take the ensemble mean of SRB and ISCCP net radiation at TOA, and at the surface, we need to further investigate which term leads to the difference.

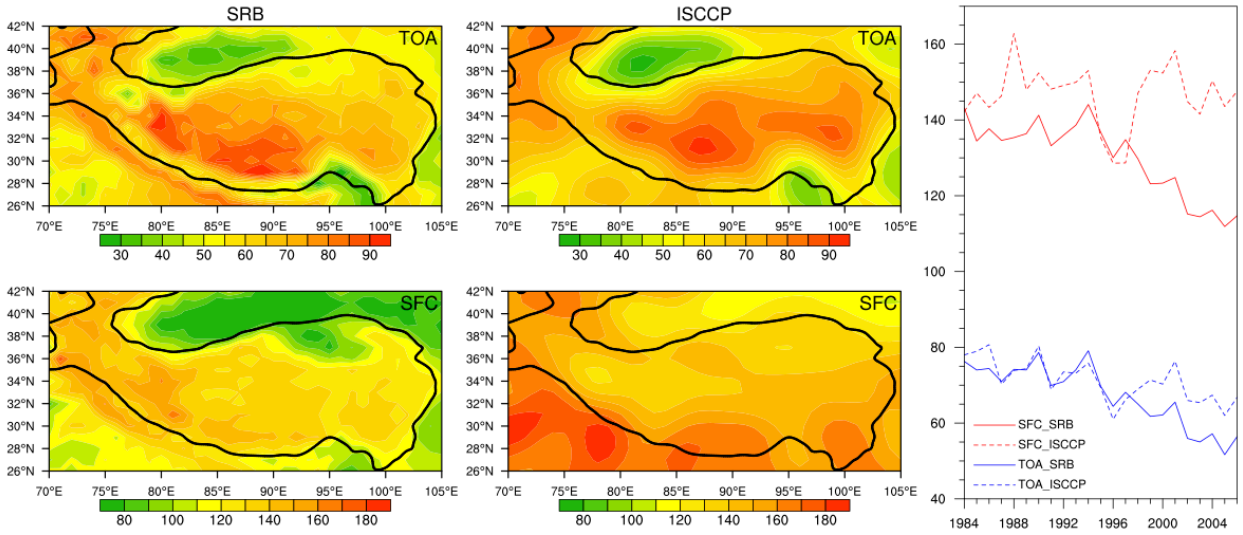

Fig. 2.9. Patterns of the summer climatology (left) and temporal evolutions (right) of net radiation (W m^{-2}) at the top of the atmosphere (TOA) and at the surface (SFC) over the TP obtained from SRB and ISCCP respectively.

Fig. 2.10 shows the climatology of the 4 components (downward SW, LW and upward SW, LW) of the surface net radiation over the TP from SRB and ISCCP respectively. The PCCs of downward SW, LW and upward LW between the two datasets are higher than 0.8, and the PCC of upward SW is 0.6. It can be found that there are large biases between the temporal evolutions of the LW radiation, and the correlation between the SRB and ISCCP upward SW is very low (Fig. 2.11). The SRB downward SW and that of ISCCP are highly correlated with each other.

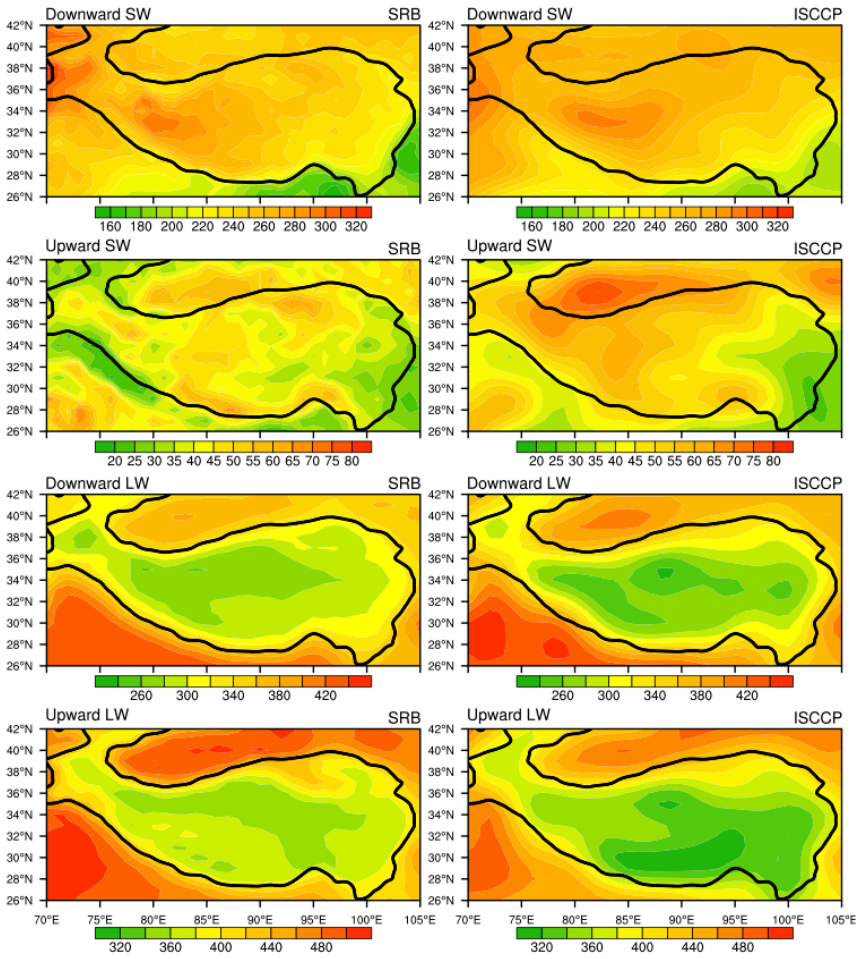

Fig. 2.10. Summer climatology of the four radiative components (downward SW, LW and upward SW, LW; W m^{-2}) of the surface net radiation over the TP from SRB and ISCCP respectively.

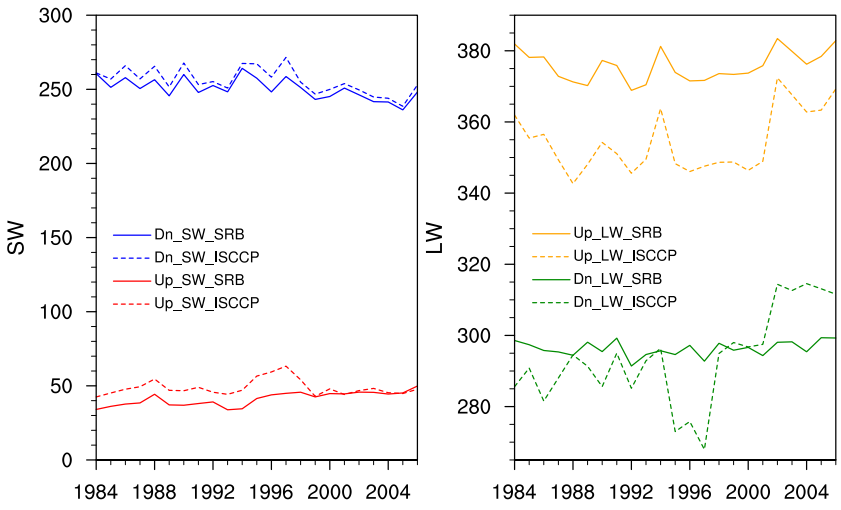

Fig. 2.11. Temporal evolutions of the radiation components (W m^{-2}) averaged over the whole TP.

Zhang et al. (2006) summarized that two sets of the input data from Earth observations used for radiative transfer models largely limit the accuracy of surface radiative flux estimates in satellite products: the near-surface atmospheric radiative properties (temperature and humidity) and the surface radiative properties (e.g. surface skin temperature, solar albedo and infrared emissivity). The leading factor that causes problems with the surface downward (upward) LW is the surface air (skin) temperature (Zhang et al. 2006). A disagreement of 2-4 K in temperature can easily cause 10-15 W m^{-2} uncertainties in the calculated surface LW. Yang et al. (2006) showed the lower-than-observed surface air and skin temperature over the TP in ISCCP data that led to considerably underestimates of the surface downward and upward LW, respectively. Another factor that affects LW is the surface elevation. The altitudes in SRB and ISCCP grids are generally higher than the corresponding observational sites over the TP (Yang et al. 2006). However, the SRB used herein is an updated version (release 3.0) in which the LW estimates are adjusted for the elevation difference between the 1°x1° grid box mean elevation and the site elevation (Stackhouse et al. 2011). Yang et al. (2006) confirmed that the height correction could largely reduce the errors in SRB LW but not work for ISCCP LW. The land surface albedo, an important input quantity in a radiative transfer model for SW calculation, is also one of the major sources of uncertainties for these radiative products (Zhang et al. 2007). The albedo of complex land surface like the Tibetan Plateau is more difficult to determine since it's variant and affected by the precise mixture of soil/rock, vegetation and snow and the temporal variations of vegetation activity and snow. The uncertainty in surface albedo could result in the large difference in the upward SW between the two datasets. After evaluating the TP surface radiation, Yang et al. (2006) suggested that SRB is better than ISCCP for LW while ISCCP is more reasonable for SW.

The selection of which product for which radiative term is based on the conclusions from previous works and also a comparison with a latest satellite dataset CERES (Kato et al. 2018; Loeb

et al. 2018). We compared each surface radiative term in the SRB and ISCCP data with that in CERES (figure not shown), only using the data after 2000, and similar conclusion with Yang's (2006) can be obtained. Thus, for the final RD estimates, we take the average of SRB and ISCCP for the net radiation at TOA and for the surface downward shortwave radiation; for other components at surface, we apply the SRB-only longwave radiation and the ISCCP-only upward shortwave radiation.

Therefore, the expression of the total heat (TH) source is the sum of the abovementioned three components:

$$\mathrm{TH} = \mathrm{SH} + \mathrm{LH} + \mathrm{RD}. \tag{2.4}$$

2.4. Characteristics of the Tibetan Plateau Heat Sources

2.4.1. JJA climatology and variance

Before discussing the temporal variations in the heat sources over the TP, it is necessary to first examine the summer climatology in terms of the spatial distribution of JJA mean heat sources. To reveal the different contributions of individual components to the year-to-year variation of TH, we also analyze the variances (i.e., standard deviations) of TH and its three components.

Figure 2.12 shows the climatological means of JJA TH, SH, LH, and RD, and their variances over the TP. Generally, the climatology has a southeast-to-northwest oriented distribution, except RD. In opposite to the distribution of SH, which is higher over the northwest (> 50 W m^{-2}), TH and LH are higher over the southeastern TP (>70 W m^{-2}) than over the northwestern TP (< 40 W m^{-2}). The pattern of RD is more homogeneous with a negative value (~ -50 W m^{-2}), exhibiting the net radiative cooling effect. The TH pattern almost resembles that of LH but with smaller magnitude. A minimum value appears in an area on the northwestern TP (around 76°E, 36°N),

where TH even becomes negative. Over there, SH also presents a minimum value, and LH is relatively small, whereas the radiative cooling is strong. In that particularly high-altitude region, where the Karakoram Mountain Range is located, many glaciers are cover by a layer of debris (Veettil 2012), which insulates the ice surface from the warmth of insolation.

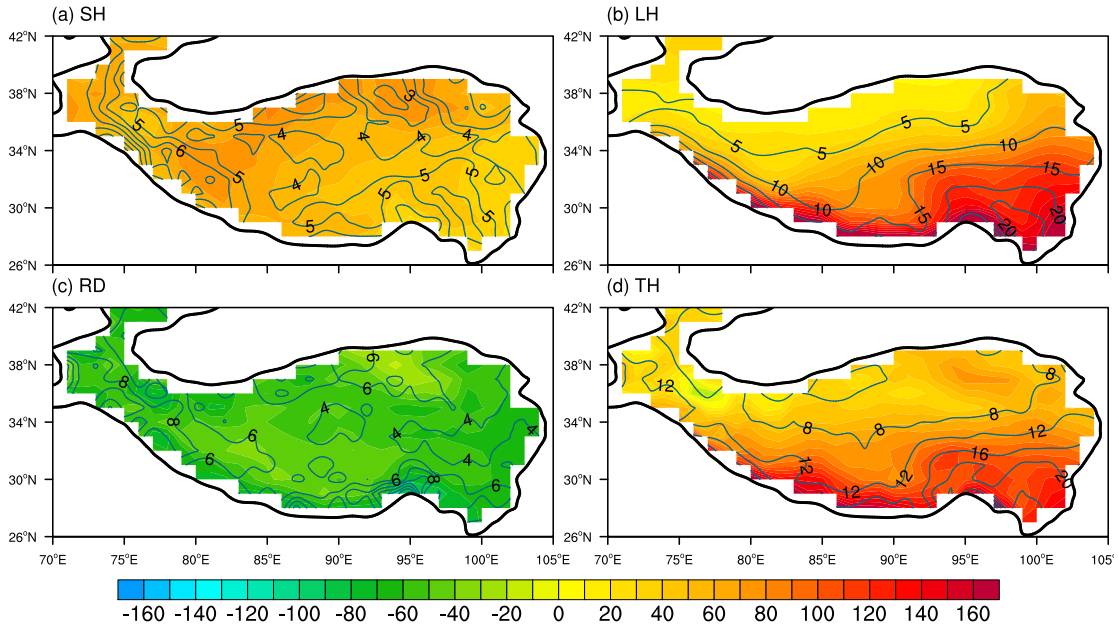

Fig. 2.12. JJA mean (shading; W m^{-2}) and variance (contours; W m^{-2}) of (a) SH, (b) LH, (c) RD, and (d) TH over the TP from 1984 to 2006. The black curve outlines the TP region with height over 2500 m.

The reason for forming the JJA climatology pattern of LH (decrease from southeast to northwest) is mainly because the moisture sources for the TP regions in summer come from the south (Indian summer monsoon) and the east (East Asian summer monsoon) through the strong summer monsoon. The high mountains in the southern flank of the TP prevent the moisture from transporting further northward. The northwestern TP is far inland, so that the moisture could hardly reach to that region. Similar changes are also reflected in vegetation, which varies from forest to grassland and then desert (Liu and Yin 2001). The spatial distribution of JJA SH (increase from southeast to northwest) is generally opposite to the distribution of LH. The northwest inland areas have less precipitation, so the surface can receive more solar radiation on sunny days. The less-

vegetation-covered WTP has stronger surface wind speed and surface warming (directly receiving more incoming solar radiation) that induces higher surface ground-air temperature difference and thus stronger SH. RD shows an overall cooling effect, since the direct heating of the atmosphere by solar radiation is much smaller than the energy loss caused by the outgoing long-wave radiation.

The standard deviation (variance) is calculated after removing the linear trend in order to represent the magnitude of interannual variation. The spatial distributions of variance basically resemble the patterns of mean for both LH and TH, which have higher values over the southeastern TP (>10 W m^{-2}). The variance of SH in the western and southern side (> 6 W m^{-2}) is larger than that in the northeast. RD has relatively homogeneous variance (~ 6 W m^{-2}). The relative standard deviation (RSD), i.e., the proportion of the standard deviation to the mean, can better express the relative importance of the interannual variability. For SH and RD, the RSD is about 10%, whereas it's around 15% for LH. The RSD is generally larger than 15% for TH. In particular, the RSD over the western and northern parts, exceeding 40%, is extremely large due to the small value of the mean TH, thus indicating a prominent year-to-year variation there.

For both the mean and variance, LH has the largest magnitude over most of the TP, particularly over the southern and eastern regions. Over the WTP, the mean SH exceeds mean LH, and the magnitude of mean RD is comparable with that of mean SH. Comparing the pattern of TH with that of SH, LH, and RD, it can be seen that the spatial variation of summer TH is overall dominated by LH. During the rainy season, the latent heat released from monsoon rainfall is the dominant heat source over the TP.

To quantitatively compare the heat sources over different parts of the TP, the entire TP region has been divided into 3 sub-regions: the western TP (WTP, 70°E-82°E), central TP (CTP, 82°E-92°E) and eastern TP (ETP, 92°E-105°E). Actually, there is no natural boundary partitioning the TP. Hu et al. (2021) showed that the first two EOF leading modes of the TP precipitation (i.e.,

latent heat) present an east-west distribution pattern. The most significant anomalous center of the first (second) EOF mode is located in the south-central (southeastern) TP. Therefore, it is reasonable to divide the plateau into east and west parts. In order to highlight the most western part, we move the western-central boundary westward from conventionally used 85°E to 82°E. The area-mean values of TH and its three components in every summer month are given in Table 2.2. LH plays the most important role in TH over the CE-TP and in July-August, while SH is lager in June and over the CW-TP. Radiative cooling is strongest in August.

Table 2.2. The areal mean of monthly climatology of summer atmospheric heat sources (W m^{-2}) over various sub-regions of the TP, and the ratio of JJA mean of each heat component to TH.

		June	July	August	JJA mean	JJA component to TH ratio
ETP	SH	45.5	39.0	34.4	39.6	0.57
	LH	75.2	83.6	72.5	77.1	1.11
	RD	-44.7	-45.1	-52.5	-47.4	-0.68
	TH	76.0	77.5	54.4	69.3	-
CTP	SH	60.5	51.2	42.8	51.5	0.82
	LH	40.8	62.8	59.4	54.3	0.86
	RD	-41.1	-40.4	-47.3	-42.9	-0.68
	TH	60.1	73.7	54.9	62.9	-
WTP	SH	51.8	52.6	47.1	50.5	1.37
	LH	24.2	41.1	37.3	34.2	0.93
	RD	-40.9	-46.2	-56.4	-47.8	-1.30
	TH	35.1	47.5	28.1	36.9	-

2.4.2. Temporal variations: long-term trends and interannual variations

Next, we analyze the long-term trend and year-to-year variations of JJA TH and its three components in the three parts of the TP respectively since they show large spatial inhomogeneity (Fig. 2.12). The method of area-average is utilized to get the time series over each sub-region (Fig.

2.13), and the area-mean value has been removed.

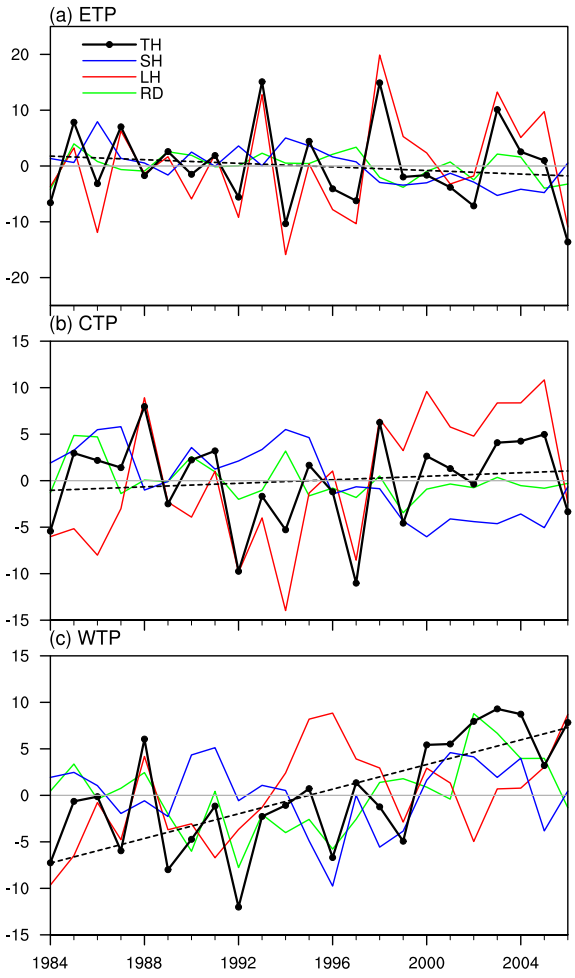

Fig. 2.13. Temporal variations of summer anomalies for TH, SH, LH, and RD (W m^{-2}) in JJA over the (a) ETP, (b) CTP, and (c) WTP. The black dashed line denotes the linear trend of TH over each sub-region.

A slight decreasing trend appears in TH over the ETP (Fig. 2.13a) due to the downtrend of RD an SH that is partly offset by the uptrend of LH. The increasing trend in TH over the CTP is relatively weak (Fig. 2.13b). Oppositely, TH over the WTP shows a considerable ascending trend, about 6.6 W m^{-2} per decade that exceeds the significance level of 99%, following the strong rising in precipitation before 1996 and the weakening of radiative cooling after 1996 (Fig. 2.13c).

The downward trend of the radiative forcing is likely caused by multiple sources. The strengthening of radiative cooling (decrease of negative RD value) is closely associated with the

persistent decline of daytime total cloud amount since mid-1970s (Duan and Wu 2006). Wu et al. (2015) concluded that the intensification of radiative cooling since 1980s is due to the enhanced outgoing radiation at TOA, as a combined effect by global warming and change in cloud height. More low-level cloud cover with strong reflection to SW intensified the outgoing SW. The higher surface emissivity under planetary warming and the decrease in total cloud cover (reducing LW absorption and counter radiation) enhanced the outgoing LW. Again, RD over the WTP in our study presents a different warming trend since early 1990s, which is possibly affected by different change of the local clouds. The processes causing the change of cloud amount are complicated and beyond the scope of this study. In addition, a recent study (Xu et al. 2017) showed the significant decreasing trend of summer snow cover since 1980s from station observations. All the three stations to the west of 85°E showed the negative trends, indicating the high possibility of the decreasing trend of snow cover over the WTP. Reduced snow cover would lower the surface albedo, thus weaken the radiative cooling over the WTP.

Precipitation in the TP has increased in most regions over the past several decades, especially in the CE-TP. An earlier study showed the increasing trend in LH is consistent with that snow depth over the TP increases persistently during mid-1970s to 1990s (Y.-S. Zhang et al. 2004). A clear jump to stronger precipitation over the CE-TP can be found in the late 1990s, which could be linked to the intensification of Indian summer monsoon with the interdecadal strengthening of high-level (850-600 hPa) Somali Jet (Kang et al. 2010; Xiao et al. 2015). However, for the WTP in our study, LH decreased since 1996 (red line in Fig. 2.13c), showing a totally different interdecadal change. This confirms the different impacts of climate change on different TP sub-regions. Maybe on the interdecadal timescale, there's an east-west dipole pattern in LH (precipitation), in which the WTP LH exhibits opposite phase change to the ETP LH. This conjecture needs to be verified using longer data in future work.

The downward trend in SH over the CE-TP has been consistently found by lots of previous works. Since that region is station-covered, all of their calculation of SH is based on the CMA station data. Although the distribution and altitudes of the CMA stations could induce uncertainties in estimating the heat sources, the negative trends have been detected in SH at all of the current stations regardless of their altitudes (Duan et al. 2014). Thus, this decreasing trend should be credible in spite that its magnitude is uncertain. Yang et al. (2011) suggested that this weakening trend was overestimated in previous studies. The decline of SH is closely connected with the persistent decrease of the surface wind speed (U_0) over the CE-TP since 1970s (Duan et al. 2008). In addition, the surface air temperature (T_a) shows a rapidly upward trend, while the increase of ground surface temperature (T_s) is slower, leading to a decrease in (T_s - T_a), thus the decline of SH. Yang et al. (2014) suggested that the decline of the surface wind speed is transferred from the upper-air into the boundary layer. Observed evidence indicates that the wind speed change over China (the Plateau included) is due to the latitudinal gradient of surface warming over Central and East Asia (Lin et al. 2013). This warming gradient altered the upper-level pressure gradient force, then the upper-level wind adapted to it through geostrophic adjustment, and eventually the surface wind speed is changed by downward momentum transport (Yang et al. 2014). A recovery in SH after early 2000 is found over the CE-TP and it has been documented in a recent study (Zhu et al. 2017) as a phenomenon associated with the recent global warming hiatus (1998-2012). During the hiatus, the previous declining in surface wind speeds has been generally recovered. Besides, the increase of the total cloud amount at night enhances the atmospheric downward LW radiation, inducing the nocturnal surface warming, thereby leading to the rise of (T_s - T_a). Both the changes in wind speed and in ground-surface temperature difference cause the recovery of SH during the global warming hiatus.

The time evolutions of U_0 and (T_s - T_a) in the selected reanalysis datasets (just average of the four sets, no bias correction) are shown in the Fig. 2.14. The decrease and recovery of the surface wind speed over the CE-TP can be detected by reanalysis. We found in the reanalysis data, the decline trend of (T_s - T_a) is more significant than that of U_0 over the CE-TP. This is different from the results of previous observational studies, indicating the uncertainties in reanalysis data. Whereas over the WTP, (T_s - T_a) has a slight increasing trend, contrasting to the descending trend of U_0. The increase of (T_s - T_a) is probably owing to the increase of T_s because of the reduction of snow cover. Possibly the overall effects by both U_0 and (T_s - T_a) lead to the insignificant trend in SH over the WTP.

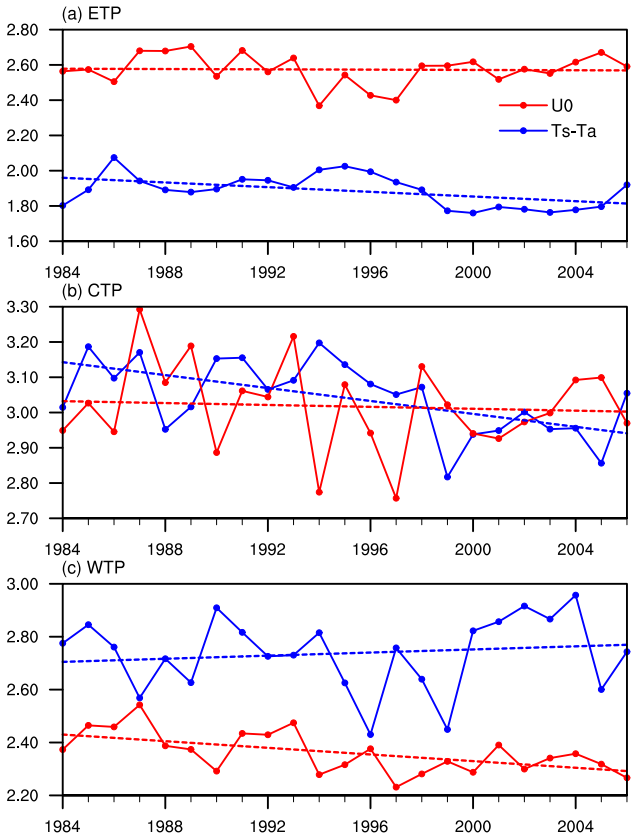

Fig. 2.14. The time evolutions of surface wind speed (U_0; m s^{-1}) and ground-air temperature difference (T_s - T_a; K) in the merged reanalysis dataset over the ETP (a), CTP (b), and WTP (c), respectively.

In order to obtain the interannual variations, linear trends have then been removed, and the following discussions are based on detrended time series. TH is highly correlated with LH over the ETP ($r = 0.92$, $p < 0.01$) and CTP ($r = 0.80$, $p < 0.01$), which demonstrates that the variation of LH dominates that of TH in the central-eastern TP. Meanwhile, for the WTP, the correlation between TH and LH is negligible ($r = 0.08$). The WTP TH is significantly correlated with RD ($r = 0.62$, $p < 0.01$) and SH ($r = 0.53$, $p < 0.01$). Comparing the JJA TH among the three sub-regions (Table 2.3), we can find that the WTP TH is uncorrelated with the ETP TH. The different interannual variations of TH over the WTP and over the ETP indicate their potential separate climate impacts.

Table 2.3. Correlation coefficients (r) among the ETP, CTP, and WTP for detrended TH in each month and JJA mean. The italic, bold, and red bold values denote they exceed the confidence level of 90% ($p < 0.10$), 95% ($p < 0.05$), and 99% ($p < 0.01$), respectively.

	June	July	August	July-August	JJA
(ETP, CTP)	0.21	**0.45**	**0.76**	**0.64**	**0.53**
(CTP, WTP)	0.30	**0.48**	0.21	*0.38*	**0.55**
(WTP, ETP)	-0.06	-0.17	-0.22	-0.08	0.05

Because LH released by precipitation may have large differences before and after summer monsoon onset and TH is dominant by LH, TH may be quite different for each month. Thus, we analyze the temporal evolutions of SH, LH, RD, and TH in each month separately. As shown in Fig. 2.15, the series in each month are considerably different. Specifically, there are decadal variations of TH over the CTP and WTP in July, while more interannual variations of TH appear in June and August. The variance of the TH time series becomes larger from June to August. The WTP and ETP TH also show distinct variations. From the mid- to late 1980s, TH in June is quite strong over the WTP, whereas over the ETP, it is abnormally weak. Similar contrast also occurs in

August during mid 1990s. Besides, the interannual variability of LH is generally larger than that of SH and RD.

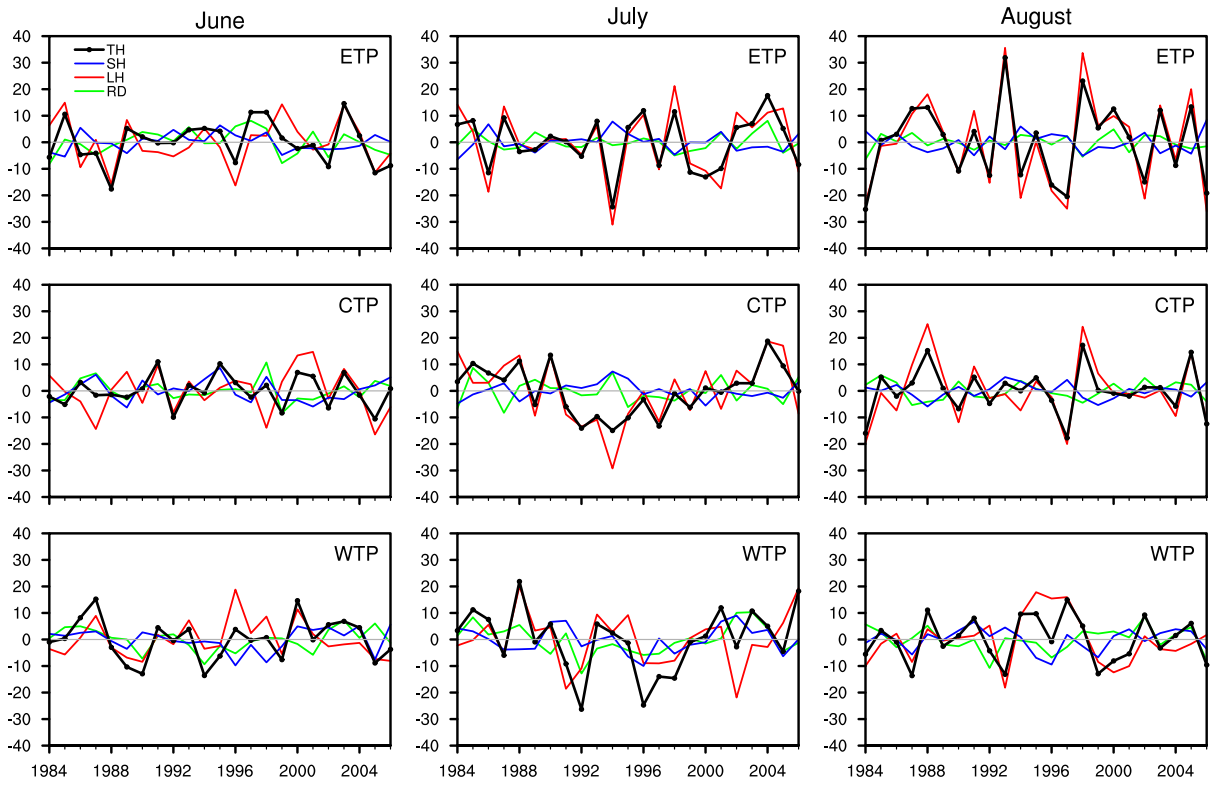

Fig. 2.15. Evolutions of detrended anomalous TH, SH, LH, and RD (W m^{-2}) over the ETP, CTP, and WTP in each summer month.

We further examine the temporal correlation coefficients of TH among the ETP, CTP and WTP in each month (Table 2.3) and the coefficients among June, July and August over each sub-region (Table 2.4). As shown in Table 2.3, TH over the WTP and ETP are overall not linearly correlated, while TH over the ETP and CTP are highly correlated in July-August, i.e., in the heavy rainfall months. The correlation between TH over the CTP and WTP is also significant in July. Table 2.4 shows the month-to-month correlation among the TH time series. None of the correlation coefficient values exceeds the confidence level of significance, indicating large subseasonal variation of TH, which supports the result shown in Fig.16.

Table 2.4. Correlation coefficients among June, July, and August for detrended TH over different sub-regions of the TP.

TH	ETP	CTP	WTP
(June, July)	0.07	-0.11	-0.10
(July, August)	0.17	0.17	-0.12
(June, August)	0.15	0.02	-0.31

2.5. Discussion

Considering the possible interdecadal variability in the heat sources, we have attempted to extend our new dataset to 2016. However, due to the early termination of certain selected datasets, we could only lengthen with those products that are available in a longer term and still have reasonably good quality. From the extended data, it is shown that the trends in 1984-2006 are likely to be a deceasing or increasing phase of interdecadal variations (Fig. 2.16). For SH, the temporal variations of the station-covered CE-TP area averages of the JJA SH in each selected dataset are shown in the Fig. 2.16(a). Only two (ERA-I and MERRA-2) of the four selected reanalysis datasets cover the whole period of 1984-2016. CFSR only provides reanalysis data until 2010, and its values are particularly abnormal since 2007. GLDAS-2.0 dataset is also ended in 2010, while its recent counterpart, GLDAS-2.1 (Beaudoing and Rodell 2016), starting from 2000 is provided until present. But these two versions have apparent difference. Therefore, we only merged the bias-corrected ERA-I and MERRA-2 for the extended period of 2007-2016, as depicted by the red dashed line in Fig. 2.16(a). The 2-sets merged data is comparable with the 4-sets merged one in the period of 1984-2006, showing high correlation with Yang11 (figure not shown). For the extended period, SH in MERRE-2 continuously declined after a short recovery of 2004-2006 and recovered again since 2011, the ERA-I slightly recovered. The different temporal changes between MERRA-2 and ERA-I result in the insignificant decreasing tendency of the merged one. The lack

of validation in this stage increases the uncertainties in the prolonged merged dataset.

A similar figure but for the total TP area averages of LH are shown in Fig. 2.16(b). Except that APHRODITE data ended in 2007, the other three still exhibit good agreement after 2006. The red solid line in Fig. 2.16(b) denotes the 3-sets (except APHRO) merged LH. Despite a small mean difference, the 3-sets G-merged dataset is significantly correlated with the 4-sets merged one. The dashed black line is added by subtracting the mean difference between the two G-merged datasets in 1984-2006 from the red line. We can see that the previous increasing trend has been shifted to a slight decreasing tendency since 2008. The total-TP area averages of RD are presented in Fig. 2.16(c). It is found that the CERES is highly different from the SRB-ISCCP merged one during the overlapping years of 2000-2006. Comparisons of each surface radiative term in SRB and ISCCP with that in CERES suggest that one might apply the closer-to-CERES SRB-only LW and ISCCP-only upward SW to the merging, but the discrepancies between them still cannot be ignored (especially in upward SW). Nevertheless, if we subtract the mean difference between the merged RD and CERES in 2000-2006, we can extend the merged RD by using CERES up to 2016. But the reliability of extending RD by adding CERES remains uncertain and further validation is needed. By the time updated satellite and observation data become available, we will make our effort to apply our selection and verification method to those updated data and expect to get a more reliable lengthened dataset.

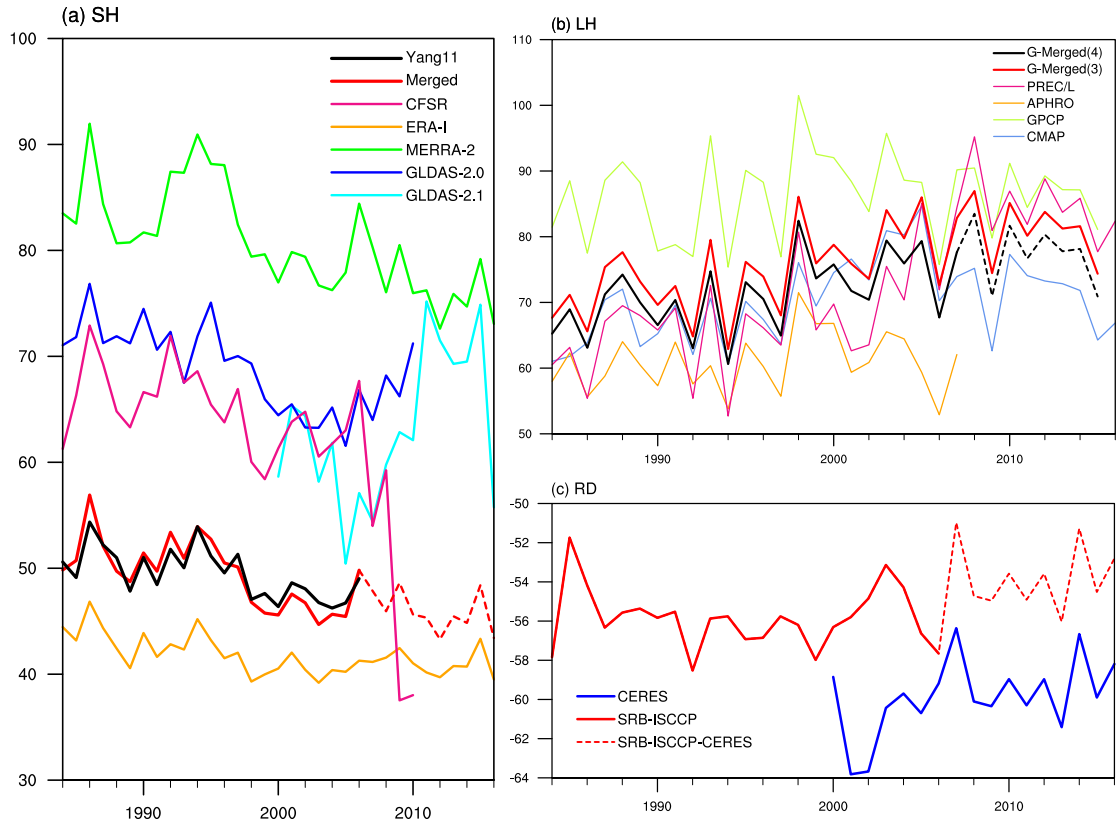

Fig. 2.16. Temporal variations of summer (a) station-covered-area averaged SH and total-TP averaged (b) LH and (c) RD (W m^{-2}) from multiple datasets in the period of 1984-2016.

There are still some uncertainties in our merged estimation since the merging method is not perfect. The mean bias in a reanalysis dataset is assumed to be same for all the sub-regions. After checking the mean bias of the ETP and CTP separately, we found that the values of bias are indeed not the same. However, the bias of the CTP is smaller than that of the ETP in most selected reanalysis datasets (CFSR, MERRA-2, GLDAS-2), while larger in the others (ERA-I and other not-selected datasets). It seems that the bias is not increasing from the east to the west when compared to the station-observation. For further verification, we also set each of the eight reanalysis datasets as the "criterion" and compared it with the remaining seven datasets. Results showed that the biases between most datasets are indeed larger in the western TP than in the eastern TP, except the bias between MERRA-2 and GLDAS-2 as well as the bias between CFSR and

FLUXNET-MTE. The biases for these two pairs of datasets are even smaller in the WTP since their corresponding spatial patterns are quite similar across the whole TP (Fig. 2.2-f, g and b, h). The east-west difference of the bias for each pair of reanalysis datasets is very inconsistent. Therefore, we cannot conclude how much the bias in the WTP is greater than the ETP.

Arguably, removing a uniform mean bias at this stage is a better way for bias correction since it can retain the spatial and temporal variations in the original data to the largest extent. The lack of in situ data for verification over the WTP and the uncertainties in the observational criterion itself call for more in situ observations and more meteorological station establishment over the TP. In spite of this, we still believe that those selected datasets with better performance over the CE-TP could better capture the main characteristics of the spatiotemporal variations of SH over the WTP as well.

In addition, there is a possible meridional dipole pattern with different north-south linear trends in precipitation over the ETP. Song et al. (2016) have found the modest increases in the inner and northeastern TP and significant decreases in the southeastern TP. A simplified regional division of eastern, central, and western TP would eliminate this north-south contrasting feature. Considering that the main focus of the present analysis is the summer heat sources over the CW-TP, where the precipitation does not have such an obvious north-south distribution, we used the ETP as a reference for comparison with the CW-TP. The division of the eastern and western TP is also following most previous studies on the TP heat sources.

2.6. Conclusions

A number of bias-corrected reanalysis datasets, gauge-based observations, and selected satellite data are synthetically utilized to study the climatology, long-term trends and interannual variations of summer (June-July-August) atmospheric heat sources over various sub-regions of the

Tibetan Plateau (TP). Different from most of the previous works that focused on the station-covered eastern TP (east of 85°E), this study pays more attention to the data-sparse western plateau (70° - 85°E).

Total heat source (TH) in an air column comprises local surface sensible heat flux (SH), latent heat released by precipitation (LH), and net radiation flux (RD). we applied different datasets to estimate the different components. First, SH from eight reanalysis resources, including NCEP-DOE R2, CFSR, ERA-Interim, JRA-25, JRA-55, MERRA-2, GLDAS-2, and FLUXNET-MTE, are compared with a station-based new estimation (Yang11) over the central and eastern TP (CE-TP). After correcting the mean bias in each dataset, we chose the top four of them (CFSR, ERA-Interim, MERRA-2, and GLDAS-2), which show better agreement with the climatology and temporal variation of the observation. The merged SH obtained by the ensemble average of the above four sets is most close to the observed new estimation over the CE-TP, thus SH over the WTP can be unprecedentedly reasonable. Due to the good performance of the selected reanalysis datasets, our estimation can possibly be further extended for longer periods, especially for the latest 10 years.

Two gauge-based (PREC/L and APHRODITE) and two merged (GPCP and CMAP) precipitation datasets are averaged to calculate LH. RD is calculated from two satellite resources, GEWEX-SRB and ISCCP. Since they have a large discrepancy at the surface, we prudently select the dataset that is suitable for each radiation component. Consequently, we take the average of SRB and ISCCP for the net radiation at the top of the atmosphere and for the surface downward shortwave radiation, while for other components at surface we apply the SRB-only longwave radiation and the ISCCP-only upward shortwave radiation.

Results show that the climatology of summer TH as well as its three components displays significant spatial inhomogeneity. Consistent with prior studies, SH (LH) typically increases

(decreases) from southeast to northwest over the TP; LH generally dominates TH over most of the TP. The southeast-northwest distribution of LH depends on its summer moisture source that comes from the south and the east. SH has a generally opposite distribution to LH, because the surface of the northwest inland areas with less rainfall can receive more solar radiation. A noteworthy new finding in summer climatology is a minimum TH area over the northwestern TP (around 76°E, 36°N). The radiative cooling there is strong due to the insulation effect of debris-covered Karakoram glaciers on solar radiation, while SH and LH there are relatively small, thus leading to a negative value of TH. In addition, LH is most important role for TH over the CE-TP in July-August, while SH is stronger in June and over the CW-TP. Radiative cooling is largest in August.

Over the long-term period of 1984-2006, TH over the ETP (CTP) has a very slight decreasing (increasing) trend. On the opposite, TH over the WTP is obviously increased due to the rising trend of LH before 1996 and the increasing trend of RD after 1996. The decreasing trend since 1980s and the recovery since early 2000s in SH relied on the corresponding changes of the surface wind speed and ground-air temperature difference. The change of RD is connected to that of the cloud amounts, snow cover, and surface emissivity. The upward or downward tendency in LH is also closely related to the change of snow cover or snow depth. A climatic jump in LH around late 1990s is deemed as a signal of the interdecadal variations in the summer heat sources over the TP.

The year-to-year variation of TH is highly correlated with that of LH over the CE-TP. The TH of WTP is significantly correlated with RD and SH. Correlations of the temporal evolutions of TH among sub-regions of the TP in each month also show great differences. On the interannual scale, TH over the ETP and that over the CTP are highly correlated during the summer rainy season. TH over the CTP and that over the WTP are significantly correlated in July, whereas TH over the WTP and that over the ETP are overall uncorrelated. The significantly different interannual variations of TH over the WTP and over the ETP indicate their potential distinct climate impacts,

which need further investigation. The noticeable subseasonal variation of the interannual variability of heat sources should be taken into account as well since there is little correlation between TH in every month.

As a first attempt to comprehensively investigate the total summer heat source and its three components over the data-sparse CW-TP, this observation-validated study could improve the accuracy in the heat source estimation over the TP, especially the station-void WTP. The results of the interdecadal changes and long-term trends of the heat sources in different sub-regions would enhance our understanding of the potential impacts of climate change on different parts of the TP. The summer heat source over the TP is a very important thermal forcing to the climate system, thus further relevant model evaluations, climate change researches, and future climate predictions could benefit from our new estimates. With the complex topography and climate patterns seen in the TP, there is still a need for a higher station density and more in situ observations in order to fully understand the climate variability in the heat sources over the TP.

Citation: Xie, Z., and B. Wang, 2019. Summer Atmospheric Heat Sources over the Western–Central Tibetan Plateau: An Integrated Analysis of Multiple Reanalysis and Satellite Datasets. *J. Climate*, **32**, 1181-1202, https://doi.org/10.1175/JCLI-D-18-0176.1.

Chapter 3. Different Remote Forcings on the Interannual Variations of Summer Heat Sources across the Tibetan Plateau

3.1. Abstract

Tibetan Plateau (TP) heat source influences summer atmospheric general circulation profoundly. However, its interannual variation is affected by remote forcing from world oceans. The processes governing the variability of the TP heat sources remains controversial and poorly understood. With numerical model experiments, we show that the summer heat source variability is affected by different remote forcings across the TP from east to west. The eastern TP (ETP) precipitation is likely modulated by North Atlantic Oscillation (NAO) and associated SST anomalies through large-scale wave trains propagating from Western Europe to East Asia. On the other hand, the increased central TP (CTP) precipitation heating is primarily driven by a developing La Nina through generating a low-pressure anomaly over northern India, enhancing moisture transport and precipitation heating over the southern CTP. The increased western TP (WTP) sensible heating is linked to the tropical western Pacific cooling, central Pacific warming, and North Atlantic cooling. These anomalous SST conditions produce a high-pressure anomaly over the WTP, raising the ground-air temperature difference, thereby enhancing the sensible heat there. The results suggest that the summer TP heat sources and global climate comprise an interactive system, and the anomalous Pacific and Atlantic conditions have divergent influence on the summer heat source across TP. These conclusions are based on the past 40 years of observations, possible secular change of the forcing mechanism invite further investigation.

3.2. Introduction

The striking impacts of the interannual variability of the TP heat sources on the regional circulation and precipitation have attracted much attention (e.g., Zhao and Chen 2001; Chen et al. 2015; Hu and Duan 2015). However, compared to the plentiful studies working on the TP's thermodynamic effects, much less attention has been paid to the origins of the variations of the TP heating.

During the last decade, increasing number of studies have devoted to find the possible controlling factors for the TP thermal conditions. These factors include, for instance, Indian Ocean Dipole and El Niño/Southern Oscillation (ENSO) (Bothe et al. 2010; Hu et al. 2021), the North Atlantic sea surface temperature anomaly in early spring (Cui et al. 2015), the North Atlantic Oscillation (NAO) (Liu and Yin, 2001; Z. Wang et al., 2018), the western Maritime Continent convection (Jiang et al. 2016), and the May Southern Hemisphere annular mode (Dou et al. 2017).

Each previous study focuses on one or two factor(s) that influence the TP heating, and few works have investigated the different remote forcings for the ETP, CTP, and WTP heating. Particularly, the year-to-year variation of the WTP-sensible heating has been seldom studied. This chapter is devoted to find possible controlling factors for the interannual variations of the ETP, CTP, and especially the WTP summer diabatic heating and explore associated physical mechanisms.

The summer heat source over the TP is dominated by atmospheric condensational latent heating (LH) and surface sensible heating (SH) (Wu et al., 2016; Xie and Wang 2019). Xie and Wang (2019) found that, on the interannual timescale, the total heat variability is highly correlated with LH variation over the CTP and ETP but significantly correlated with SH and net radiation variation over the WTP. However, net radiation consistently exhibits a cooling effect over the whole plateau and the time range of the satellite data for net radiation is relatively short. Thus, we

use precipitation (i.e., LH) and SH to represent the total heat over the CTP/ETP and WTP, respectively.

This chapter is arranged as follows. The datasets and models used in this study are listed in section 3.3. Section 3.4 presents the observed interannual variations in the TP heating and their possible connections with tropical SST and latent heat (i.e., precipitation) anomalies. Section 3.5 shows the numerical experiment results, demonstrating the different causes (i.e., remoter forcings) of the variations in the ETP, CTP, and WTP heating. Section 3.6 presents conclusions and discussion.

3.3. Data and Models

3.3.1. Observational datasets

The atmospheric data (winds and 2-m temperature) are the monthly ERA-Interim data (Dee et al. 2011) at a resolution of 2.5° × 2.5° (1979-2019) from the European Centre for Medium-Range Weather Forecasts. The monthly global precipitation datasets are from the Global Precipitation Climatology Project version 2.3 (GPCP; Adler et al. 2003) at a resolution of 2.5° × 2.5° (1979-present) and Global Precipitation Climatology Centre (GPCC; Schneider et al. 2011) at a resolution of 1° × 1° (1891-2016). The monthly SST data is from Extended Reconstructed Sea Surface Temperature (ERSST) v5 at a 2° × 2° resolution (1854-present) (Huang et al. 2017). The entire TP region (70°E-105°E, 26°E-42°N; above 2500 m) is divided into 3 sub-regions: the western TP (WTP, 70°E-82°E), central TP (CTP, 82°E-92°E) and eastern TP (ETP, 92°E-105°E).

3.3.2. Models

A series of AGCM numerical experiments need to be conducted to justify the diagnostic results from observational data. The AGCM employed in section 3.4.2 is version 4.0 of the

Community Atmosphere Model (CAM4) developed at the National Center for Atmospheric Research (NCAR). The physical parameterization package of CAM4 consists of moist precipitation processes, clouds and radiation processes, surface processes, and turbulent mixing processes. Each process has various components. The precipitation processes include deep convective, shallow convective, and stratiform components. The deep convective processes are parameterized by the revised version of the Zhang–McFarlane convection scheme (Zhang and McFarlane 1995, Neale et al. 2008). The shallow convective process is parameterized following Hack (1994). The Rasch-Kristjansson single moment bulk microphysics parameterization (Rasch and Kristjansson 1998) and the Zhang macrophysics parameterization (Zhang et al. 2003) are adopted to mimic the stratiform processes. A detailed description of CAM4 is given in Neale et al. (2010). In this study, this model is run at a horizontal resolution of 1.9° latitude by 2.5° longitude and has 26 vertical hybrid sigma pressure levels.

A linearized atmosphere general circulation model (AGCM), Linear Baroclinic Model (LBM), which is developed at the University of Tokyo's Center for Climate System Research (Watanabe and Kimoto, 2000), is also utilized. The model is comprised of linearized primitive equations on the sphere with the sigma coordinate. For simplicity, the dry-process version is used in which the physics module is shut down. The model has a horizontal resolution of T42 and 20 sigma levels in the vertical direction. Vorticity and divergence anomaly are subject to Rayleigh friction, and temperature anomaly is subject to Newtonian thermal damping. The damping time scale is set at 1 day for the lowest three levels and the topmost two levels, 5 and 15 days for the fourth and fifth levels, and 30 days elsewhere. Additional biharmonic diffusion (order = 4) with an e-folding decay time of 6 hours is also applied in the model.

The datasets and models mentioned above are used in both Chapter 3 and Chapter 4.

3.4. Observed Interannual Variations of the TP Heat Sources

The summer heat source over the TP is dominated by atmospheric condensational latent heating (LH) and surface sensible heating (SH) (G. Wu et al. 2016; Xie and Wang 2019). From the results in Chapter 2, on the interannual timescale, the total heat is highly correlated with LH over the CTP/ETP and significantly correlated with SH and net radiation (RD) over the WTP. However, RD consistently exhibits a cooling effect over the whole plateau and the time range of the satellite data for RD is relatively short. Therefore, we use precipitation (i.e., LH) and SH to represent the total heat over the CTP/ETP and the WTP, respectively. The GPCC data is used for the TP precipitation because this dataset has the highest correlation with the station observed precipitation data (Wu and Gao 2013) over the CE-TP (1980-2016). Data for SH (from Chapter 2) is extended to the period of 1980 to 2016 by averaging the bias-removed long-range ERA-I and MERRA-2 data in the extended years.

Mean-removed and detrended time series of the extended data (1980–2016) are shown in Fig. 3.1 (a–c). The precipitation in the ETP and CTP has a moderate correlation coefficient of 0.40 ($p < 0.05$, exceeding 95% confidence level), but both of them are uncorrelated with the WTP sensible heat. From the power spectrum analysis (Fig. 3.1 d–f), the JJA heating anomalies over the ETP, CTP, and WTP have quasi-5-year, quasi-4-year, and quasi-2.5-year periods, respectively. These statistically significant periods are on the interannual timescale.

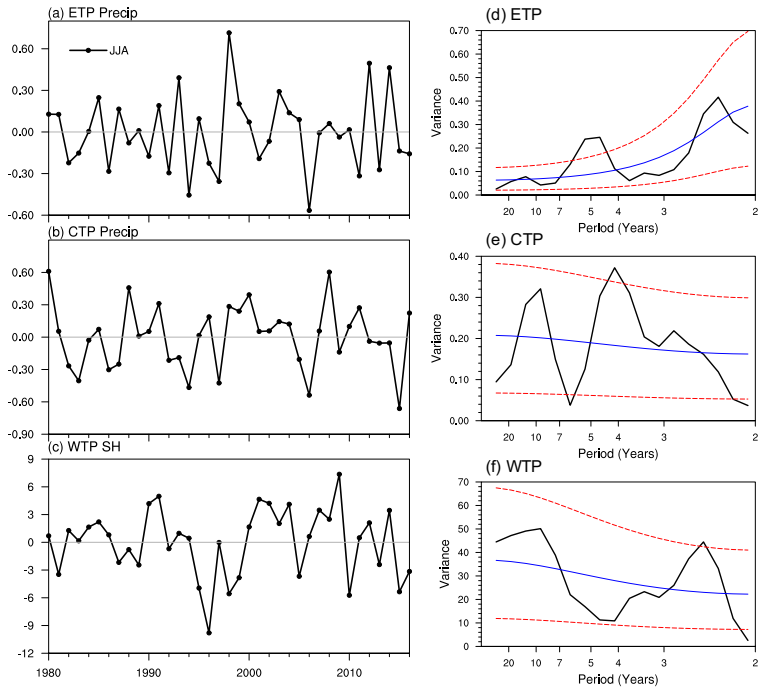

Fig. 3.1. (a–c) Detrended temporal variations of the summer anomalies of (a) precipitation (mm day^{-1}) over the ETP, (b) precipitation (mm day^{-1}) over the CTP, and (c) sensible heat (SH; W m^{-2}) over the WTP. (d–e) The corresponding power spectrum of the JJA heating in each sub-region. Blue lines denote the red noise curve; Red dashed lines indicate the 90% red noise confidence interval.

To find possible tropical-to-midlatitude SSTA origins for the TP heating variations, the lead-lag correlation maps of the global SST and 500 hPa wind anomalies with the detrended JJA TP heating are shown in Fig. 3.2. The TP surface is at around 600 hPa, and 500 hPa winds depicts the low-level circulation over the plateau. Generally, the simultaneous correlation patterns of SST anomalies (SSTA) with the CTP and ETP heating (Fig. 3.2 h, i) are largely different from the correlation pattern with the WTP heating (Fig. 3.2g). The correlation maps of the SST anomalies in the preceding winter (Fig. 3.2 a–c) and spring (Fig. 3.2 d–f) with the TP heating are also shown. The SST-lead correlation patterns over the ETP and CTP are generally similar to the simultaneous patterns, but the simultaneous ones show the highest correlations. For the WTP, the SST-lead correlation shows significant signals in the extratropical Pacific, while the simultaneous correlation displays strong signals in the tropics where typically, the ocean forces the atmosphere.

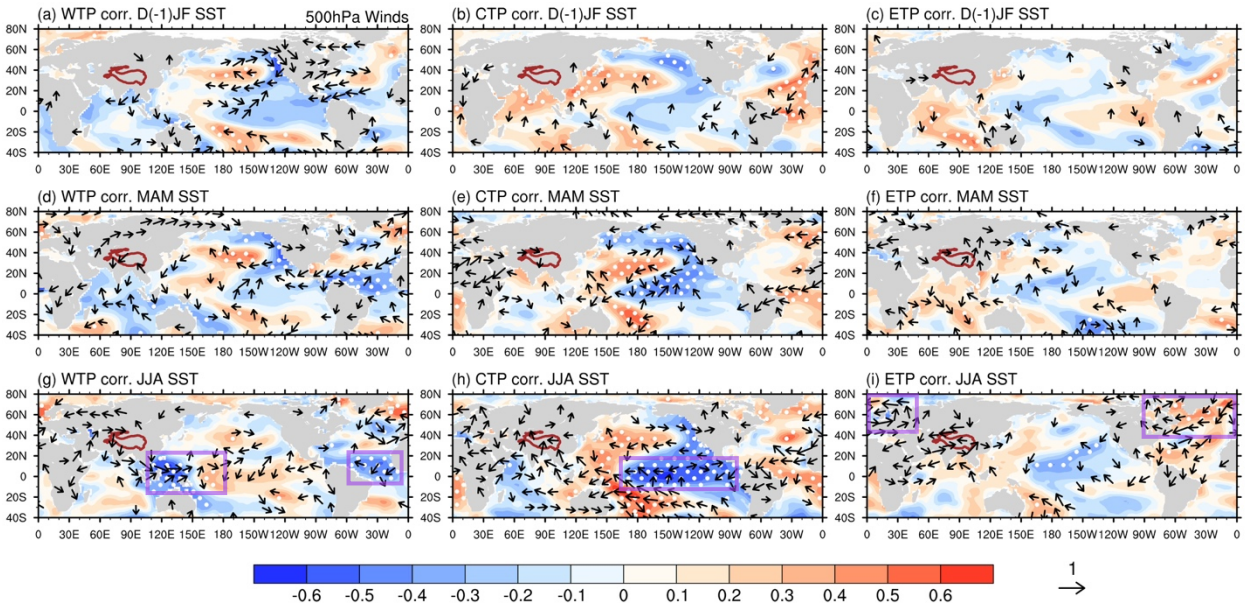

Fig. 3.2. Correlation maps of the SST (°C; shading) and 500 hPa wind (m s^{-1}; vectors) anomalies in (a–c) preceding winter (DJF), (d–e) preceding spring (MAM), and (g–i) simultaneous summer (JJA) with the detrended JJA (a, d, g) WTP, (b, e, h) CTP, and (c, f, i) ETP heating time series. Black dots indicate the correlation coefficients exceed the 95% confidence level. The purple boxes in (g), (h), and (i) denote the key regions of SSTA or circulation that influence the TP heating.

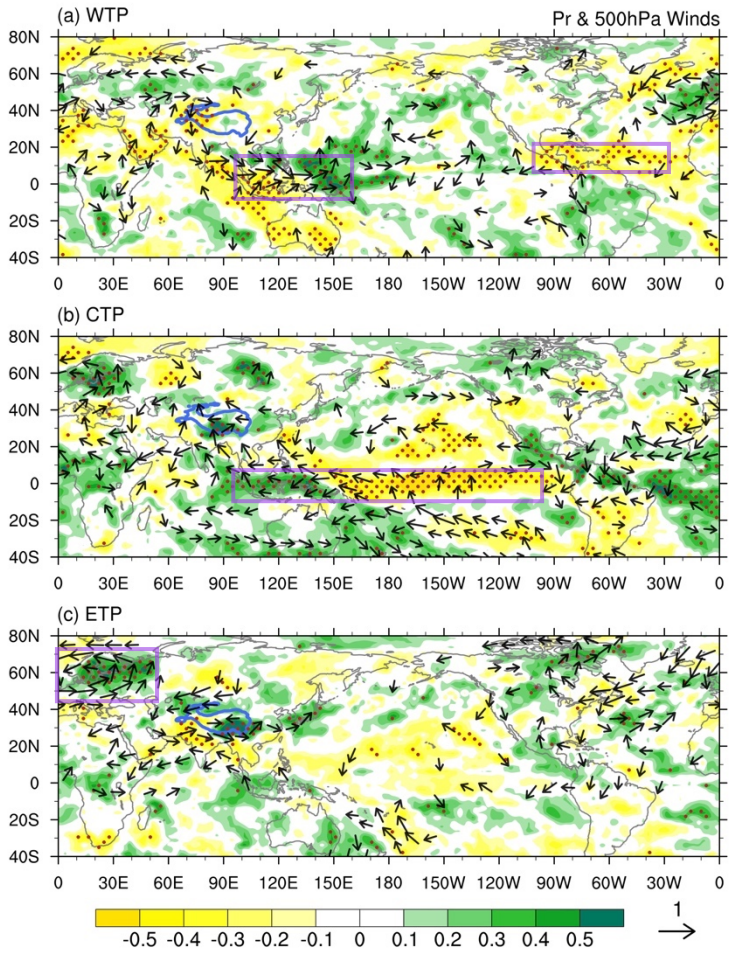

Fig. 3.3. Correlation maps of the JJA precipitation (mm day^{-1}; shading) and 500 hPa wind (m s^{-1}; vectors) anomalies with the detrended JJA (a) ETP, (b) CTP, and (c) WTP heating time series. Black dots indicate that the correlation exceeds the 95% confidence level. The purple boxes in (a), (b), and (c) denote the key regions of tropical convection or mid-latitude circulation that influence the TP heating.

The following analyses focus on the simultaneous correlations. For the Pacific SSTA, the WTP heating is significantly correlated with the tropical western Pacific (WP: 10°S–15°N, 110°E–145°E)-cooling ($r = -0.56$, $p < 0.01$) and central Pacific (CP: 10°S–5°N, 150°E–180°)-warming ($r = 0.38$, $p < 0.05$) (Fig. 3.2g). To see how the TP heating variations are linked to global precipitation heat source, we further present the correlation maps of the global precipitation with the detrended JJA TP heating (Fig. 3.3). The correlation map of precipitation shows a clear dipole pattern with suppressed rainfall in the western Maritime Continent (MC) and enhanced rainfall in the Pacific

warm pool (Fig. 3.3a). A low-level anticyclonic circulation over the WTP is associated with the WTP sensible heating (Fig. 3.2g), which is a key system connecting the remote SSTA forcing and the local sensible heat. The WTP heating is also negatively correlated with the tropical North Atlantic (TNA: 0°–20°N, 60°W–10°W) SSTA ($r = -0.52$, $p < 0.01$) (Fig. 3.2g) and precipitation anomalies (Fig. 3.3a), indicating another possible remote forcing for the WTP heating variation. Numerical model experiments will be conducted to examine the effects of the SSTA in these two regions on the WTP sensible heating.

For the CTP heating, the tropical Pacific SSTA shows a strong La Niña-like pattern (Fig. 3.2h). The CTP precipitation is also strongly connected with enhanced rainfall in the MC and depressed precipitation in the equatorial Pacific (Fig. 3.3b), which are coordinated by the La Niña condition. The JJA CTP heating and Niño 3.4 index has a high, negative correlation coefficient of -0.60 (exceeds 99% confidence level). During the developing summer of several strong El Niño events (i.e., 1982, 1987, 1997, 2015), the CTP experienced anomalous dryness. From the correlation map of the TP summer rainfall with the Niño 3.4 index (Fig. 3.4a), the Niño 3.4 index is significantly correlated with the precipitation over the CTP, especially the southern CTP, whereas over the ETP and WTP, the correlation is relatively weak. The regressed low-level circulation pattern against Niño 3.4 index (Fig. 3.4b) suggests that El Niño may generate anomalous northwesterlies to the south of the CTP, weakening southerly monsoon and reducing the moisture transported to the plateau. On the other hand, La Niña-type of SSTA produces anomalous southerlies to the south of the CTP (Fig. 3.2h), enhancing precipitation over the southern CTP (Fig. 3.3b). These results suggest the potentially strong influence of ENSO on the CTP summer heating (i.e., precipitation). The mechanism of how ENSO affects CTP precipitation needs to be further testified by numerical experiments.

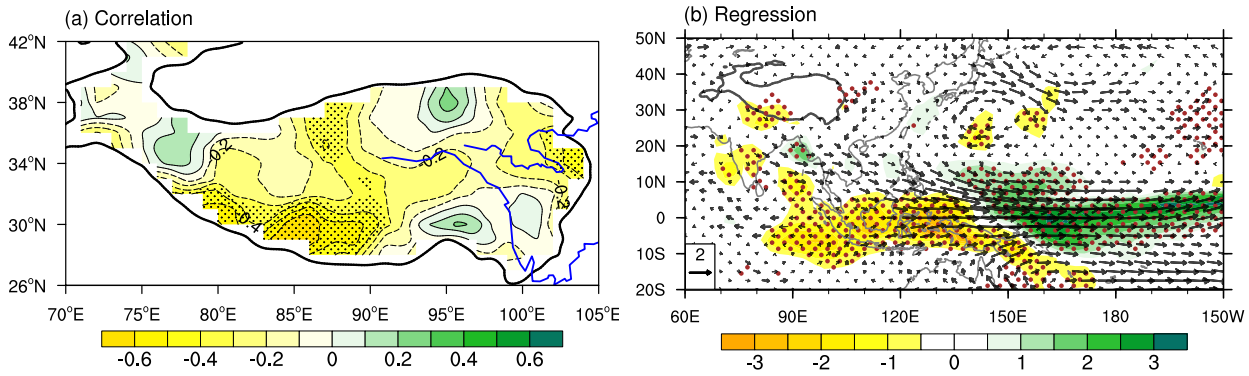

Fig. 3.4. (a) Correlation map of the JJA TP precipitation anomalies with the detrended JJA Niño 3.4 index. (b) Regression of the precipitation (shading; mm day^{-1}) and 700 hPa winds (vectors; m s^{-1}) anomalies against the detrended JJA Niño 3.4 index. Black dots in (a) and brown dots in (b) indicate the values exceeding the 95% confidence level. Bold vectors denote the values of either zonal or meridional wind components exceeding the 95% confidence level. The blue curves in (a) denote a section of the Yangtze River (south) and Yellow River (north).

The correlation between the ETP heating and tropical SSTA is relatively weak, but the ETP heating is positively correlated with the high-latitude North Atlantic SSTA, which is connected with the northern node in the negative phase of the summer NAO (Fig. 3.2i). The summer NAO has a relatively smaller spatial extent and is located farther northward with its southern node over northwestern Europe (Folland et al. 2009). The ETP heating is significantly correlated with the upstream northwestern European precipitation (Fig. 3.3c) that is corresponding to the southern node of the summer NAO. The ETP precipitation anomaly has a significant correlation ($r = 0.48$, $p < 0.01$) with the negative summer NAO index (Fig. 3.5c). From the regression pattern of circulation against the negative summer NAO index (Fig. 3.5 a, b), the summer NAO could generate a large-scale wave train propagating from northwestern Europe to East Asia, inducing an upper-level anomalous anticyclonic circulation over the southeastern TP. The vertical baroclinic structure and the pumping effect of the TP are strengthened over the southeastern TP through the southeastward propagation of wave disturbance, thereby enhancing the precipitation. This result is consistent with the previous studies on the linkage between the summer NAO and the ETP

precipitation (Liu and Yin 2001; Z. Wang et al. 2018).

We further calculated the lead-lag correlation coefficients between the ETP heating and summer NAO index. It is found that April-May-June (AMJ) and May-June-July (MJJ) NAO index has a highest negative correlation of -0.49 ($p < 0.01$) with the JJA ETP heating, suggesting that NAO may lead the ETP precipitation in summer by up to two months.

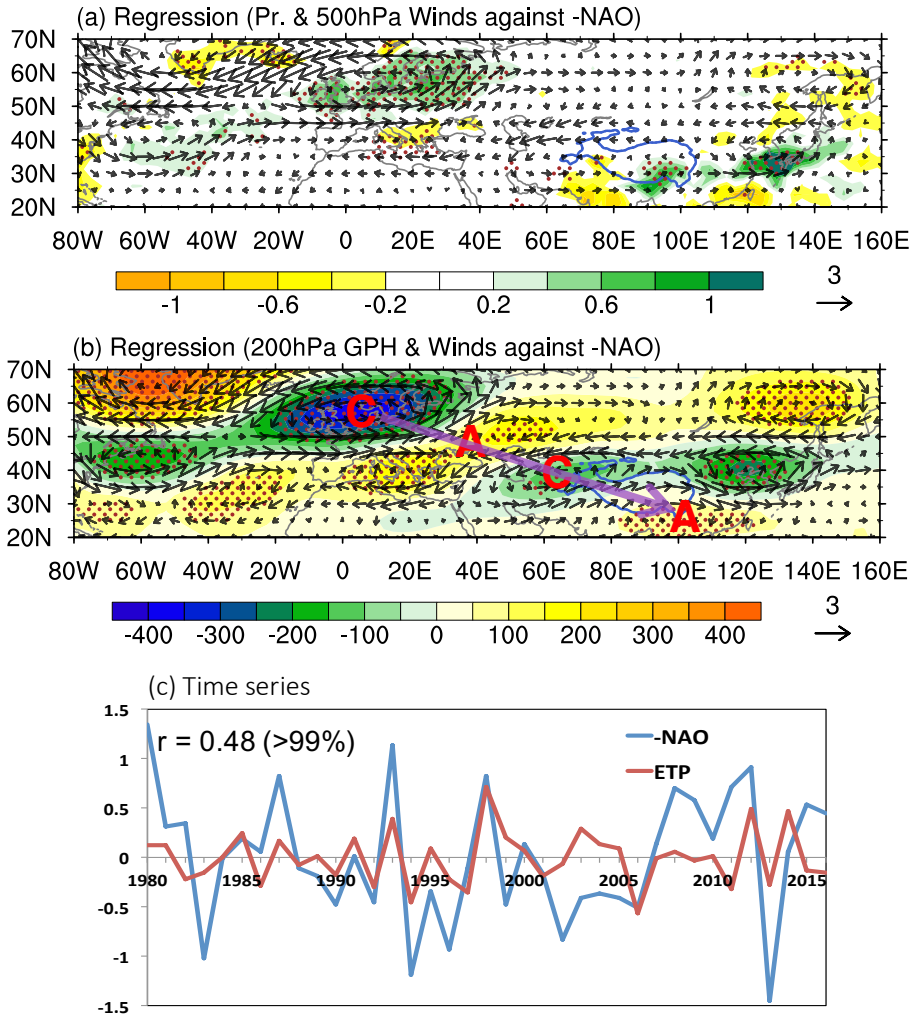

Fig. 3.5. (a) Regression of precipitation and 500hPa wind anomalies against the detrended negative summer NAO index. (b) Regression of 200 hPa geopotential height and wind anomalies against the detrended negative summer NAO index. The symbols "C" and "A" in (b) denote cyclonic and anticyclonic circulations, respectively. Then purple arrow indicates the wave train propagating from western Europe to southeastern TP. (c) Year-to-year evolutions of the ETP heating anomaly (red line) and the negative summer NAO index (blue line).

3.5. Causes of the Interannual Variations

In order to explore the drivers for the interannual variability, numerical experiments are conducted to assess the influences of the tropical SSTA on the TP heating. The SSTA sensitivity run is an AGCM (CAM4) experiment with prescribed SSTA (plus climatological SST) forcing. One sensitivity experiment comprises 30 ensembles starting with different initial conditions. Each ensemble member runs from May 1st to August 31st, and the SSTA is added in JJA. The output differences between the SSTA run and control run are considered the model-simulated atmospheric responses to the SSTA forcing. Control run is forced by climatological SST.

Figure 3.6 shows the comparison between the observation and the simulated JJA climatology in the AGCM control run. The model can generally simulate the observed precipitation and low-level circulation patterns. Note that the simulated precipitation is much higher (lower) than the observation in the southern slope of the TP and eastern Arabian Sea (eastern Bay of Bengal), because the simulated southwest monsoon that transports moisture is located westward compared to the observation. This may need attention when interpreting the experiment results.

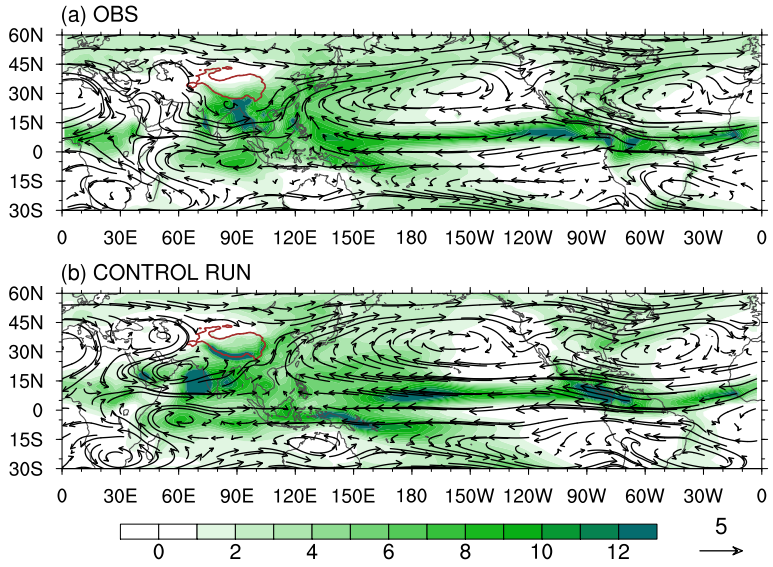

Fig. 3.6. The 1980–2016 JJA climatology of precipitation (shading; mm day^{-1}) and 700 hPa winds (vectors; m s^{-1}) in (a) observation and (b) AGCM control run.

3.5.1. CTP heating controlled by El Niño

The result in Section 3.4 suggests that El Niño could be a major influential factor for the CTP latent heating (i.e., precipitation), so an AGCM experiment of El Niño run is conducted. The prescribed El Niño SSTA pattern in JJA is shown in Fig. 3.7. The seasonal averaged SSTA is added onto the climatological SST forcing in three summer months.

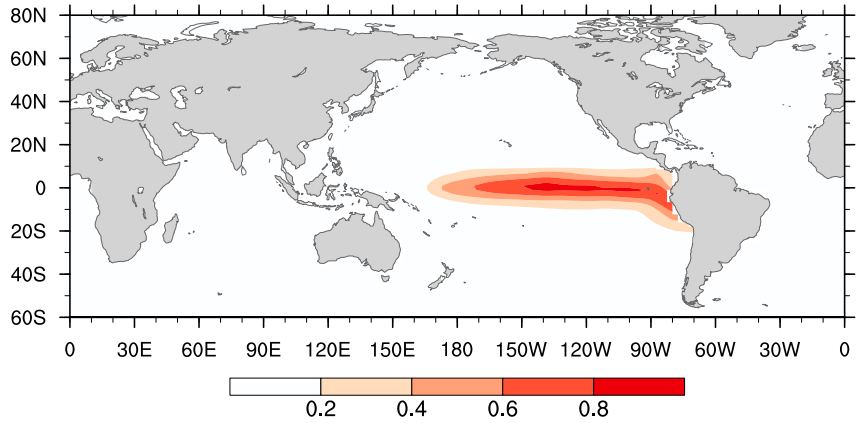

Fig. 3.7. SSTA forcing pattern (units: K) of El Niño run from the regression of the tropical eastern Pacific SST anomalies against the standardized JJA Niño 3.4 index.

The difference between the El Niño run and the control run shows reduced JJA precipitation in the south slope of the TP (Fig. 3.8a). The observed rainfall in the south-central TP has a significantly negative correlation with El Niño (Fig. 3.4a), and the model result is roughly consistent with the observed precipitation anomalies shown in Fig.3.4(a), although the simulated dry area is more southward and extends to the east. A strong anomalous rain band is generated to the south of the TP (Fig. 3.8a). The monsoon trough is strengthened to the south, and the large-scale anomalous anticyclonic ridge to the south of the TP prevents northward moisture transport, reducing precipitation over the south slope of the CTP. This high-pressure ridge is connected with the intensified and westward-extended subtropical high. The center of reduced rainfall corresponds to the positive 400 hPa vertical pressure velocity center (Fig. 3.8b), indicating that the weakened ascending motion is the major reason for the suppressed precipitation. The tropical eastern Pacific

warming induces a pair of upper-level anticyclonic circulations to the east of the warming area, generating a wave train propagating to mid-latitude (Fig. 3.8c). In this wave train, an anomalous cyclonic circulation is located to the north of the TP, and an anomalous anticyclonic circulation is induced over the south flank of the central-eastern TP, favoring anomalous subsidence over the south slope of the CTP.

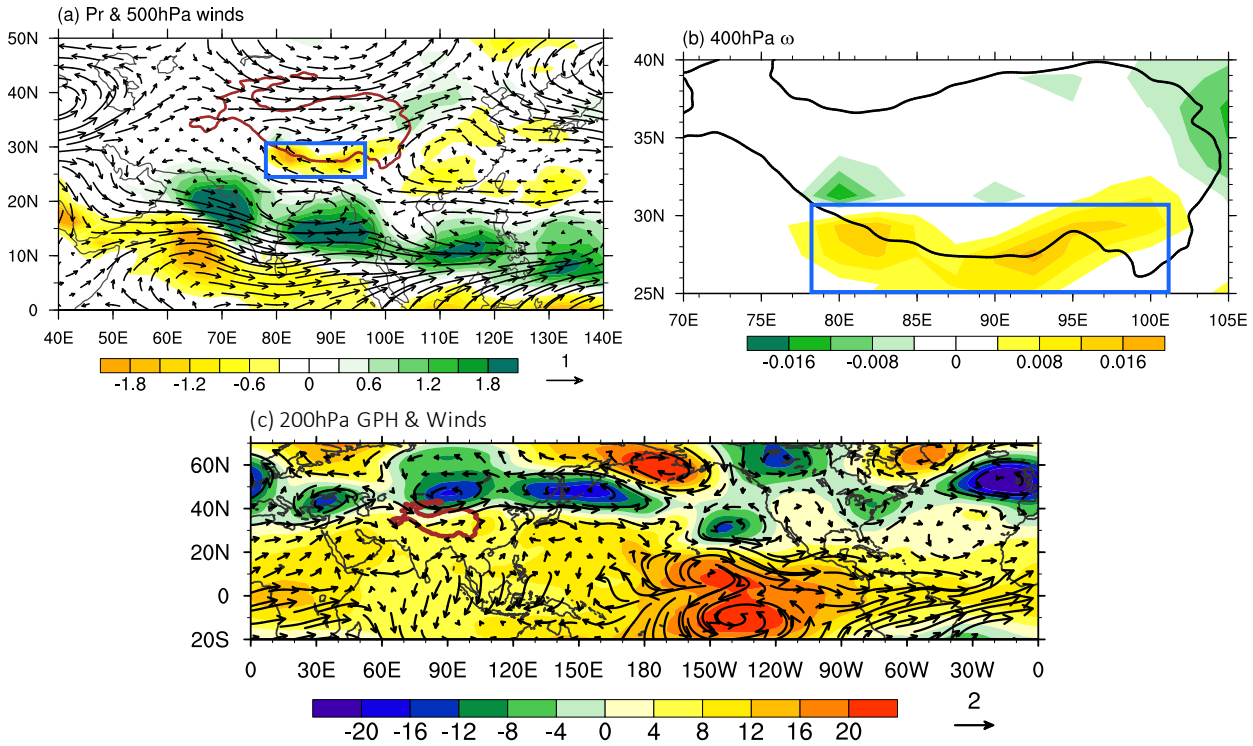

Fig. 3.8. (a) Responses of the JJA precipitation (shading; mm day^{-1}) and 700 hPa winds (vectors; m s^{-1}) to El Niño SSTA forcings. (b) Responses of the JJA 400 hPa vertical pressure velocity (Pa s^{-1}) over the TP to El Niño SSTA forcings. (c) Responses of the JJA 200 hPa geopotential height (shading; m) and winds (vectors; m s^{-1}) to El Niño SSTA forcings.

3.5.2. WTP heating regulated by tropical western Pacific cooling-central Pacific warming

Figure 3.2 (g) indicates a significant correlation between the WTP sensible heating (SH) and the tropical WP cooling-CP warming in JJA. Thus, a WP cooling-CP warming run and an opposite WP warming-CP cooling run by CAM4 are conducted to verify this observed correlation. The half of the difference between these two runs is the response to the SSTA forcing. The SSTA dipole in

the tropical Pacific is prescribed as shown in Fig. 3.9, which is from the regression of SSTA against the WTP heating. We confined the SSTA forcing in the equatorial region (-10°S – 5°N) because to the north of 5°N in the western Pacific (i.e., South China Sea and the Philippine Sea), the atmosphere and ocean are interactive where we cannot assume the ocean is driving the atmosphere.

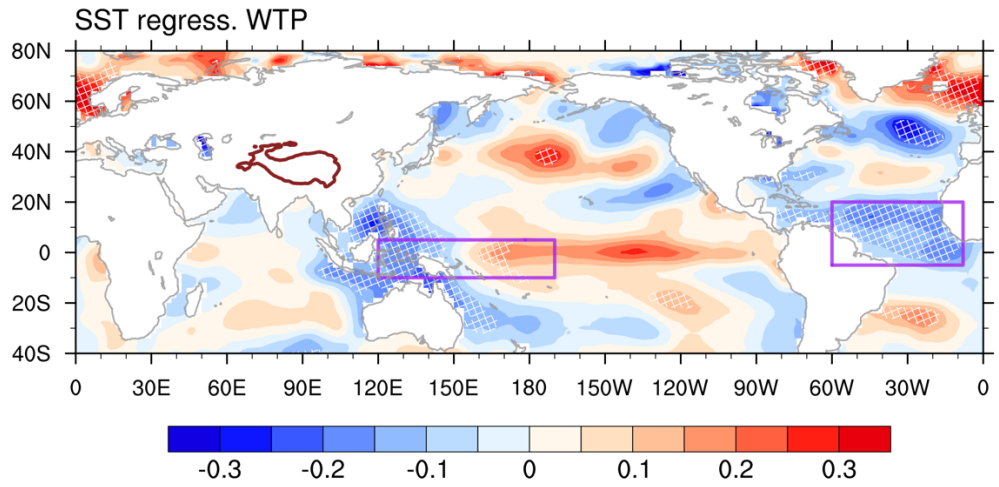

Fig. 3.9. Regression of global SSTA (°C) against the standardized JJA WTP heating time series. White hatching denotes the values exceeding the 95% confidence level. The purple rectangular frame in the tropical Pacific encloses the location and pattern of the SSTA forcing for the WP cooling-CP warming run. The purple frame in the Atlantic denotes the SSTA forcing for the tropical North Atlantic cooling run in section 3.5.3. The SSTA would be doubled in magnitude and then put into the models as the prescribed forcing.

The precipitation response is first examined to see the local atmospheric heating response to the SSTA. It shows suppressed rainfall in the maritime continent and enhanced rainfall in the western-central Pacific (Fig. 3.10c), which is roughly consistent with the observed rainfall dipole pattern shown in Fig. 3.3(c) although the location is relatively eastward. Accompanied with the precipitation response, a large-scale cyclonic circulation is produced to the south of the TP, and a large-scale low-level anticyclonic circulation is generated over the WTP (Fig. 3.10c).

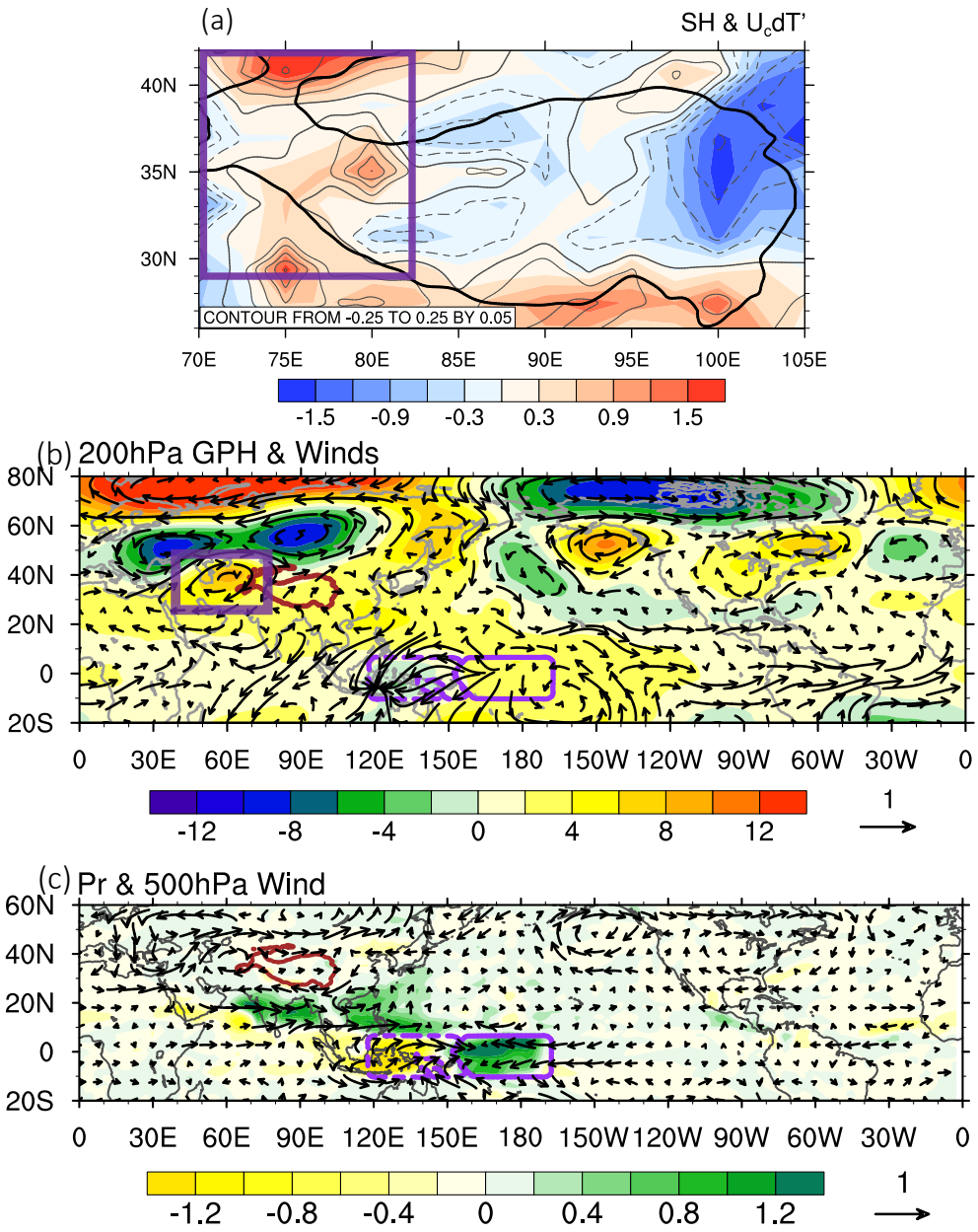

Fig. 3.10. (a) Responses of the JJA surface sensible heat flux (shading; SH: W m^{-2}) and the product of ground-air temperature difference anomaly (dT') and climatological surface wind speed from control run (contours; dT'×U_c: °C m s^{-1}) to the tropical Pacific SSTA dipole forcing. The deep purple box in (a) denotes the area of WTP. (b) Responses of the JJA 200 hPa geopotential height (shading; m) and winds (vectors; m s^{-1}) to the Pacific forcing. The deep purple box in (b) marks the high pressure over the WTP. (c) Responses of the JJA precipitation (shading; mm day^{-1}) and 500 hPa winds (vectors; m s^{-1}) to the Pacific forcing. The purple curves in (b) and (c) denote the location of the WP cooling (dashed line)-CP warming (solid line).

The JJA SH is enhanced in most areas of the WTP (Fig. 3.10a), which is consistent with the observed correlation result. The SH response pattern well matches the response pattern of the product of ground-air temperature difference anomaly and climatological surface wind speed (Fig. 3.10a), indicating that the SH anomaly is dominated by the anomalous gourd-air temperature difference. The circulation responses exhibit an anomalous barotropic high-pressure system over the WTP (Fig. 3.10 b, c). We also examined the responses of ground surface temperature (T_s) and surface air temperature (T_{as}), separately. Both T_s and T_{as} increase but T_s increases more (figure not shown), inducing greater ground-air temperature difference. During the dry, sunny days under high pressure, the surface can receive more solar radiation that raises the ground-air temperature difference, thereby enhancing the SH over the WTP.

Figure 3.3(a) shows that the WTP heating is correlated with a dipole pattern with suppressed rainfall in the western MC and enhanced rainfall in the Pacific warm pool. An idealized experiment using LBM is conducted to testify the direct response of the circulation to the heating forcing from such a convection dipole. The forcing's spatial pattern and vertical profile are depicted in Fig. 3.11, in which the pattern mimics the regression pattern of precipitation against the WTP heating time series. The experiment is run with the JJA mean flow.

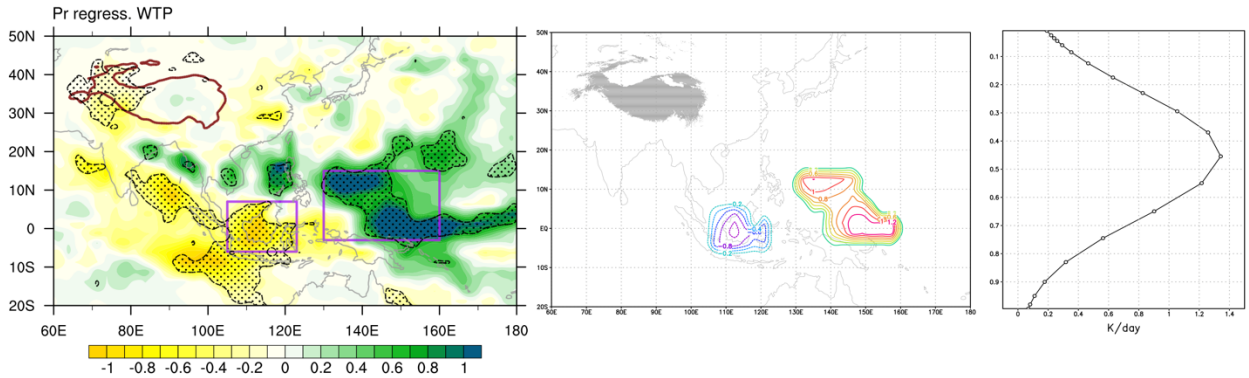

Fig. 3.11. [Left] Regression of the JJA precipitation against the standardized WTP heating. [Center] Spatial pattern of the western Maritime Continent cooling-western Pacific heating forcing for the LBM experiment. [Right] Vertical profile of the heating forcing (maximum 1.3 K day^{-1} at sigma level = 0.45).

The result shows that a strong southeast-northwest tilted low-level cyclonic circulation is generated to the north of the dipole heating, exciting a large-scale wave train propagating along the great circle over the North Pacific Ocean (Fig. 3.12). The tilted cyclone can reach the southeastern TP. An anticyclonic circulation is produced to the northwest of the tilted cyclone, which is located over the WTP. Consistent with the AGCM result, the anomalous anticyclone over the WTP could regulate the in-situ sensible heating.

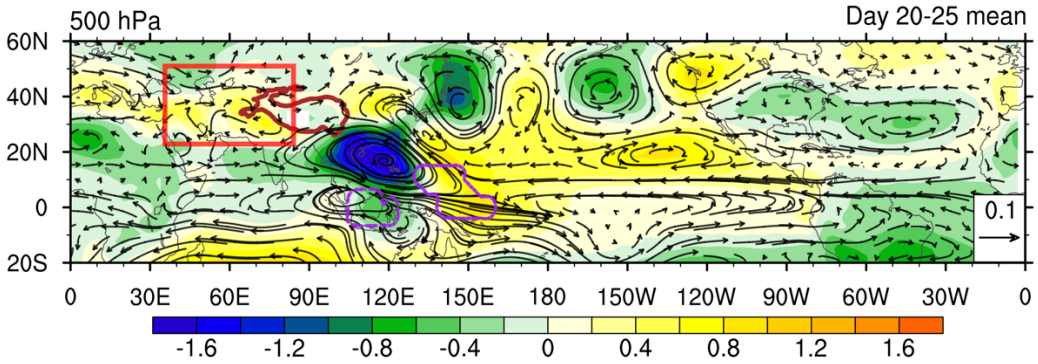

Fig. 3.12. Steady responses (Day 20 to Day 25 mean) of 500 hPa geopotential height (shading; m) and winds (vectors; m s^{-1}) to the western Maritime Continent cooling-western Pacific heating forcing in JJA. The purple curves denote the location of the forcing. The red box depicts the high-pressure response over the WTP.

3.5.3. WTP heating regulated by tropical North Atlantic cooling

Figure 3.2 (g) also suggests a negative correlation between the WTP SH and the tropical North Atlantic (TNA) SSTA. A TNA cooling run and an opposite TNA warming run are conducted, with the prescribed SSTA forcing shown in Fig. 3.9. The model response is represented by half of the difference between these two runs. The result shows that the WTP SH is generally strengthened associated with the elevated ground-air temperature difference (Fig. 3.13a). The local precipitation response to the TNA cooling is an anomalous dryness in the tropical Atlantic (Fig. 3.13c), which is roughly consistent with the observed correlation result though the observed dry region is located relatively northward (Fig. 3.3a). The upper-level circulation response displays a notable wave train propagating along the great circle over the North Atlantic and Eurasian continent, producing an

anticyclonic high-pressure system over the WTP (Fig. 3.13b), thereby leading to the increases in ground-air temperature difference and sensible heat.

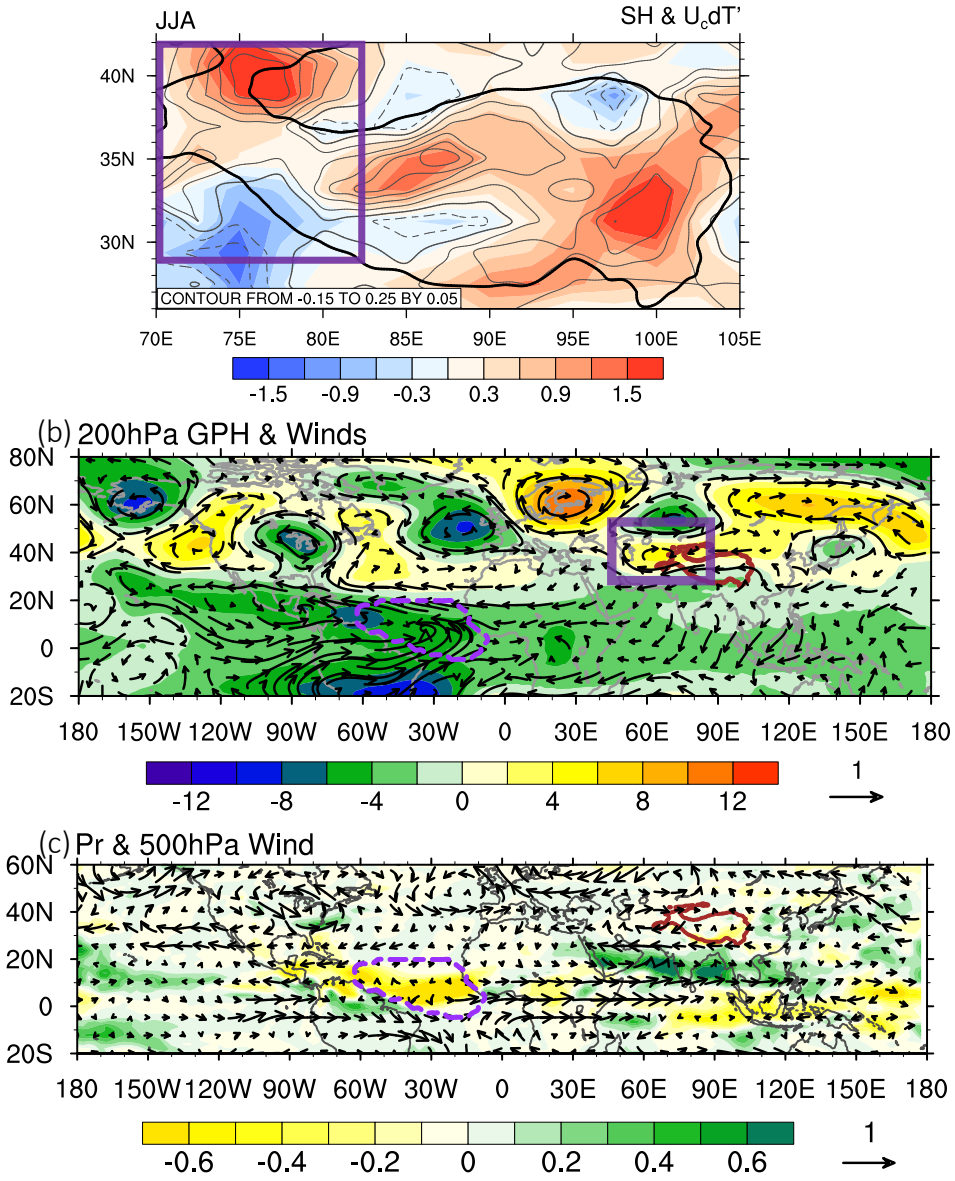

Fig. 3.13. (a) Responses of the JJA surface sensible heat flux (shading; SH: W m^{-2}) and the product of ground-air temperature difference anomaly (dT') and climatological surface wind speed (contours; dT'×U$_c$: °C m s^{-1}) to the tropical North Atlantic (TNA) cooling. (b) Responses of the JJA 200 hPa geopotential height (shading; m) and winds (vectors; m s^{-1}) to the TNA cooling. The deep purple box in (b) marks the high pressure over the WTP. (c) Responses of the JJA precipitation (shading; mm day^{-1}) and 500 hPa winds (vectors; m s^{-1}) to the TNA cooling. The purple dashed curve in (b) and (c) denotes the location of the TNA cooling.

3.6. Conclusions and Discussion

Using the newly developed heat source dataset and conducting several numerical model experiments, the effects of different remote forcings on the interannual variations in the summer heat sources over the western, central, and eastern TP are respectively explored. The JJA heating anomalies over the ETP, CTP, and WTP have quasi-5-year, quasi-4-year, and quasi-2.5-year periods, respectively (Fig. 3.1 d–f).

Observational results show that the simultaneous correlations with the SST anomalies are largely different between the ETP/CTP and WTP heating (Fig. 3.2 g–i). The JJA ETP heating has a negative correlation with the summer NAO index ($r = -0.48$, $p < 0.01$). The summer NAO, with its southern node over northwestern Europe, can generate a large-scale wave train propagating downstream to the ETP, affecting the ETP rainfall variability (Fig. 3.5).

The CTP heating is closely linked with a La Niña-like SSTA pattern in the tropical Pacific Ocean (Fig. 3.2h). The Niño 3.4 index is well correlated with the precipitation over the CTP ($r = -0.60$, $p < 0.01$), especially the south-central TP (Fig. 3.4a), while its correlation with the ETP and WTP rainfall is relatively weak. The CTP precipitation is also correlated with the El Niño-induced, enhanced precipitation in the Maritime Continent (MC) and depressed precipitation in the equatorial Pacific (Fig. 3.3b). The AGCM experiment result shows that the tropical eastern Pacific warming induces strong anomalous subsidence in the south slope of the CTP, thereby suppressing the latent heating released from precipitation over there (Fig. 3.8). Meanwhile, the southerly monsoonal winds are weakened during the El Niño developing summer and the anomalous rain band produced to the south of the TP prevents moisture from being transported further northward to the Plateau. On the other hand, La Niña can produce anomalous southerlies to the south of the CTP (Fig. 3.2h), enhancing precipitation over the southern CTP (Fig. 3.3b). It could be concluded that ENSO is an important origin for the interannual variations of the CTP latent heating.

The WTP heating is significantly correlated with the tropical western Pacific (WP) cooling and central Pacific (CP) warming (Fig. 3.2g) and it is connected with the suppressed (enhanced) rainfall in the western MC (Pacific warm pool) (Fig. 3.3a). Besides, the WTP heating is negatively correlated with tropical North Atlantic (TNA) SSTA ($r = -0.52$, $p < 0.01$) (Fig. 3.2g), suggesting another influential factor for the WTP heating variability. Model results verify that both the WP-cooling/CP-warming and the TNA cooling can enhance the WTP sensible heating through large-scale wave trains, generating an anomalous high-pressure system over the WTP, thus elevating the ground-air temperature difference and the sensible heating over there.

Since the WTP is regulated by the tropical SSTA in two basins, we conduct an extra experiment with both the WP-cooling/CP-warming and the TNA cooling prescribed as forcing (figures not shown). The model result, however, shows reduced SH over the WTP, which is inconsistent with the observation. It is possibly because the effects of the two SSTA forcings cancel each other out when prescribed together into the model. More experiments need to be taken to further examine the combined effect of these two SSTA forcings on the WTP sensible heating.

Compared to the SH response shown in most areas of the WTP region, the precipitation response to the SSTA forcing is notable in the southern part of the CE-TP. Since the major moisture source for the TP is coming from the southerly summer monsoon, the sub-region area-mean precipitation variability is dominated by the precipitation of the southern TP. Thus, it is acceptable to use the sub-region area-mean to represent the dominant precipitation variability of the southern TP. The reason why CTP and ETP precipitation are affected by different remote forcings is possibly related to their different moisture transport paths, which requires further investigation.

The current study is based on a coarse-resolution (1.9° latitude × 2.5° longitude) AGCM, so some results may not be very accurate. For instance, the CTP precipitation response to the El Niño warming is confined to the south slope of the Plateau, but the observation analysis shows that the

rainfall in most areas of the CTP is significantly correlated with the Niño index. The coarse-resolution model may have difficulty in simulating the processes associated with the complex topography. Further experiments using a high-resolution model are needed to examine the current results. Moreover, the air-sea interaction is not included in the AGCM. For the WTP heating, the air-sea interaction in the South China Sea and the Philippine Sea could be an important influencing factor. Therefore, the coupled model experiments can be conducted to investigate the role of air-sea interaction in affecting the TP's heating variability.

Chapter 4. Impacts of the Interannual Variations in Summer Heat Sources over the Tibetan Plateau

4.1. Abstract

The impacts of the interannual variations in summer heat sources over the eastern, central, and western TP are investigated by observational analyses and numerical model experiments. The ETP, CTP, and WTP heat sources have different impacts on regional climate and teleconnection. Observational results show that the ETP heating is connected with a northwestern-Asia warming center and a western-Europe cooling center; the CTP heating is related to a northeastern Asia warming and an East Asia cooling; the WTP heating is linked to the warming in southeastern China and the polar region of Asia. The linear wave-train responses to the ETP, CTP, and WTP heating forcings are notably different. The ETP (CTP) heating generates an upper-level wave train propagating eastward to the northwestern (north-central) Pacific. Both the wave responses to ETP and CTP heating are guided by the subtropical westerly jet. For the WTP heating, the wave train splits into two branches: the northern one propagates northeastward to the Arctic region and the southern one propagates eastward to coastal northwestern Pacific. The locations of the two split anticyclonic circulations roughly correspond with the locations of the observed WTP-heating related upper-level anticyclones and near-surface warming in southeastern China and polar Asia. The anomalous upper-level anticyclone generated by the TP heating may induce anomalous subsidence and reduce the cloud formation, increasing the incoming shortwave radiation and thereby warming the near-surface air.

4.2. Introduction

Compared to the early researches that mainly focus on the climatological roles of the TP heat source, recent works pay more attention to the remarkable impacts of the interannual variability in the TP heat sources on the variations of the circulation and precipitation in surrounding regions (Zhao and Chen 2001; Liu et al. 2002; Chen et al. 2015; Hu and Duan 2015). The TP anomalous heating in spring can exert a delayed effect on the summer weather and climate anomalies in East Asia (Hsu and Liu, 2003; Wang et al. 2014). The TP excessive surface heating can also affect the 'upstream' climate to the west of the TP through the intensified and westward-extended South Asian High and the Rossby wave responses to the heating (Lu et al. 2018).

The influences of the interannual variations in the ETP and CTP heating on climate have been extensively studied. However, the distinct role of the heat source over the western TP (where observational data is scarce) in the climate system has recently been documented but still poorly understood. In previous studies, the snow cover is often used as a proxy of the thermal condition of the WTP. The WTP snow cover may affect interannual variations of summer Eurasian heatwaves through a southern Europe-northeastern Asia (SENA) teleconnection (Z. Wu et al. 2016), and the winter or spring snow cover anomalies over the WTP exert time-lagged impact on East Asian summer monsoon by modulating moisture transport to Eastern China (Xiao and Duan 2016). The current knowledge on the climate impacts of the WTP heating is still limited and distinguishing the role of the WTP and CE-TP heating in the regional and global climate systems is critical for evaluating climate models' fidelity and improving climate prediction. Hence, based on the newly developed reliable estimate of the heat sources over the entire TP (from Chapter 2), this chapter aims to explore the different climate impacts of the interannual variations in the WTP, CTP, and ETP heating and to find possible physical processes associated with the TP heating's effects on teleconnections.

4.3. Methods

The linear regression and partial regression methods are adopted to investigate the possible impacts of the TP heating's year-to-year variations on surface air temperature and teleconnections (Y). In multiple regression (Equation 4.1), $\hat{Y}$ denotes predicted values of Y; b_0 denotes the intercept term when X_1, X_2 and X_3 are all 0; and b_1, b_2 and b_3 denote the partial regression coefficients of X_1, X_2 and X_3, respectively. The partial regression coefficient measures the change in $\hat{Y}$ per unit change in some specific predictor, with other predictors held constant. In this chapter, X_1 is the TP heating, and X_2 and/or X_3 are other factors affecting the TP heating. b_1 is the partial regression coefficient used for analysis.

$$\hat{Y} = b_0 + b_1X_1 + b_2X_2\ (+b_3X_3), \tag{4.1}$$

Considering that the effect of El Niño (NAO) on the CTP (ETP) heating may influence the linear regression pattern against the CTP (ETP) heating, we use the partial regression coefficients with the effect of the JJA Niño 3.4 (negative NAO) index signal being removed. Similarly, for the WTP heating, we use the partial regression coefficients by removing the effects of the JJA negative western Pacific (WP: 10°S–15°N, 110°E–145°E) SSTA index and the JJA negative tropical North Atlantic (TNA: 0°–20°N, 60°W–10°W) SSTA index.

4.4. Observed temperature and teleconnection associated with the TP Heat Source Variations

Linear and partial regression coefficients of the 2-meter air temperature and 200 hPa wind anomalies against the JJA TP heating are shown in Fig. 4.1 and 4.2, respectively. The linear regression results (Fig. 4.1) showed that the anomaly patterns associated with the ETP heating and CTP heating are similar, both having a warming center in northwestern Asia and a cooling center in western Europe, whereas the WTP heating is linked to a northwestern Asian cooling. The ETP

heating is also connected with an eastern Asian cooling. The surface warming (cooling) centers correspond to the upper-level anticyclonic (cyclonic) circulation centers. These centers form a wave train propagating from western Europe to western TP (Fig. 4.1b) or East Asia (Fig. 4.1c).

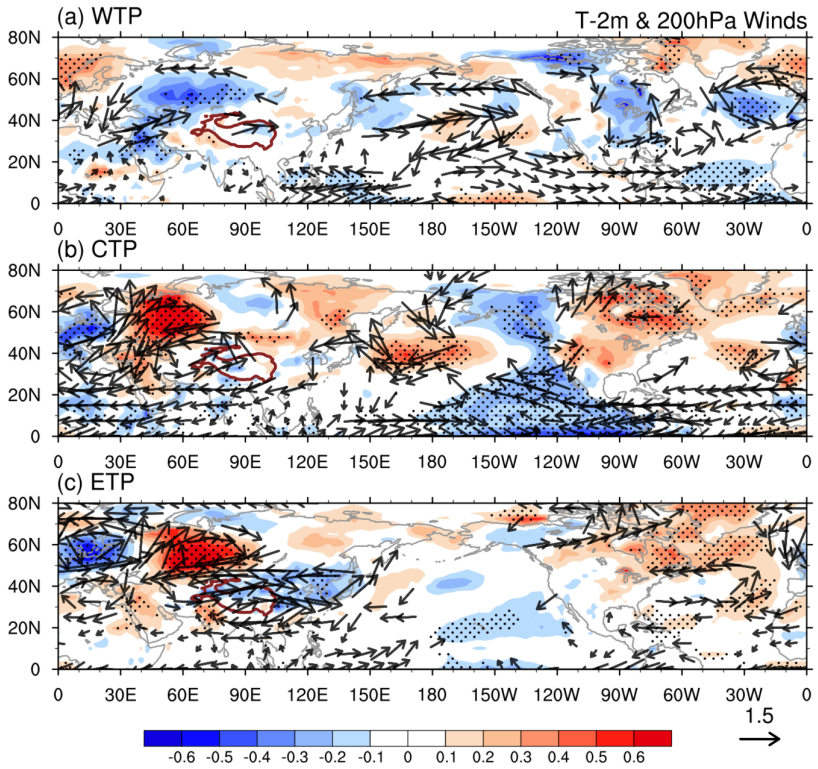

Fig. 4.1. Linear regression of the JJA 2-m temperature (°C; shading) and 200 hPa wind (m s^{-1}; vectors) anomalies against the detrended and standardized (a) WTP heating, (b) CTP heating, and (c) ETP heating. Only the vectors with values of either zonal or meridional wind component exceeding the 90% confidence level are plotted. Black dots indicate the shading values exceed the 90% confidence level.

The partial regression results (Fig. 4.2) are quite different from the linear regression. One common feature in all three patterns (Fig. 4.2 a–c) is the notable easterlies to the south of the TP (around 20°N), which are associated with a large-scale anticyclonic circulation anomaly (same location as South Asia High). After removing the effects of WP and TNA cooling, the WTP heating is associated with the warming in southeastern China and the polar region of Asia (Fig. 4.2a). The WTP sensible heating (SH) is negatively correlated with the WTP snow cover ($r = -0.44$, $p < 0.05$). Z. Wu et al. (2016) found that reduced WTP snow cover (associated with the enhanced WTP SH)

can intensify southern Europe and northeastern Asia heat waves. The result of the WTP partial regression here is quite different from their result, probably because the variability in SH cannot be completely represented by the snow cover.

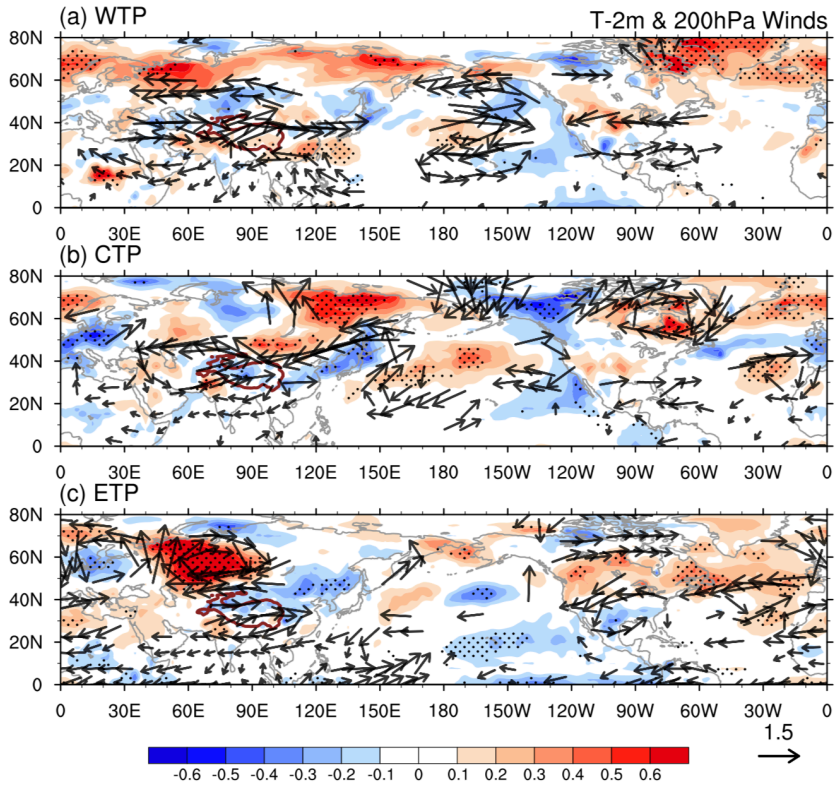

Fig. 4.2. Partial regression coefficients of the JJA 2-m temperature (°C; shading) and 200 hPa wind (m s^{-1}; vectors) anomalies against the detrended and standardized (a) WTP heating (removing western Pacific SSTA index signal and tropical North Atlantic SSTA index signal), (b) CTP heating (removing Niño 3.4 index signal), and (c) ETP heating (removing NAO index signal). Only the vectors with values of either zonal or meridional wind component exceeding the 90% confidence level are plotted. Black dots indicate the shading values exceed the 90% confidence level.

After removing the effect of El Niño, the CTP heating is significantly linked with a northeastern Asian warming and corresponding upper-level anticyclonic circulation over northeastern Asia (Fig. 4.2b). The CTP precipitation is also related to an East Asia cooling band and corresponding cyclonic circulation (Fig. 4.2b), which may affect the East Asia rainfall variability.

For the ETP heating, the partial regression pattern (Fig. 4.2c) is similar to the linear regression: significant temperature anomalies appear upstream of the TP along the propagation path of the wave train excided by NAO (Fig. 3.5b). The circulation pattern, corresponding well with the temperature pattern, also suggests the linkage between the ETP heating and NAO, with two upper-level anticyclones over northwestern Asia and the southern ETP, and two cyclones over western Europe and the WTP. The downstream signal associated with the ETP heating is not evident. Although the NAO signal is statistically removed, the partial regression pattern associated with the ETP heating seems still to be dominated by the summer NAO-related wave disturbances. A numerical experiment is needed to inspect the effects of the ETP heating on upstream circulation and the causality between the ETP heating and the Eurasian teleconnection.

4.5. Direct Responses to the Western, Central, and Eastern TP Heating

The previous section revealed some possible linkages of the TP heating with global circulation. However, the regression results cannot prove causality. In this section, a simplified AGCM, the LBM (Watanabe and Kimoto, 2000), is utilized to test to what extent these linkages can be reproduced in numerical models. LBM is an anomaly model based on linearized primitive equations, in which the basic state is always chosen to be the climatological mean flow. Because of its lacking nonlinear interaction and gravitational instability, such simplified AGCM only comprise large-scale dynamical processes such as equatorial waves, Rossby wave propagation, baroclinic instability, and barotropic instability. This model has been widely proven to be a very useful tool to study the direct response of atmospheric circulation to large-scale external forcing.

In a pioneer work, Hoskins and Karoly (1981) used such a model and identified a “great circle” path of Rossby wave propagation given thermal and orographic forcing. After that, numerous studies attempted to study atmospheric direct response to various kinds of forcings. Baroclinic

instability inherited from primitive equations will eventually contaminate direct response to external forcing. Jin and Hoskins (1995) found that quasi-steady direct response to tropical forcing could only be seen during the first 20 days, after which baroclinic eddies would dominate. By comparing the linear and nonlinear baroclinic model runs, Ting and Yu (1998) suggested that direct response to tropical heating bears a striking similarity in the two models when additional damping is included in the linear model. Therefore, it is promising to study atmospheric response to external forcing with a linear model as long as carefully preventing baroclinic eddies from contaminating the direct response.

The basic state used in this model is the observed three-dimensional JJA climatology derived from ERA-Interim Reanalysis data. To simulate the ETP and CTP latent heating and the WTP sensible heating, three idealized local forcings are prescribed as follows (Fig. 4.3). ETP forcing is horizontally nearly-elliptical-shaped heating centered at southern ETP (97°E, 29°N), and its vertical profile is gamma shaped with a maximum heating rate of 2K/day at sigma level = 0.65 (about 450 hPa). Similar CTP forcing is centered at southern CTP (87°E, 29°N) with a maximum heating rate of 2K/day at sigma level = 0.65. WTP forcing is centered at (76°E, 35°N) with the maximum heating rate of 2K/day in boundary layer (below sigma level of 0.97); the heating rate decreases upward exponentially above the boundary layer. Note that the results show the pattern of response to the heating is not very sensitive to the horizontal shape of the heating forcing. Here the nearly-elliptical shape is used for idealized experiments.

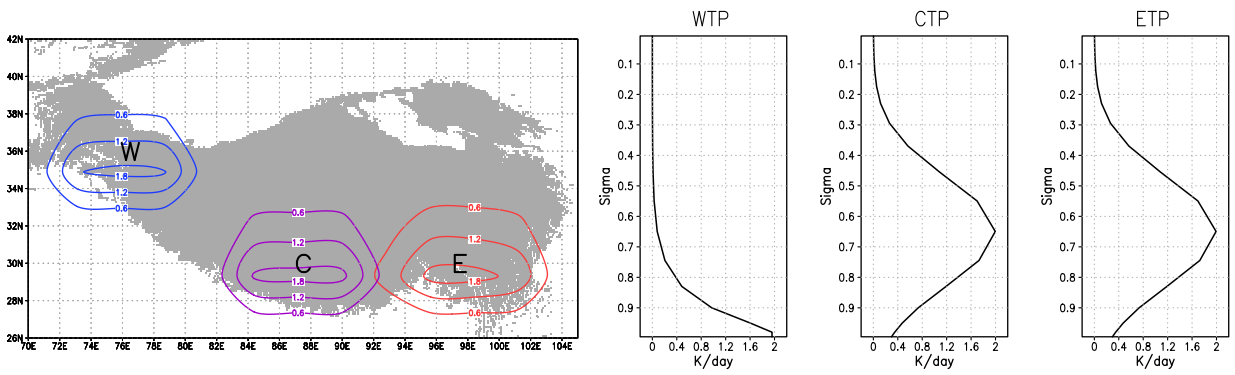

Fig. 4.3. Forcing fields for LBM experiments. [Left] Spatial patterns of (a) ETP, (b) CTP, and (c) WTP heating forcings. [Right] Vertical profiles of the ETP, CTP, and WTP heating, respectively.

Figure 4.4 shows the time evolution of 200 hPa stream function responded to the WTP (Fig. 4.4a), CTP (Fig. 4.4b), and ETP (Fig. 4.4c) forcing, respectively. In the first few days (Day 5), each forcing excites a corresponding upper-level anticyclonic circulation above the forcing area and a Rossby wave train propagating downstream zonally to East Asia. Note that the anticyclone center is located next to the southwest side of the CTP for the CTP forcing and located next to the southeast side of the ETP for the ETP forcing. Afterward, for both ETP and CTP forcing, the anticyclonic center is strengthened, and the wave train propagates further eastward; meanwhile, the wave energy extends westward to the upstream side (Day 10). Between two anticyclonic centers, a cyclone center develops over the central TP. Then the response pattern tends to be steady: the ETP response contains anticyclones and cyclones propagating to the northwest Pacific along the mid-latitude jet stream over Eurasia (Day 15–25); the CTP response has more eastward wave propagation to north central Pacific.

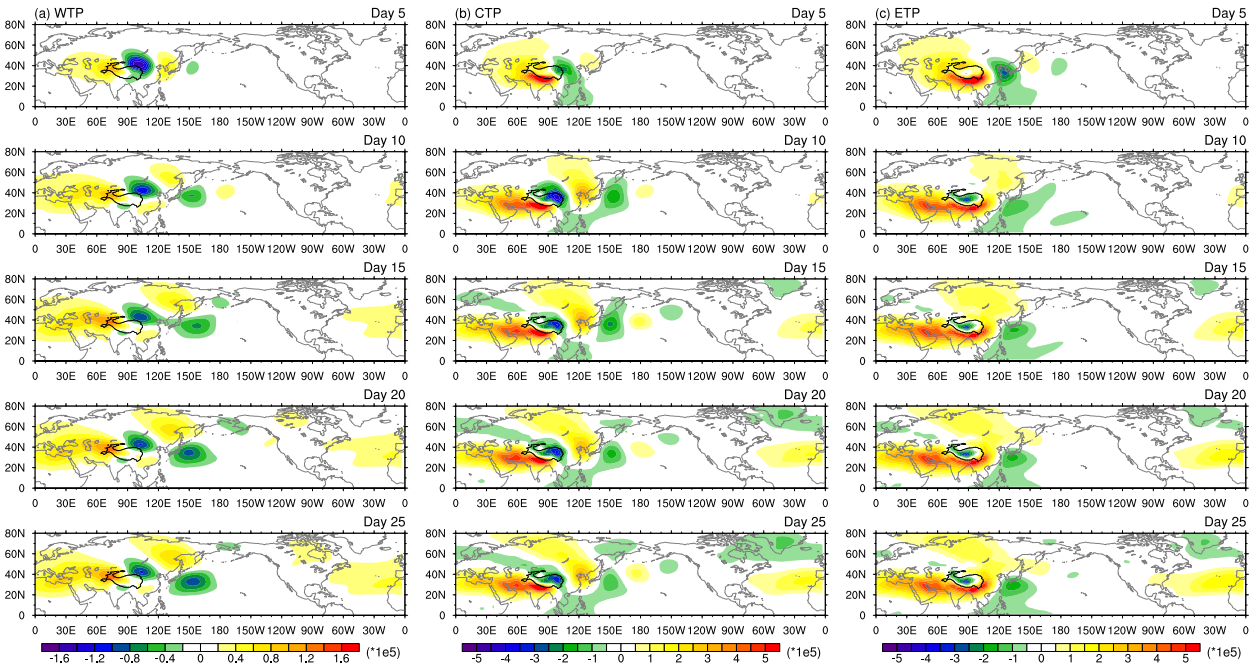

Fig. 4.4. LBM responses (Day 5 to Day 25) of the 200 hPa stream function ($m^2 s^{-1}$) to heating forcing of the (a) WTP, (b) CTP, and (c) ETP in JJA.

For the WTP forcing (Fig. 4.4a), besides the anticyclone center enhanced over the northwestern TP, the anticyclone over east Asia splits into two centers (a north-south pair) and the Rossby wave propagation begins to split into two branches since Day 10: the northern branch is approximately along a great circle path toward poleward and then equatorward as in the theoretical explanation by Hoskins and Karoly (1981); the southern branch takes a more zonal path in lower latitude along the westerly jet stream. Such split paths may be related to the exit region of the jet stream over Eurasia (Takaya and Nakamura 2001). From Day 10 to Day 20, the southern branch confines to coastal northwestern Pacific while the northern branch develops and propagates further eastward. The westward dispersion of the WTP anticyclone center is also strengthened and extends far westward. After Day 20, the response pattern maintains steady.

Since all of the responses gradually become steady from Day 15, we choose the mean response from Day 20 to 25 as the "steady response". The steady response patterns to different TP forcings are different (Fig. 4.5), as mentioned above. To better show how Rossby wave energy

propagates, the zonal mean flow (contours) and wave activity flux (**W**) and horizontal divergence of **W** ($\nabla_H \cdot \mathbf{W}$; Takaya and Nakamura, 2001) for the upper-level steady response to the TP forcings are also shown. In all three cases, the prescribed forcing excites a Rossby wave response due to westward phase propagation to its upstream and a stationary wave package response to its downstream. The easterly responses (around 20°N) in the south of directly-forced anticyclone over the TP match the observed feature shown in Fig. 4.2.

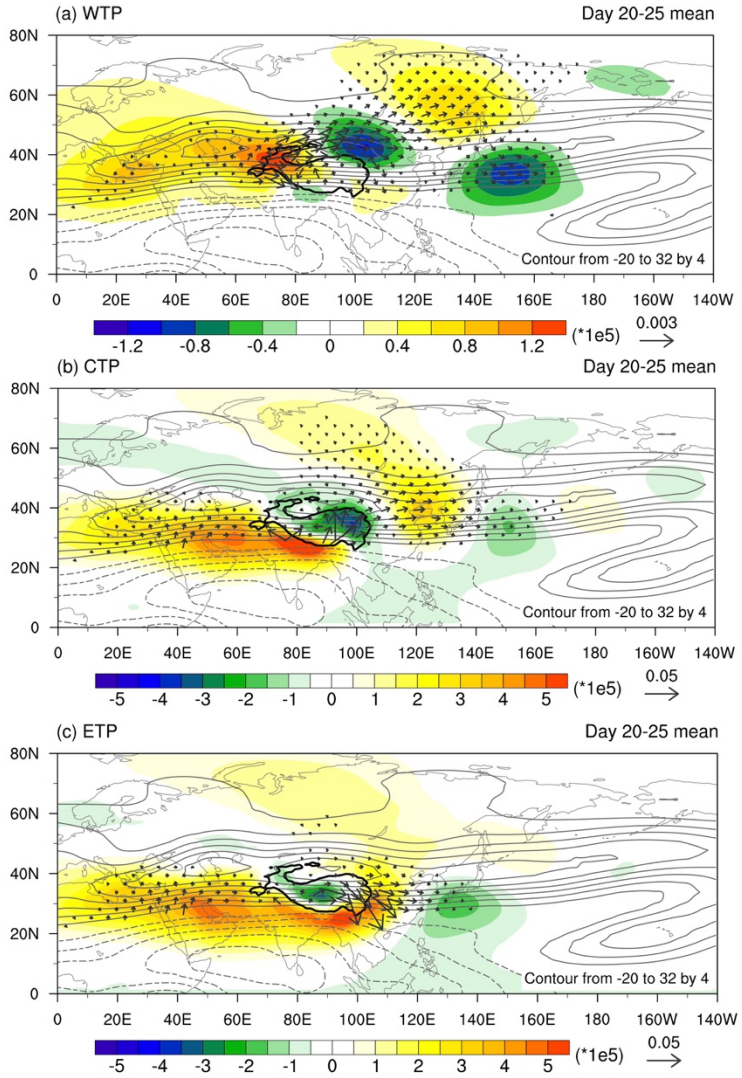

Fig. 4.5. Steady responses (Day 20–25 mean) of 200 hPa stream function (shading; unit: $m^2\ s^{-1}$) to heating forcing of the (a) WTP, (b) CTP, and (c) ETP. Vectors are wave activity fluxes (unit: $m^2\ s^{-2}$) that are drawn only where zonal mean flow > 2 m s^{-1}. Contours represents the zonal mean flow (unit: m s^{-1}).

The ETP response exhibits that the wave source region is located over the east side of the TP, and **W** shows evident wave activities transported from the anticyclone center over East China to the cyclone center over southern Japan (Fig. 4.5c). For the CTP response, the wave activities transport from the anticyclone center over the southwest slope of the TP to the cyclone center over the CTP and then to the anticyclone center over northeastern China and the cyclone over northwestern Pacific (Fig. 4.5b). For CTP and ETP forcing, as the heating locates toward the southern flank of the westerly, the response has relatively smaller scale, and the propagation is more zonal-like. The westerly jet plays as a wave guide for the response, and the wave train response cannot penetrate the westerly belt propagating to the north.

Regarding the WTP response, a wave source region is generated over the WTP and the wave activities transport from the WTP anticyclone center to the cyclone center to the northeast of the TP. Then the wave activities split into two directions (Fig. 4.5a): from the cyclone center to the anticyclone center over northeastern Asia and the anticyclone center over southeastern China. Both the northern and southern branches transport further eastward. The locations of the two split anticyclonic circulations roughly correspond with the locations of the observed WTP-heating related upper-level anticyclones and near-surface warming in polar Asia and southeastern China (Fig. 4.2a). Compared to the other two cases, WTP heating locates more northward and resides in a relatively stronger background westerly, which allows northward propagation of the wave train along the great circle.

4.6. Summary and Discussion

The different impacts of the interannual variations in the summer heat sources over the western, central, and eastern Tibetan Plateau (TP) are investigated using the newly developed heat source dataset and conducting model experiments.

The ETP, CTP, and WTP heat sources have different connections with climate and circulation. A northwestern-Asia warming center and a western-Europe cooling center are connected to the ETP heating (Fig. 4.2c), which correspond with the ETP-heating associated upper-level anticyclonic circulation over northwestern Asia and the cyclonic circulation over western Europe. The CTP heating is related to northeastern Asia warming and a cooling band in East Asia (Fig. 4.2b). The WTP heating is associated with warming in southeastern China and the polar region of Asia (Fig. 4.2a). The near-surface warming centers are roughly located under the TP-heating related upper-level anticyclonic circulations. The anomalous upper-level anticyclone may induce anomalous subsidence and reduce the cloud formation, increasing the net shortwave radiation and thereby warming the near-surface air.

Numerical experiments are conducted to examine the observational results. The direct circulation responses to the heating simulated by a linearized AGCM exhibit different upper-level wave-train patterns for different sub-regions' heating forcings (Fig. 4.5), suggesting their different impacts on teleconnection. For the ETP heating, an anticyclone is generated over the east side of the TP (East China), and the wave propagates eastward, forming a cyclone center over southern Japan. The CTP heating produces an anticyclone center over the southwest slope of the TP, a cyclone center over the CTP, and an anticyclone center over northeastern China. The WTP heating generates an anticyclone over the WTP and a cyclone center to the northeast of the TP. Then the wave train splits into two branches: the northern branch propagates to the anticyclone center over northeastern Asia and the southern branch propagates to the anticyclone center over southeastern China. Both the northern and southern branches transport further eastward. The locations of the two split anticyclonic circulations roughly correspond with the locations of the observed WTP-heating related upper-level anticyclones and near-surface warming in polar Asia and southeastern China (Fig. 4.2a).

The current study only uses a dry, linear model to conduct numerical experiments. It is found that for the WTP sensible heating, the model responses well match the observational results due to the fewer moisture processes involved in the teleconnection associated with the WTP heating. However, for the ETP and CTP latent heating that is closely related to moisture processes, this dry model cannot capture the basic features in the observations. Therefore, GCM experiments are needed to further investigate the impacts of the ETP and CTP latent heating.

We conducted a group of preliminary AGCM experiments using CAM4 model, prescribing anomalous WTP, CTP, or ETP heating. The heating patterns and profiles are the same as Fig. 4.3 shown. Each sensitivity experiment comprises 100 ensembles starting with different initial conditions. Results are displayed in Fig. 4.6. We can see that all the responses are stronger in mid-to-high latitudes, in which the patterns are quite different from the LBM and observed results. Therefore, more experiments and newer/high-resolution model are necessary for examining the impacts of the TP heating.

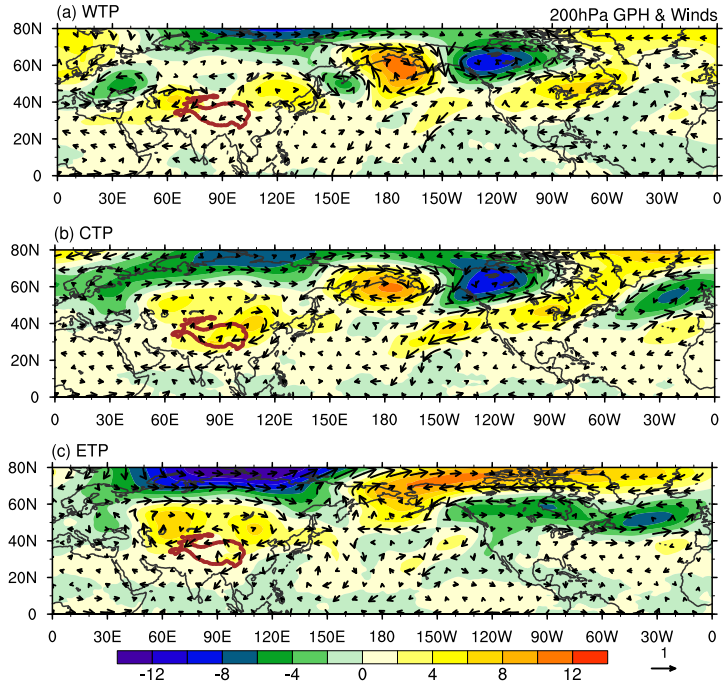

Fig. 4.6. CAM4 responses of 200 hPa geopotential height (shading; unit: m) and winds (vectors; m s^{-1}) to heating forcing of the (a) WTP, (b) CTP, and (c) ETP in JJA.

Chapter 5. Future Changes of Summer Heat Sources over the Tibetan Plateau in CMIP6 Models

5.1. Abstract

Model simulations and future changes of condensational latent heat released from precipitation and surface sensible heat (SH) over the eastern Tibetan Plateau (TP) are investigated with 22 CMIP6 models' outputs. The models reproduce the mean precipitation pattern well, but the mean intensity is 65% excessive. SH has scarcely been evaluated. It is found that nearly half of the models cannot realistically capture SH's spatial structure. The best six models in simulating SH are the same models that best simulate surface air temperature. The models with high performance are selected to make a multi-model ensemble mean projection. Under the medium emission scenario (SSP2-4.5), the TP's future summer precipitation will likely increase, despite its weakening thermal forcing effect. The increasing precipitation is primarily due to the future enhancement in vertical moisture transport and surface evaporation. However, the greenhouse gases (GHGs)-induced top-heavy heating stabilizes the atmosphere and diminishes the TP's thermal forcing effect, weakening the circulation and upward motion. As such, the precipitation sensitivity is only a 2.7% increase per degree Celsius global warming. The projected SH will be likely unchanged in accord with the likely unaltered surface wind speed. These results have important implications for the future change of the water supplies in the heavily populated South and East Asian countries. They could help the modeling groups further improve the climate model performance in the highland regions.

5.2. Introduction

Climate change, especially global warming, is a critical global issue. The TP has been identified as a region susceptible to climate change (Liu and Chen 2000). In recent decades, the TP has undergone a noticeable warming trend (Wang et al. 2008, Xu et al. 2008) even during the global warming hiatus period of 1998–2013 (Duan and Xiao 2015, You et al. 2016, Ma et al. 2017), which has already changed TP thermal forcing and regional environment significantly. Thus, it is imperative to investigate how the TP heat sources will change under future warming and understand why these changes will occur.

Atmosphere-ocean general circulation models (AOGCMs) and Earth system models (ESMs) are the primary tools for projecting future climate change. The Coupled Model Intercomparison Project (CMIP) makes plentiful standardized model outputs publicly available, considerably facilitating multimodel analyses of the past, current, and future climate. Multiple recent works found that most CMIP5 (phase 5 of CMIP) models have cold TP biases, and all of them overestimate precipitation in most parts of the TP (Su et al. 2013, Duan et al. 2013a, You et al. 2016, Salunke et al. 2018). With these caveats, the CMIP5 models generally projected rising TP surface air temperature and increasing precipitation under various Representative Concentration Pathway (RCP)-based scenarios (Su et al. 2013, Chen and Frauenfeld 2014a, b, Jia et al. 2019a, b). However, much less attention has been paid to the future change of the surface sensible heat (SH) over the TP (e.g., Wang et al. 2019). The TP summer sensible heating may ‘pump’ surrounding air upward, transporting abundant water vapor from the ocean to feed the highland Asian summer monsoon (Wu et al., 2007, 2012). Besides, most researches focus on how the TP precipitation will change, but few studies have explored the factors contributing to precipitation or SH changes.

The present work aims to assess the future changes of condensational latent heat (LH) and SH over the eastern TP as they are two different types of major summer heat sources over the TP (Xie and Wang 2019). LH is solely determined by precipitation, so we use precipitation as a proxy for LH. Precipitation also represents a critical component of the hydrological cycle and significantly influences the water resources over China and South Asian countries. We analyze 22 newest generation CMIP6 (phase 6 of CMIP) model products (Eyring et al. 2016) to (a) evaluate the models' capability and biases in reproducing the present-day climatological TP heat sources against the previous CMIP5 results, (b) select credible models to synthesize their ensemble projection of the TP heat sources' future changes, and (c) determine the causes of those future changes.

5.3. Data and Methods

5.3.1. CMIP6 model outputs

The monthly CMIP6 data used in this study are downloaded from the Earth System Grid Federation (ESGF) data replication centers (https://esgf-node.llnl.gov/projects/cmip6/). Table 5.1 lists the information of 22 models adopted in this study. The CMIP6 historical simulations (1850-2014) and the future projections under the SSP2-4.5 (SSP245) scenario (2015–2100) are utilized. The SSP245 scenario represents the medium-level emission pathway, and several other MIPs adopt it as a reference scenario (O'Neill et al. 2016). The last 20-year average of the SSP245 experiment (i.e., 2081–2100) will be compared with its historical counterpart (1995–2014) to quantify the future change, which minimizes the uncertainties arising from the models' internal variability (Wang et al. 2020).

Table 5.1. Description of the 22 CMIP6 models used in this study, including model names, countries, horizontal resolutions, and data references. All data are available online at https://esgf-node.llnl.gov/search/cmip6/.

Model Name	**Country**	**Institution**	**Resolution (Lat×Lon)**
ACCESS-CM2 ACCESS-ESM1-5	Australia	Australian Community Climate and Earth System Simulator (ACCESS)	144 × 192 145 × 192
BCC-CSM2-MR	China	Beijing Climate Center (BCC), China Meteorological Administration (CMA)	160 × 320
CanESM5	Canada	Canadian Centre for Climate Modelling and Analysis (CCCma)	64 × 128
CESM2 CESM2-WACCM	USA	National Center for Atmospheric Research (NCAR)	192 × 288
CNRM-CM6-1 CNRM-ESM2-1	France	Centre National de Recherches Meteorologiques–Centre Europeen de Recherche et Formation Avancees en Calcul Scientifique (CNRM-CERFACS)	128 × 256
EC-Earth3 EC-Earth3-Veg	Europe	European EC-Earth Consortium	256 × 512
FGOALS-g3	China	Chinese Academy of Sciences (CAS)	80 × 180
GFDL-CM4 GFDL-ESM4	USA	Geophysical Fluid Dynamics Laboratory (NOAA-GFDL)	180 × 288
HadGEM3-GC31-LL	UK	Met Office Hadley Centre (MOHC)	144 × 192
IPSL-CM6A-LR	France	Institute Pierre-Simon Laplace (IPSL)	143 × 144
MIROC6 MIROC-ES2L	Japan	Atmosphere and Ocean Research Institute (University of Tokyo), National Institute for Environmental Studies, and Japan Agency for Marine-Earth Science and Technology	128 × 256 64 × 128
MPI-ESM1-2-HR MPI-ESM1-2-LR	Germany	Max Planck Institute for Meteorology (MPI-M)	192 × 384 96 × 192
MRI-ESM2-0	Japan	Meteorological Research Institute (MRI)	160 × 320
NESM3	China	Nanjing University of Information Science and Technology (NUIST)	96 × 192
UKESM1-0-LL	UK	Natural Environment Research Council (NERC) and the Met Office Hadley Centre (MOHC)	144 × 192

We use the two-tailed Student's *t*-test to see whether the projected 2081–2100 means are significantly different from the historical 1995–2014 means. This test yields the probability measuring how the projected future multi-model ensemble mean (MME; $\bar{S}_M$ from Equation (5.1a))

differs from the simulated present-day MME ($\bar{H}_M$ from Equation (5.1b)). The variances used in the Student's *t*-test representing the intermodel spreads are calculated from Equations (5.1c) and (5.1d).

$$\bar{S}_M = \sum_{i=1}^{N} \bar{S}_i = \sum_{i=1}^{N} \left(\sum_{t=2081}^{2100} S_{t,i} \right), \tag{5.1a}$$

$$\bar{H}_M = \sum_{i=1}^{N} \bar{H}_i = \sum_{i=1}^{N} \left(\sum_{t=1995}^{2014} H_{t,i} \right), \tag{5.1b}$$

$$\mathrm{Var}(S) = \frac{\sum_{i=1}^{N} (\bar{S}_i - \bar{S}_M)^2}{N-1}, \tag{5.1c}$$

$$\mathrm{Var}(H) = \frac{\sum_{i=1}^{N} (\bar{H}_i - \bar{H}_M)^2}{N-1}, \tag{5.1d}$$

where $\bar{S}_i$ and $\bar{H}_i$ denote the 20-year averages of the SSP245 (S) and historical (H) simulations of each model, and N is the number of models.

5.3.2. Observational datasets

The monthly precipitation and surface (~2 m) air temperature data are obtained from the CN05.1 gridded observation dataset developed by Wu and Gao (2013). This dataset (1961–present) is based on more than 2400 meteorological stations in China and has been interpolated into a high resolution of 0.25° × 0.25°. The monthly SH flux data over the TP in 1984–2016 is provided by Xie and Wang (2019). This new estimate of SH is generated by merging several bias-corrected top-quality reanalysis datasets covering the entire TP region. These observational data are employed to evaluate the CMIP6 models' historical products, using several statistical methods such as model bias and pattern correlation coefficient. The boreal summer season (June–August, i.e., JJA) from 1979 to 2014 is chosen for the present-day analysis. The study domain is the TP region (TP; 26°–42°N, 70°–105°E) within a boundary defined by elevation higher than 2500 m.

Since most of the Chinese Meteorological Administration stations are located in the eastern part of the plateau, the following investigations of both CMIP6 simulations and observations are limited to the eastern TP (east of 90°E). To facilitate the model validation against observation, we interpolate all data's horizontal resolutions to 1° × 1°.

5.3.3. Precipitation attribution analysis

Condensational latent heat released from precipitation is calculated by $\mathrm{LH} = \mathrm{Pr} \times L_w \times \rho_w$, where Pr is the total precipitation (mm day^{-1}), L_w = 2.5×10^{-6} J kg^{-1} is the condensation heat coefficient, and ρ_w = 10^3 kg m^{-3} is the density of liquid water (Duan and Wu 2008). Since LH is solely proportional to precipitation, we apply precipitation to represent LH for subsequent analyses.

The precipitation attribution analysis (Jin et al. 2020) is adopted to examine the contributing factors to the future change of the eastern-TP precipitation. The expression of the moisture budget in a vertical column is:

$$P - E = -\langle \frac{\partial q}{\partial t} + \mathbf{V} \cdot \nabla q + \omega \frac{\partial q}{\partial p} \rangle , \tag{5.2}$$

where $\langle \quad \rangle = \frac{1}{g} \int_{p_s}^{p_T} (\quad)\, dp$ denotes the vertical integration. Here P and E are the precipitation rate and surface evaporation rate (kg m^{-2} s^{-1}), respectively. $\mathbf{V}$ is the horizontal wind velocity, ∇ is the horizontal gradient operator, q is the specific humidity, ω is the vertical p velocity, and p is the pressure. The tropopause pressure p_T is set to 100 hPa, and the surface pressure p_s is set to 600 hPa over the eastern TP. For monthly or seasonal mean motion, the local rate of change ($\frac{\partial q}{\partial t}$) can be neglected. A two-layer approximation is applied to the troposphere over the TP to estimate the moisture transport terms. Considering that the TP surface is around 600 hPa, we set the mid-level interface to 400 hPa and assume that the lower-layer mean specific humidity is equal to the specific humidity at 500 hPa, while the upper-layer specific humidity is negligible. Thus, the horizontal

and vertical moisture transports can be approximated by

$$-\langle \mathbf{V} \cdot \nabla q \rangle \approx -\frac{1}{g}\left(u_{500}\frac{\partial q_{500}}{\partial x} + v_{500}\frac{\partial q_{500}}{\partial y}\right)\Delta p, \tag{5.3a}$$

$$-\langle \omega \frac{\partial q}{\partial p} \rangle \approx -\frac{1}{g}\omega_{400} q_{500}, \tag{5.3b}$$

where Δp = 200 hPa is the thickness of the lower layer. Therefore, the precipitation change could be attributed to the changes in surface evaporation, low-level horizontal moisture advection, and vertical moisture transport, as expressed by the following Equation:

$$\Delta \mathrm{Pr}^{*} = \Delta \mathrm{Ev} + \underbrace{\Delta\left(-\frac{\Delta p}{\rho_w g}\mathbf{V_{500}} \cdot \nabla q_{500}\right)}_{\Delta[-\mathbf{V}\cdot\nabla q]} + \underbrace{\Delta\left(-\frac{1}{\rho_w g}\omega_{400} q_{500}\right)}_{\Delta[-\omega q]}, \tag{5.4}$$

where $\mathrm{Pr} = P/\rho_w$ and $\mathrm{Ev} = E/\rho_w$ (mm day^{-1}). The operator Δ represents the difference between the SSP245 projection (2081–2100 mean) and the historical simulation (1995–2014 mean). $\Delta \mathrm{Pr}^{*}$ denotes the diagnosed precipitation change that is the sum of the three terms on the right-hand side of Equation (5.4).

5.3.4. Other statistical measures

Several objective approaches are utilized to quantify the fidelity of the CIMP6 historical simulations: model bias (the difference between simulation and observation); relative bias defined as bias/observation×100% (Su et al. 2013); model spread (the standard deviation of multiple models' simulations); pattern correlation coefficient (PCC) that measures the similarity between the modeled and observed climatology patterns; and domain-averaged normalized root-mean-square error (NRMSE) of simulated climatology (Li et al. 2018). The root-mean-square error (RMSE) is computed by

$$\mathrm{RMSE} = \sqrt{\frac{1}{N}\sum_{i=1}^{N}(S_i - O_i)^2}, \tag{5.5}$$

where S_i and O_i denote simulation and observation at each grid point, and N is the number of all grid points in the eastern TP. The NRMSE is the RMSE normalized by the observed spatial standard deviation:

$$\mathrm{NRMSE} = \frac{\mathrm{RSME}}{\sqrt{\frac{1}{N-1}\sum_{i=1}^{N}(O_i - \bar{O})^2}}, \tag{5.6}$$

where $\bar{O}$ is the spatial mean value of the observation.

5.4. Evaluations of the Modeled Present-day Summer Precipitation and Sensible Heat Flux

Figure 5.1(a) shows that the observed JJA mean precipitation generally decreases from the southeast to the northwest over the TP because the South Asian monsoon transports abundant water vapor primarily to the southeastern TP. The regional-mean rainfall for the eastern TP is 3.3 mm day^{-1} or 302 mm during JJA. The historical precipitation simulated by the multi-model ensemble mean (MME) is higher than the observation in most parts of the TP region (Fig. 5.1b). The largest bias and intermodel spread (measured by one standard deviation of multiple models' simulations) appear at the southern and eastern edges, indicating the models' poor skills in simulating the monsoon rainfall amount over the southeastern TP. All models overestimate the observed precipitation with the relative biases ranging from 7.6% to 112.6% over the eastern TP. Thus, the 22 models' MME has a notable wet bias of 2.1 mm day^{-1} or 64.8% of the mean plus a great intermodel spread of 1.6 mm day^{-1}. To quantify the discrepancy among models, we further calculate the PCC and NRMSE of each model compared with observation (Fig. 5.1c). Since the wet biases are substantial, both PCC and NRMSE need to be considered for choosing high-performance models. The best eight models with high PCC (greater than the mean) and low NRMSE (smaller than the mean) are selected (upper left quadrant in Fig. 5.1c). The MME of the best eight models ('Best 8 MME') is better than the MME of all 22 models ('22 MME') in

capturing the observed pattern. The corresponding five poor models—PCC (NRMSE) lower (higher) than the mean value—are also picked out as a contrast group. The mean bias of the best group is 59.1%, which is significantly smaller than that of the poor group (89.6%). In addition, both observation and MME historical simulations exhibit no significant trend in the TP summer precipitation (figure not shown).

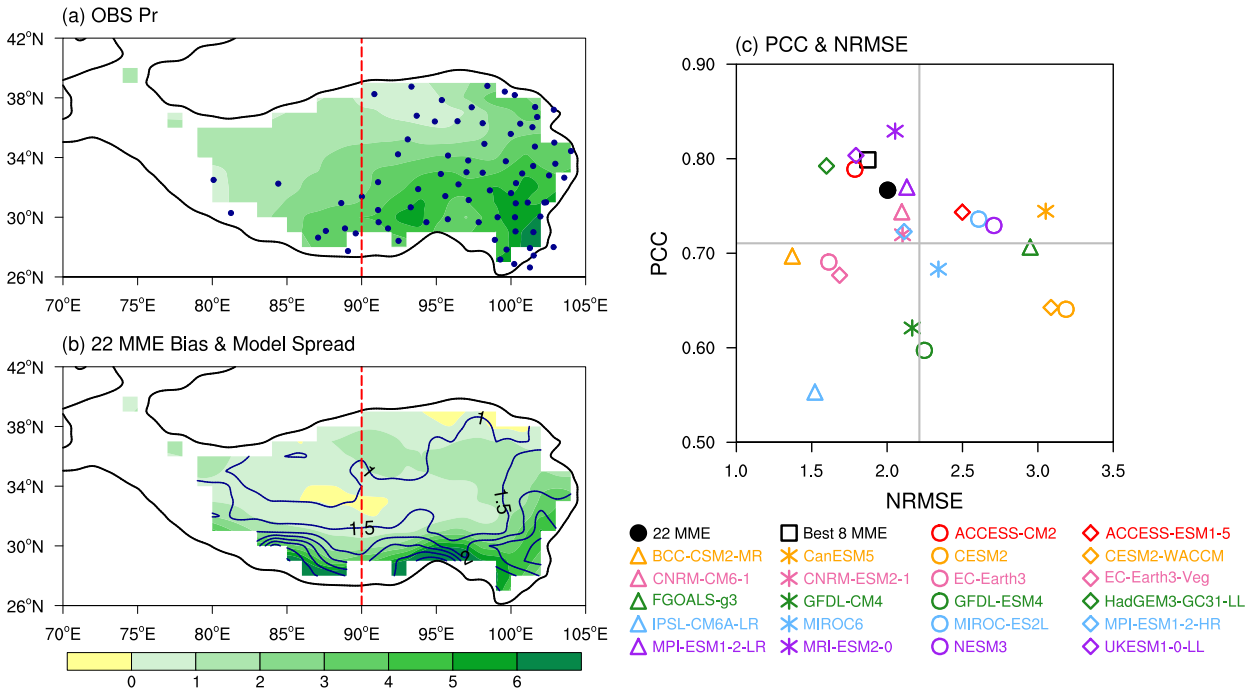

Fig. 5.1. (a) Observed 1979–2014 JJA climatology of precipitation (Pr; units: mm day^{-1}) over the TP from the CN05.1 dataset. (b) Patterns of MME's bias (shading) and intermodel spread (contours) for precipitation. The black curve in (a) and (b) outlines the TP region with elevation above 2500 m. The dots in (a) denote the Chinese Meteorological Administration stations. (c) Performance of the 22 CMIP6 models and their MME (solid black dot) on simulating the observed precipitation pattern over the eastern TP (east of 90°E). The vertical and horizontal coordinates in (c) are PCC and NRMSE, respectively. The horizontal (vertical) gray line in (c) indicates the mean value of the PCC (NRMSE) of 22 models. The hollow black square in (c) depicts the MME of the selected best eight models enclosed in the upper left quadrant. The five poor models are enclosed in the lower right quadrant.

To see if there is an improvement compared to CMIP5, we refer to Su et al. (2013)'s results that examined the annual mean precipitation over the eastern TP in 24 CMIP5 models. They found an overestimation range of 61.9% to 183.4%, with a mean bias of 116.6% in CMIP5 models.

Through our calculations, the CMIP6 simulated annual mean precipitation has a mean bias of 99.0%, with a range from 44.3% to 142.8%. We find that the CMIP6 models' mean wet bias in annual mean precipitation is reduced by 18%, and the intermodel spread range is reduced by 23% compared to CMIP5. The improvement is statistically significant at the 90% confidence level. Considering that a fair comparison requires the same group of models or at least the same number of models, the comparison of ours and Su et al. (2013) results is not ideal but arguably reasonable.

The period 1984–2014 is selected for the evaluation of SH owing to the limited availability of reliable observational data. The observed summer SH is stronger in the western-central and northern TP (Fig. 5.2a) due to sparse vegetation, semiarid surface condition, and higher altitude. The mean SH in the eastern TP is 48.4 W m^{-2}. The distributions of the 22 MME's bias and the intermodel spread (Fig. 5.2b) generally resemble that of the SH climatology (Fig. 5.2a) with larger negative bias over the western and northern TP. The MME has a bias of -6.1 W m^{-2} or -12.7% over the eastern TP, and the area-averaged intermodel spread is 14.7 W m^{-2}. The relative biases of all models range from -61.8% to 35.7%, in which most of them (15 out of 22) underestimate the SH. Twelve out of 22 models with PCC above 0.75 suggest their good spatial correspondence with the observation, while other models have PCC lower than 0.62 (Fig. 5.2c). Since the model biases are relatively small, we use PCC as the primary criterion to select 12 models as a good-model group, and the other ten models form a poor-model group. It can be seen that the good models for SH do not precisely match those for the precipitation, indicating the model's inconsistent skills in simulating different variables. For SH, the 'Good 12 MME' has the optimal performance with the highest PCC (0.90) and almost the lowest NRMSE (0.57). Considering the uncertainties in the SH datasets (Duan et al. 2014), we also compared the model simulations with two other advanced TP SH observational datasets provided, respectively, by Yang et al. (2011) for the period 1984–2006 and Duan et al. (2018) for the period 1979–2016 to verify the reliability of the above result. It turns

out that the same twelve good models are selected (Fig. 5.3). Moreover, the MME historical simulations can capture the weakening trend in the observed SH (figure not shown), which is mainly due to the reduced surface wind speed over the eastern TP (Duan et al. 2008), despite that the declining rate of the modeled SH is lower than the observed value.

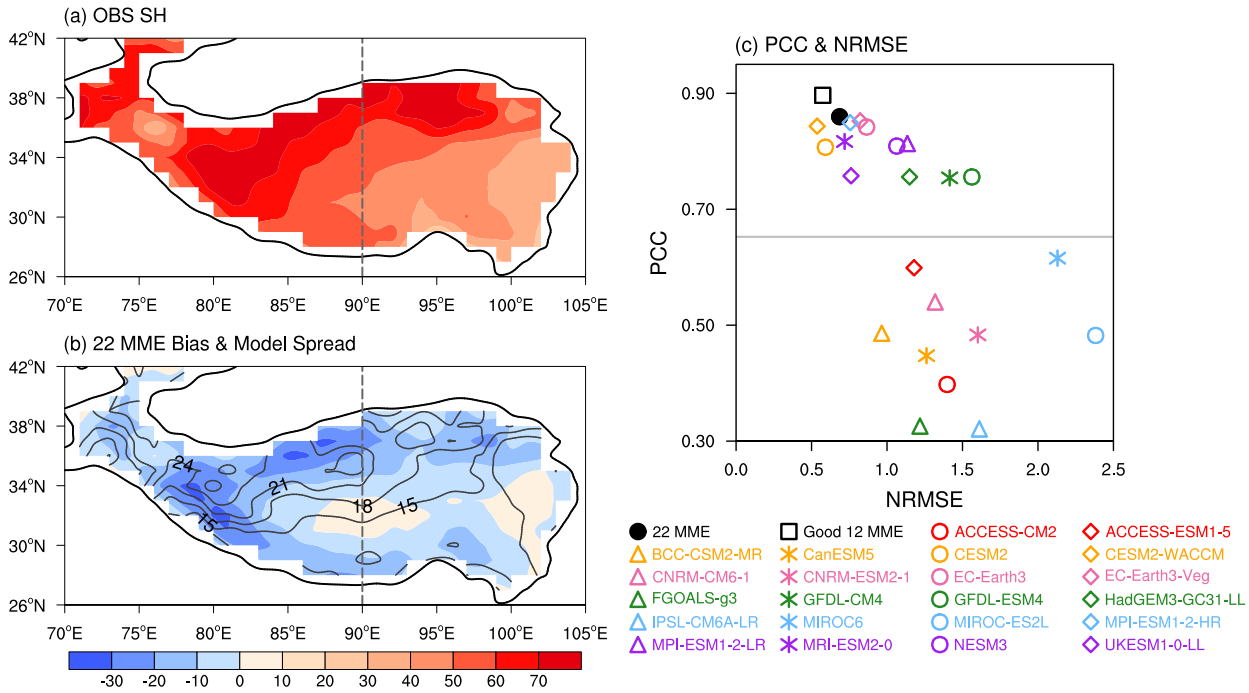

Fig. 5.2. Same as Fig. 5.1 but for surface sensible heat (SH; units: W m^{-2}) in 1984–2014. The horizontal gray line in (c) indicates the mean value of the PCC of 22 models. The hollow black square in (c) depicts the MME of the selected twelve good models (above the gray line).

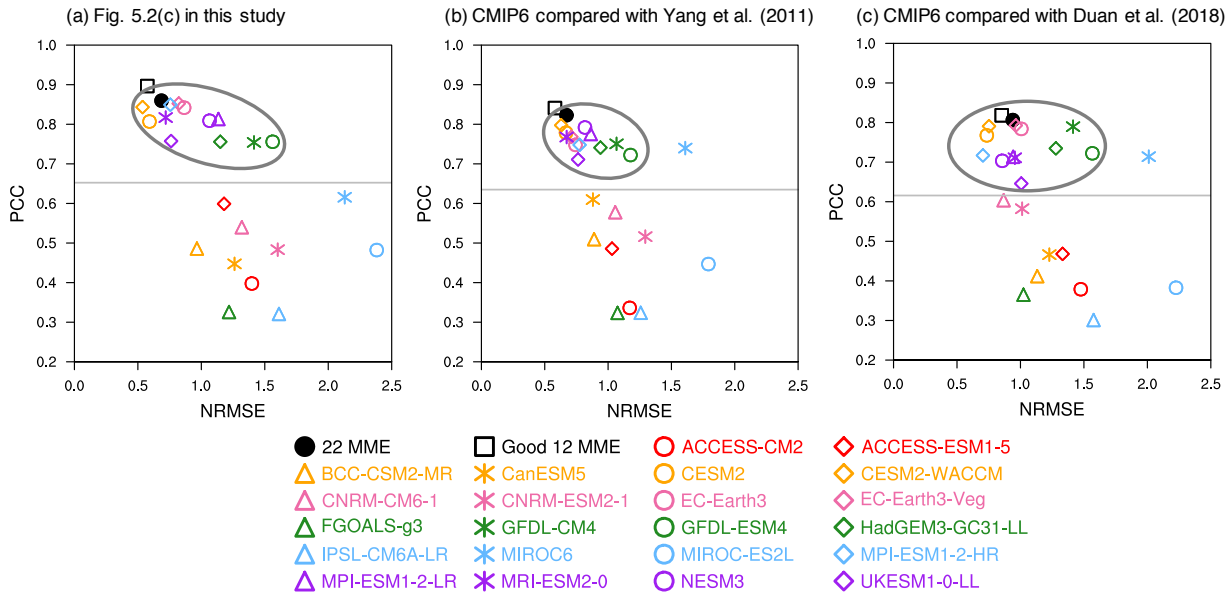

Fig. 5.3. Performance of the 22 CMIP6 models and their MME (solid black dot) on simulating the observed SH pattern over the eastern TP. The reference observational data are provided by (a) Xie and Wang (2019), (b) Yang et al. (2011), and (c) Duan et al. (2018), respectively. The vertical and horizontal coordinates are PCC and NRMSE. The horizontal gray line indicates the mean value of the PCC of 22 models. The hollow black square depicts the MME of the selected twelve good models enclosed in the gray oval.

5.5. Future Projections of the TP Summer Heat Sources

5.5.1. Projected changes of the TP precipitation and sensible heat and their influencing factors

We use the difference between the 2081–2100 average in the SSP245 experiment and the 1995–2014 average in historical simulation to quantify the projected change in the 21st century and utilize the percentage of this difference to the 1995–2014 climatology to represent the expected relative change. The precipitation attribution analysis shows that the enhancement of vertical moisture transport and surface evaporation are the major contributors to the simulated precipitation increase. In contrast, the horizontal moisture advection term is relatively small and has a negative contribution (Fig. 5.4). This conclusion is valid for all models in general. However, the relative

contributions between the vertical transport and evaporation differ among the three MME groups. In 'Best 8 MME,' the increase in evaporation is much larger than the increase in vertical moisture transport, while in 'Poor 5 MME,' the substantial vertical moisture transport enhancement is the primary contributor to the precipitation increase. Thus, the contributions of these two terms are comparable in '22 MME.' Compared to '22 MME' and 'Poor 5 MME,' the 'Best 8 MME' diagnosed precipitation change (ΔPr^*) seems to a bit overestimate the projected change (ΔPr). The reason for this overestimation needs further investigation.

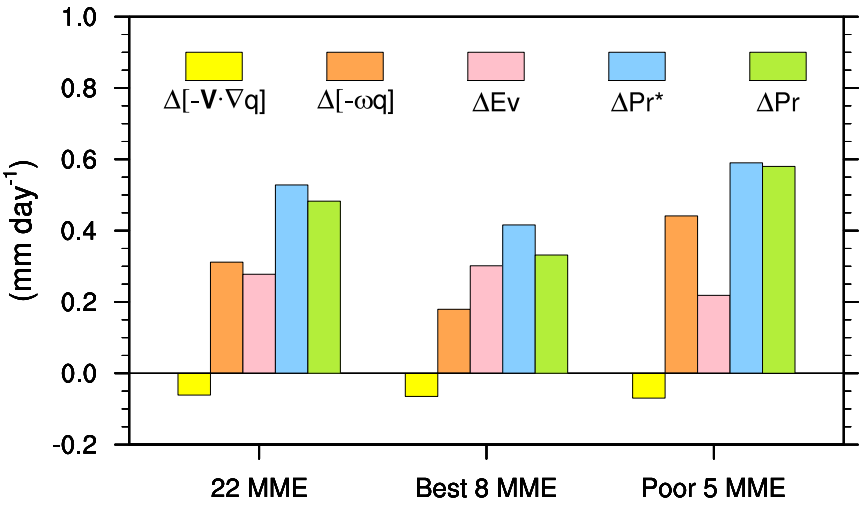

Fig. 5.4. Moisture budget decomposition of the summer precipitation change (the difference between 2081–2100 mean and 1995–2014 mean) over the eastern TP for three groups: '22 MME,' 'Best 8 MME,' and 'Poor 5 MME.' The yellow, orange, pink, blue, and green bars denote the horizontal moisture advection change ($\Delta[-\mathbf{V}\cdot\nabla q]$), vertical moisture transport change ($\Delta[-\omega q]$), surface evaporation change (ΔEv), diagnosed precipitation change (ΔPr^*), and multi-model simulated precipitation change (ΔPr), respectively.

Table 5.2 presents the projected changes of precipitation and their attributing terms over the eastern TP. The significance of these future changes has been examined using the two-tailed Student's *t*-test in which the intermodel spread (i.e., model uncertainty) is considered. The confidence level follows the likelihood scale assigned by the IPCC fifth assessment report on consistent treatment of uncertainties (Mastrandrea et al. 2010). Precipitation projected by 'Best 8

MME' will 'likely' increase by 6.2% (0.33 mm day^{-1}), which is attributed to a 'very likely' enhancement of 12.1% in surface evaporation, a 'likely' intensification of 9.0% in vertical moisture transport, and a slight offset by the 'likely' decrease in horizontal moisture convergence. The 'virtually certain' increase of 21.4% in low-level specific humidity and the 'likely' weakening of 8.9% in ascending motion jointly induce the predicted strengthening in the vertical moisture transport. The relative change of the horizontal moisture advection term is quite large (40.5%) since this term's historical average (negative) is very small. The results of '22 MME' are similar to those of 'Best 8 MME,' except that the '22 MME' projected precipitation will 'very likely' increase owing to the less offset effect by the 'about as likely as not' decrease in the upward motion.

Table 5.2. 'Best 8 MME' and '22 MME' projected precipitation changes and their contributing factors over the eastern TP in summer. Results of '22 MME' are presented as a comparison. The *, **, and *** symbols indicate that the likelihood of the projected change is 'likely' (66–100% probability), 'very likely' (90–100% probability), and 'virtually certain' (99–100% probability), respectively (under two-tailed Student's *t*-test). The value without the asterisks means its likelihood is 'about as likely as not' (33–66% probability). Note that $-\omega_{400}$ is presented in the table because the summer-mean value of ω_{400} is negative over the eastern TP, which indicates the climatological ascending motion.

	Pr		Ev		$[-\boldsymbol{V}\cdot\nabla q]$	
	Change (mm day^{-1})	Relative Change	Change (mm day^{-1})	Relative Change	Change (mm day^{-1})	Relative Change
'Best 8 MME'	0.33*	6.2%*	0.30**	12.1%**	-0.065*	40.5%*
'22 MME'	0.48**	8.7%**	0.28**	10.9%**	-0.061*	46.0%*
	$[-\omega q]$		q_{500}		$-\omega_{400}$	
	Change (mm day^{-1})	Relative Change	Change (g kg^{-1})	Relative Change	Change (Pa s^{-1})	Relative Change
'Best 8 MME'	0.18*	9.0%*	0.91***	21.4%***	-4.14×10^{-3}*	-8.9%*
'22 MME'	0.31*	14.7%*	0.91***	20.8%***	-2.19×10^{-3}	-4.4%

According to the bulk aerodynamic formula of surface sensible heat flux, SH is proportional to the surface (~10 m) wind speed (U_s) and the ground-air temperature difference ($T_s - T_{as}$). The SH projected by 'Good 12 MME' will be 'likely' unchanged (i.e., 'unlikely' changed) in the future (Table 5.3). Meanwhile, the surface wind speed will also 'likely' remain unchanged, and the ground-air temperature difference will 'about as likely as not' (i.e., insignificantly) decrease. The '22 MME' predicted SH will be 'very likely' unchanged (i.e., 'very unlikely' changed).

Table 5.3. 'Good 12 MME' and '22 MME' projected SH changes and their influencing factors over the eastern TP in summer. The $^{++}$ and $^{+}$ symbols indicate 'very unlikely' (0–10% probability) and 'unlikely' (0–33% probability), respectively (under two-tailed Student's *t*-test). The value without the symbols means its likelihood is 'about as likely as not' (33–66% probability).

	SH		U_s		$T_s - T_{as}$	
	Change (W m^{-2})	Relative Change	Change (m s^{-1})	Relative Change	Change (°C)	Relative Change
'Good 12 MME'	1.40^{+}	3.3%$^{+}$	-0.10^{+}	-3.8%$^{+}$	-0.25	-15.0%
'22 MME'	0.21^{++}	0.5%$^{++}$	-0.09^{+}	-3.0%$^{+}$	-0.16	-8.8%

Figure 5.5 shows the range of the projected relative changes, illustrating the large inter-model variability in 22 models. The box includes 66% of data that shows the range of 'likely' occurrence, and the dashed line between the 5th and 95th percentiles represents the 'very likely' range. Most models project enhancement in precipitation. Six of the best eight models are concentrated in the 'likely' box, and the '22 MME' projection is higher than the 'Best 8 MME.' Since the MPI-ESM1-2-HR and MPI-ESM1-2-LR models predict negative changes, the projection range of the 'Best 8' group is quite large. The projected changes of SH show great discrepancies among the models, and the 'likely' box is inclusive of zero, which induces the insignificant MME change. The spread of the good models for SH is also broad, mainly due to the two notable positive outliers (CESM2 and CESM2-WACCM models).

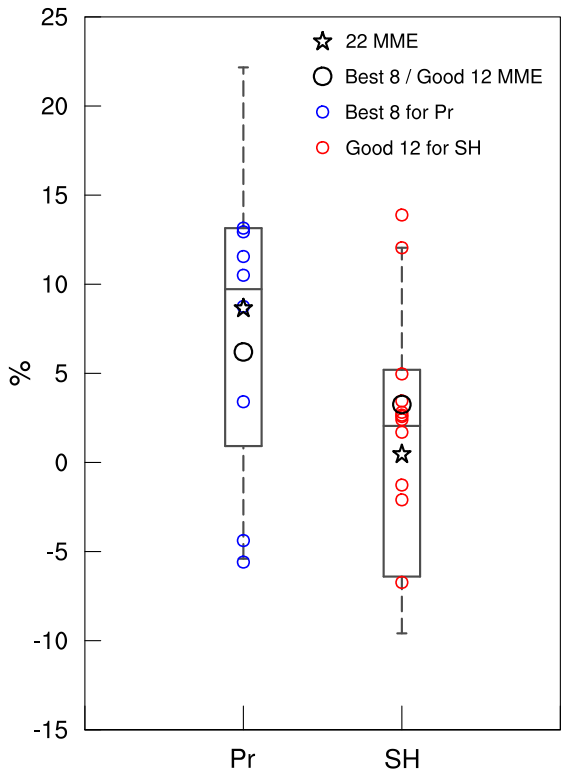

Fig. 5.5. Range of the projected relative changes of precipitation (Pr; mm day^{-1}) and SH (W m^{-2}): 2081–2100 average minus 1995–2014 average. The boxplots indicate the 5th and 95th percentiles (whiskers), 17th and 83rd percentiles (box ends), and median (black solid middle bar). The black hollow star is the MME of all 22 models, and the black circle denotes the MME of the best eight (twelve good) models for Pr (SH). The small blue (red) circles represent the individual projections by the best eight (twelve good) models for Pr (SH).

5.5.2 Precipitation sensitivity to local and global warming

To obtain the precipitation sensitivity (the relative change scaled to one degree of local or global warming), we evaluate the simulated surface air temperature (T_{as}). The '22 MME' has a cold bias of 0.31 °C that is -3.5% relative to the observation over the eastern TP. This bias is slightly less than the cold bias found in the CMIP5 models (< 1 °C in summer) (Su et al. 2013). All models have PCC higher than 0.6 in simulating observed T_{as}. The best six models for T_{as} are the same as those for SH, suggesting that the models better simulating the surface air temperature are more likely to simulate the SH better over the TP. The best models for precipitation are different

from those for T_{as}, but the 'Pr Best 8 MME' still has good performance in reproducing the climatological T_{as} (PCC = 0.81). Therefore, considering the consistency with the precipitation, we use the 'Pr Best 8 MME' to analyze the future change of T_{as}. All 22 models predict a steadily warming trend under SSP245, and the projected 20-year change from 'Pr Best 8 MME' is 3.0 °C that is virtually certain warming over the eastern TP. Given the relative change of precipitation is 6.2%, the precipitation sensitivity to local warming is 2.1% $°C^{-1}$. The global surface air temperature is projected to rise by 2.3 °C from 'Pr Best 8 MME.' Thus, the precipitation sensitivity to global warming is 2.7% $°C^{-1}$.

As the TP will warm up in the future, the surface evaporation and low-level specific humidity are projected to increase significantly according to the Clausius-Clapeyron relationship (Held and Soden 2006). We have checked that the soil moisture is projected to be very unlikely changed over the eastern TP, but the leaf area index will likely increase. The vegetation greening will probably help enhance the land-surface evapotranspiration. Moreover, to investigate what causes the likely weakening of ascending motion in 'Best 8 MME,' we examine the future changes of the 500 hPa divergence ($\nabla \cdot \boldsymbol{V}_{500}$) at the top of the eastern TP boundary layer and the atmospheric static stability measured by the difference between 200 hPa and 500 hPa pseudoequivalent potential temperature ($\Delta\theta_{se}$; Bolton 1980) (Table 5.4). The 'Best 8 MME' predicts an 'about as likely as not' increase in 500 hPa divergence. Besides, the projected 500 hPa air temperature difference (ΔT_{500}) between the eastern TP and East Asia (EA: 25°–40°N, 105°–130°E) is 'about as likely as not' to decrease. The changes of both $\nabla \cdot \boldsymbol{V}_{500}$ and ΔT_{500} imply an insignificant reduction of the TP low-level cyclonic circulation. The static stability is projected to 'very likely' increase by about 10% due to the greenhouse gases (GHGs)-induced top-heavy heating (i.e., the upper-level air will warm faster than the low-level air). Thus, the atmospheric stabilization is the main cause for the likely weakening of the TP upward motion.

Table 5.4. 'Best 8 MME' projected changes of $\nabla \cdot V_{500}$, ΔT_{500}, and $\Delta\theta_{se}$ over the eastern TP in summer. The ** symbol indicates 'very likely' (90–100% probability) change (under two-tailed Student's t-test). The values without the asterisks denote their likelihood are 'about as likely as not' (33–66% probability).

	$\nabla \cdot \boldsymbol{V}_{500}$		ΔT_{500}: TP–EA		$\Delta\theta_{se}$: 200 hPa – 500 hPa	
	Change (s^{-1})	Relative Change	Change (°C)	Relative Change	Change (K)	Relative Change
'Best 8 MME'	1.24×10^{-7}	33.4%	-0.08	-5.3%	2.63**	10.1%**

5.6 Conclusions and Discussion

Most CMIP6 models can reasonably simulate the observed climatological patterns of precipitation and temperature over the eastern TP. However, the SH pattern still could not be well captured by nearly half of the models. It is worth noting that the best six models for SH are the same as those for surface air temperature. The mean cold bias in CMIP6 (0.31 °C) is slightly reduced compared to Su et al. (2013) assessed CMIP5's cold bias (< 1 °C). The models have large wet biases with a mean of 2.1 mm day^{-1} or 65%. Compared to the CMIP5 simulations (Su et al. 2013), we find that the mean wet bias in the CMIP6 simulated annual mean precipitation is reduced by 18%, with a reduction of 23% in the intermodel spread range. However, the systematic wet biases remain relatively large in CMIP6 models, suggesting that the simulation of precipitation remains a major challenge. We attempted to ascribe the bias to the models' limited capability in dealing with topographic effects. Current climate models cannot fully capture many regional processes such as local circulation induced by complex topography due to their coarse resolution (Giorgi and Marinucci 1996, Su et al. 2013). Meanwhile, model performance is sensitive to parameterization schemes for sub-grid convective processes (Kang and Hong 2008, Chen et al. 2010, Neelin et al. 2010). Deficient cumulus parametrization could induce biases in simulations.

Most models project a prominent warming and wetting trend in the 21st century under the SSP245 scenario. The 'Pr Best 8 MME' projects a 3.0°C increase in local temperature and a 6.2% increase in precipitation compared to 1979–2014 mean. The precipitation sensitivity to local temperature rise is 2.1% $°C^{-1}$, and to global warming is 2.7% $°C^{-1}$. The likely increase in precipitation is primarily attributed to the likely increasing vertical moisture transport and the very likely intensifying surface evaporation. The vertical moisture transport depends on the changes of low-level moisture and mid-level upward motion. Anthropogenic warming certainly enhances low-level humidity. The increasing water vapor likely comes from the future enhancement of evaporation or evapotranspiration from the land surface, including the lake, vegetation, soil, river, and glacier. A surface water budget analysis is needed to fully address the sources of the water vapor. On the other hand, the GHGs-induced top-heavy heating stabilizes the atmosphere and thus likely weakens the upward motion. The weakening of the ascending motion partially offsets the increases in surface humidity and evaporation, thereby reducing the precipitation sensitivity to global warming.

For SH, 'Good 12 MME' predicts an 'unlikely' change due to the large intermodel spread. Along with it, the near-surface wind speed will also be likely unchanged, although the ground-air temperature is projected to 'about as likely as not' decrease. By comparing the historical simulations of U_s and $T_s - T_{as}$ with the corresponding observations, we find that the CMIP6 models can capture the decreasing trend of observed U_s but not the increasing trend of $T_s - T_{as}$ (Fig. 5.6). Oppositely, the 'Good 12 MME' even simulates a decreasing trend of $T_s - T_{as}$ during 1979–2014. Thus, the projected decrease in $T_s - T_{as}$ may not be reliable. Further investigation is needed to understand the models' poor performance in simulating $T_s - T_{as}$. Since the CMIP6 models show high performance for T_{as}, the problem might come from the simulation of T_s, which is related to complex land processes in the plateau region.

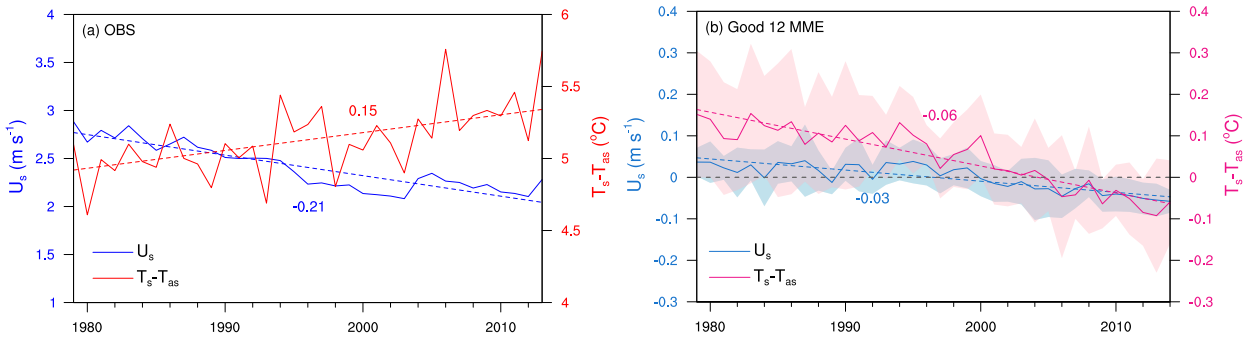

Fig. 5.6. Time evolutions of the eastern-TP-averaged JJA surface wind speed (U_s; units: m s^{-1}) and ground-air temperature difference ($T_s - T_{as}$; units: °C) in (a) observation and (b) historical simulation by 'Good 12 MME'. The 1979–2014 climatological means have been removed in (b). The dashed lines indicate the linear trends of each curve, and the numbers near the lines denote the corresponding linear trends per decade. The shading area in (b) displays the MME's uncertainty represented by intermodel spread, i.e., one standard deviation.

The CMIP6 models' biases over the TP are probably associated with the coarse model resolution and defective physical parameterization. The current models cannot fully capture many local processes induced by complex topography. In this study, the EC-Earth3 and EC-Earth3-Veg models have the highest spatial resolution (256 × 512). These two models are the best in simulating the observed temperature pattern and are superior in reproducing SH. For the precipitation, these two European models also have almost the least wet biases. Besides, by comparing the models from the same institution, the wet bias of the high-resolution model (MPI-ESM1-2-HR or MIROC6) is smaller than that of the low-resolution model (MPI-ESM1-2-LR or MIROC-ES2L). The above results suggest that refining spatial resolution could help to reduce model biases in the TP region. The apparent wet bias is also related to the deficiencies in model cumulus parameterizations, one of the major sources of uncertainty in precipitation projection and needs to be further explored. This study may help the modeling groups further improve the climate model performance in highland regions.

Citation: Xie, Z., and B. Wang, 2021. Summer Heat Sources Changes over the Tibetan Plateau in CMIP6. *J. Environ. Res. Lett*, **16**, 064060, https://doi.org/10.1088/1748-9326/ac0279.

Chapter 6. Concluding Remarks

6.1. Key Findings

In the first part of this dissertation, a new and reliable estimate of the summer heat sources over the entire Tibetan Plateau (TP) has been developed by synthetically using several bias-corrected reanalysis datasets, gauge-based observations, and selected satellite data. The climatology, long-term trends and interannual variations of summer total heat and its three components over various sub-regions of the TP have been comprehensively examined. Different from most previous research that focused on the station-covered eastern TP (east of 85°E), this study pays more attention to the data-sparse western plateau (70° - 85°E). A noteworthy new finding in summer climatology is a minimum of the total heat area over the northwestern TP (around 76°E, 36°N). The radiative cooling there is strong due to the insulation effect of debris-covered Karakoram glaciers on solar radiation, while SH and LH there are relatively small, thus leading to a negative value of the total heat. The latent heat (LH) plays the most important role for the total heat over the central-eastern TP in July-August, while the surface sensible heat (SH) is stronger in June and over the central-western TP; radiative cooling is largest in August. The total heat shows insignificant trends over the eastern and central TP from 1984 to 2006, whereas it exhibits an evident increasing trend over the western TP. The year-to-year variation of the total heat over the central-eastern TP is highly correlated with LH. The TH of WTP is significantly correlated with RD and SH. It is also worth noting that the variations of the total heat in each summer month are not significantly correlated with each other.

In Chapters 3 and 4, the different origins and impacts are explored for the interannual variations in the summer heat sources over the western, central, and eastern TP, using the newly developed heat source dataset and conducting several numerical model experiments. Correlation

results suggest that the ETP heating is strongly correlated with the negative summer NAO; the CTP heating is closely linked with El Niño; the WTP heating is highly correlated with the WP cooling-CP warming and negatively correlated with the tropical Atlantic SSTA. AGCM experiments have verified the effects of the remote SSTA forcings on the TP heating variations. The direct wave responses to the ETP, CTP, and WTP heating forcings have large differences. The ETP heating generates an upper-level wave train propagating eastward to the northwestern Pacific. The wave train produced by the CTP heating is propagating to north-central Pacific. The WTP heating excites a wave train that splits into two branches: the northern one propagates northeastward to the Arctic region and the southern one propagates eastward to coastal northwestern Pacific. The WTP-heating induced upper-level anticyclones can cause near-surface warming in southeastern China and polar Asia.

In Chapter 5, future changes of summer latent heat released from precipitation and SH over the eastern TP are investigated with 22 CMIP6 models' outputs. The latent heat is represented by the variable precipitation. Nearly all models can simulate the observed climatological precipitation pattern (1979–2014) but overestimate it by a mean bias of 2.1 mm day^{-1} (or 65%). SH has scarcely been evaluated, and we found that one-third of the models cannot capture its spatial structure, and most models underestimate it with a mean bias of -6.1 W m^{-2} (or -12.7%). The models with high performance are selected, and their multimodel ensemble mean (MME) projects that, under the medium emission scenario (SSP2-4.5), the summer precipitation in 2065–2100 is 6.2% higher than the historical 1979–2014 mean, and it will likely increase 2.7% per one degree of global warming due to the remarkable enhancement of surface evaporation and vertical moisture transport that are partially offset by weakening ascending motion. The SH is projected to be likely unchanged due to a considerable intermodel spread, which is related to the likely unaltered surface wind speed.

6.2. Discussion and Future Work

As a first attempt to comprehensively investigate the total summer heat source and its three components over the data-sparse central-western TP, the observation-validated study in Chapter 1 could improve the accuracy in the heat source estimation over the TP, especially the station-void WTP. This new reliable estimate of the summer heat sources over the TP is very important for relevant model evaluations, climate change research, and future climate predictions. With the complex topography and climate patterns seen in the TP, there is still a need for a higher station density and more in situ observations to fully understand the climate variability in the heat sources over the TP.

Chapters 3 and 4 only adopted a coarse-resolution AGCM to conduct experiments in order to emphasize the role of the prescribed heating or SSTA. In the future, experiments using high-resolution model are needed to examine the accuracy of the current results, and the coupled model experiments also need to be conducted to explore the effect of air-sea interaction.

In Chapter 5, the CMIP6 simulations have not been evidently improved compared to CMIP5 models, indicating that the systematic model deficiencies still exist. The biases over the TP may be related to the coarse model resolutions and the deficient physical parameterization. Many local processes induced by the complex topography cannot be fully captured by the models. Further study is needed to explore the specific causes of biases to improve the performance of future climate models. Moreover, the TP heating's impacts can be examined using CMIP6 model products, and the future change of the impacts is also an interesting topic.

Bibliography

Adler, R.F., and Coauthors, 2003: Global Precipitation Climatology Project (GPCP) Monthly Precipitation Analysis (1979-Present), version 2.2. NOAA/OAR/ESRL PSD, accessed 14 October 2015, https://www.esrl.noaa.gov/psd/data/gridded/data.gpcp.html.

Beaudoing, H., and M. Rodell, NASA/GSFC/HSL, 2015: GLDAS Noah Land Surface Model L4 monthly 1.0 x 1.0 degree, version 2.0. GES DISC, accessed 7 February 2017, https://doi.org/10.5067/QN80TO7ZHFJZ.

Beaudoing, H., and M. Rodell, NASA/GSFC/HSL, 2016: GLDAS Noah Land Surface Model L4 monthly 1.0 x 1.0 degree V2.1. GES DISC, accessed 20 June 2018, https://doi.org/10.5067/LWTYSMP3VM5Z.

Blanford, H. F., 1884: On the connection of the Himalaya snowfall with dry winds and seasons of drought in India. *Proc. Roy. Soc. London*, **37**, 3–22, https://doi.org/10.1098/rspl.1884.0003.

Bolin, B., 1950: On the influence of the earth's orography on the general character of the westerlies. *Tellus*, **2**, 184-195, https://doi.org/10.3402/tellusa.v2i3.8547.

Bolton, D., 1980: The computation of equivalent potential temperature. *Mon. Wea. Rev.*, **108**, 1046–1053, https://doi.org/10.1175/1520-0493(1980)108<1046:TCOEPT>2.0.CO;2.

Bothe, O., K. Fraedrich, and X. Zhu, 2010: The large-scale circulations and summer drought and wetness on the Tibetan plateau. *Int. J. Climatol.*, **30**, 844-855, https://doi.org/10.1002/joc.1946.

Chang, C.-P., Z. Wang, and H. Hendon, 2006: The Asian winter monsoon. *The Asian Monsoon*, B. Wang, Ed., Springer, 89–127.

Chen, B., W. Chao, and X. Liu, 2003: Enhanced climatic warming in the Tibetan Plateau due to doubling CO2: a model study. *Climate Dynamics*, **20**, 401-413, https://doi.org/10.1007/s00382-002-0282-4.

Chen, H., T. Zhou, R. B. Neale, X. Wu, and G. Zhang, 2010: Performance of the new NCAR CAM3. 5 in East Asian summer monsoon simulations: Sensitivity to modifications of the convection scheme. *J. Clim.*, **23**, 3657-3675, https://doi.org/10.1175/2010JCLI3022.1.

Chen, J., X. Wu, Y. Yin, and H. Xiao, 2015: Characteristics of heat sources and clouds over eastern China and the Tibetan Plateau in boreal summer. *J. Climate*, **28**, 7279–7296, https://doi.org/10.1175/JCLI-D-14-00859.1.

Chen, L., and O.W. Frauenfeld, 2014a: A comprehensive evaluation of precipitation simulations over China based on CMIP5 multimodel ensemble projections. *Journal of Geophysical Research: Atmospheres*, **119**, 5767-5786, https://doi.org/10.1002/2013JD021190.

Chen, L., and O.W. Frauenfeld, 2014b: Surface air temperature changes over the twentieth and twenty-first centuries in China simulated by 20 CMIP5 models. *Journal of Climate*, **27**, 3920-3937, https://doi.org/10.1175/JCLI-D-13-00465.1.

Chen, M., P. Xie, J. E. Janowiak, and P. A. Arkin, 2002: NOAA's Precipitation Reconstruction over Land (PREC/L). NOAA/OAR/ESRL PSD, accessed 14 October 2015, https://www.esrl.noaa.gov/psd/data/gridded/data.precl.html.

Cheng, G. and Wu, T., 2007. Responses of permafrost to climate change and their environmental significance, Qinghai-Tibet Plateau. *Journal of Geophysical Research: Earth Surface*, **112**, F02S03, https://doi.org/10.1029/2006JF000631.

Cui, Y., A. Duan, Y. Liu, and G. Wu, 2015: Interannual variability of the spring atmospheric heat source over the Tibetan Plateau forced by the North Atlantic SSTA. *Climate Dyn.*, **45**, 1617-1634, https://doi.org/10.1007/s00382-014-2417-9.

Dee, D. P., and Coauthors, 2011a: ERA-Interim reanalysis. ECMWF datasets, accessed 3 February 2017, https://www.ecmwf.int/en/forecasts/datasets/reanalysis-datasets/era-interim.

Dee, D. P., and Coauthors, 2011b: The ERA-Interim reanalysis: Configuration and performance of the data assimilation system. *Q. J. R. Meteor. Soc.*, **13**, 553-597, https://doi.org/10.1002/qj.828.

Duan, A., J. Hu, and Z. Xiao, 2013a: The Tibetan Plateau summer monsoon in the CMIP5 simulations. *Journal of Climate*, **26**, 7747-7766, https://doi.org/10.1175/JCLI-D-12-00685.1.

Duan, A., R. Sun, and J. He, 2017: Impact of surface sensible heating over the Tibetan Plateau on the western Pacific subtropical high: A land–air–sea interaction perspective. *Advances in Atmospheric Sciences*, **34**, 157-168, https://doi.org/10.1007/s00376-016-6008-z.

Duan, A., M. Wang, Y. Lei, and Y. Cui, 2013b: Trends in summer rainfall over China associated with the Tibetan Plateau sensible heat source during 1980–2008. *J. Climate*, **26**, 261-275, https://doi.org/10.1175/JCLI-D-11-00669.1.

Duan, A., M. Wang, and Z. Xiao, 2014: Uncertainties in quantitatively estimating the atmospheric heat source over the Tibetan Plateau. *Atmospheric and Oceanic Science Letters*, 7(1), pp.28-33, https://doi.org/10.1080/16742834.2014.11447131.

Duan, A., and G. Wu, 2005: Role of the Tibetan Plateau thermal forcing in the summer climate patterns over subtropical Asia. *Climate Dyn.*, **24**, 793–807, https://doi.org/10.1007/s00382-004-0488-8.

Duan, A., and G. Wu, 2006: Change of cloud amount and the climate warming on the Tibetan Plateau. *Geophys. Res. Lett.*, **33**, https://doi.org/10.1029/2006GL027946.

Duan, A., and G. Wu, 2008: Weakening trend in the atmospheric heat source over the Tibetan Plateau during recent decades. Part I: Observations. *J. Climate*, **21**, 3149–3164, https://doi.org/10.1175/2007JCLI1912.1.

Duan, A., and G. Wu, 2009: Weakening trend in the atmospheric heat source over the Tibetan Plateau during recent decades. Part II: Connection with climate warming. *J. Climate*, **22**, 4197-4212, https://doi.org/10.1175/2009JCLI2699.1.

Duan, A., and Z. Xiao, 2015: Does the climate warming hiatus exist over the Tibetan Plateau? *Scientific Reports*, *5*, https://doi.org/10.1038/srep13711.

Dou, J., Z. Wu, and Y. Zhou, 2017: Potential impact of the May Southern Hemisphere annular mode on the Indian summer monsoon rainfall. *Climate Dyn.*, **49**, 1257-1269, https://doi.org/10.1007/s00382-016-3380-4.

Eyring, V., S. Bony, G.A. Meehl, C.A. Senior, B. Stevens, R.J. Stouffer, and K.E. Taylor, 2016: Overview of the Coupled Model Intercomparison Project Phase 6 (CMIP6) experimental design and organization. *Geosci. Model Dev.*, **9**, 1937–1958, https://doi.org/10.5194/gmd-9-1937-2016.

Flohn, H., 1957: Large-scale aspects of the "summer monsoon" in South and East Asia. *J. Meteor. Soc. Japan*, **35**, 180-186. https://doi.org/10.2151/jmsj1923.35A.0_180.

Flohn, H., 1981: The elevated heat source of the Tibetan highlands and its role for the large-scale atmospheric circulation. *Geological and ecological studies of the Qinghai-Xizang Plateau*, **2**, 1463-1469.

Folland, C. K., J. Knight, H. W. Linderholm, D. Fereday, S. Ineson, and J. W. Hurrell, 2009: The summer North Atlantic Oscillation: Past, present, and future. *J. Climate*, **22**, 1082–1103, https://doi.org/10.1175/2008JCLI2459.1.

Gao, Y.-X., M.-C. Tang, S.-W. Luo, Z.-B. Shen, and C. Li, 1981: Some aspects of recent research on the Qinghai-Xizang Plateau meteorology. *Bulletin of the American Meteorological Society*, **62**, 31–35, https://doi.org/10.1175/1520-0477(1981)062<0031:SAORRO>2.0.CO;2.

Gelaro, R. and co-authors, 2017: The Modern-Era Retrospective Analysis for Research and Applications, Version 2 (MERRA-2). *J. Climate*, **30**, 5419-5454, https://doi.org/10.1175/JCLI-D-16-0758.1.

Giorgi, F., and M. R. Marinucci, 1996: A investigation of the sensitivity of simulated precipitation to model resolution and its implications for climate studies. *Mon. Wea. Rev.*, **124**, 148-166, https://doi.org/10.1175/1520-0493(1996)124<0148:AIOTSO>2.0.CO;2.

GMAO, 2015: MERRA-2 tavgM_2d_flx_Nx: 2d, Monthly mean, time-averaged, single-level surface flux diagnostics, version 5.12.4. GES DISC, accessed 3 February 2017, https://doi.org/10.5067/0JRLVL8YV2Y4.

Hack, J. J., 1994: Parameterization of moist convection in the National Center for Atmospheric Research Community Climate Model (CCM2). *J. Geophys. Res*., **99**, 5551–5568, https://doi.org/10.1029/93JD03478.

He, B., Y. Liu, G. Wu, Z. Wang, and Q. Bao, 2019: The role of air-sea interactions in regulating the thermal effect of the Tibetan–Iranian Plateau on the Asian summer monsoon. *Clim. Dyn.*, **52**, 4227-4245, https://doi.org/10.1007/s00382-018-4377-y.

Held, I. M., and B. J. Soden 2006: Robust responses of the hydrological cycle to global warming. *J. Clim.*, **19**, 5686-5699, https://doi.org/10.1175/JCLI3990.1.

Hoskins, B. J., and D. J. Karoly, 1981: The steady linear response of a spherical atmosphere to thermal and orographic forcing. *J. Atmos. Sci.*, **38**, 1179-1196, https://doi.org/10.1175/1520-0469(1981)038<1179:TSLROA>2.0.CO;2.

Hsu, H.-H., and X. Liu, 2003: Relationship between the Tibetan Plateau heating and East Asian summer monsoon rainfall. *Geophys. Res. Lett.*, **30**, 2066, https://doi.org/10.1029/2003GL017909.

Hu, J., and A. Duan, 2015: Relative contributions of the Tibetan Plateau thermal forcing and the Indian Ocean Sea surface temperature basin mode to the interannual variability of the East Asian summer monsoon. *Climate Dyn.*, **45**, 2697-2711, https://doi.org/10.1007/s00382-015-2503-7.

Hu, S., T. Zhou, and B. Wu, 2021: Impact of Developing ENSO on Tibetan Plateau Summer Rainfall. *J. Climate*, **34**, 3385-3400, https://doi.org/10.1175/JCLI-D-20-0612.1.

Huang, B., and Coauthors, 2017: Extended Reconstructed Sea Surface Temperature version 5 (ERSSTv5): Upgrades, validations, and intercomparisons. *J. Climate*, **30**, 8179-8205, https://doi.org/10.1175/JCLI-D-16-0836.1.

Huang, P., S.P. Xie, K. Hu, G. Huang, and R. Huang, 2013: Patterns of the seasonal response of tropical rainfall to global warming. *Nature Geoscience*, **6**, 357-361, https://doi.org/10.1038/ngeo1792.

Jia, K., Y. Ruan, Y. Yang, and Z. You, 2019a: Assessment of CMIP5 GCM simulation performance for temperature projection in the Tibetan Plateau. *Earth and Space Science*, **6**, 2362-2378, https://doi.org/10.1029/2019EA000962.

Jia, K., Y. Ruan, Y. Yang, and C. Zhang, 2019b: Assessing the Performance of CMIP5 Global Climate Models for Simulating Future Precipitation Change in the Tibetan Plateau. *Water*, **11**, 1771, https://doi.org/10.3390/w11091771.

Jiang, X., Y. Li, S. Yang, K. Yang, and J. Chen, 2016: Interannual variation of summer atmospheric heat source over the Tibetan Plateau and the role of convection around the western Maritime Continent. *J. Climate*, **29**, 121–138, https://doi.org/10.1175/JCLI-D-15-0181.1.

Jin, C., B. Wang, and J. Liu, 2020: Future changes and controlling factors of the eight regional monsoons projected by CMIP6 models. *J. Clim.*, **33**, 9307–9326, https://doi.org/10.1175/JCLI-D-20-0236.1.

Jin, F.-F., and B. J. Hoskins, 1995: The direct response to tropical heating in a baroclinic atmosphere. *J. Atmos. Sci.*, **52**, 307-319, https://doi.org/10.1175/1520-0469(1995)052<0307:TDRTTH>2.0.CO;2.

JMA, and Central Research Institute of Electric Power Industry/Japan, 2008: JRA-25, monthly means. NCAR Computational and Information Systems Laboratory Research Data Archive, accessed 9 March 2017, http://rda.ucar.edu/datasets/ds625.1/.

JMA, 2013: JRA-55, monthly means and variances. NCAR Computational and Information Systems Laboratory Research Data Archive, accessed 15 October 2015, https://doi.org/10.5065/D60G3H5B.

Jung, M., and Coauthors, 2011: Global patterns of land-atmosphere fluxes of carbon dioxide, latent heat, and sensible heat derived from eddy covariance, satellite, and meteorological observations. *J. Geophys. Res.: Biogeosci.*, **116**, G00J07, https://doi.org/10.1029/2010jg001566.

Kanamitsu, M., W. Ebisuzaki, J. Woollen, S. Yang, J.J. Hnilo, M. Fiorino, and G. L. Potter, 2002: NCEP-DOE Reanalysis 2. NOAA/OAR/ESRL PSD, accessed 3 February 2017, https://www.esrl.noaa.gov/psd/data/gridded/data.ncep.reanalysis2.html.

Kang, H. S., and S. Y. Hong, 2008: Sensitivity of the simulated East Asian summer monsoon climatology to four convective parameterization schemes. *J. Geophys. Res.: Atmos.*, **113**, D15119, https://doi.org/10.1029/2007JD009692.

Kang, S., Y. Xu, Q. You, W. A. Flügel, N. Pepin, and T. Yao, 2010: Review of climate and cryospheric change in the Tibetan Plateau. *Environ. Res. Lett.*, **5**, 015101, https://doi.org/10.1088/1748-9326/5/1/015101.

Kato, S., and Coauthors, 2018: Surface irradiances of Edition 4.0 Clouds and the Earth's Radiant Energy System (CERES) Energy Balanced and Filled (EBAF) data product. *J. Climate*, **31**, 4501-4527, https://doi.org/10.1175/JCLI-D-17-0523.1.

Koo, C.-C., 1951: On the importance of the dynamical influence of Tibetan Plateau on the circulation over East Asia (in Chinese). *Sci. Sinica*, **2**, 283-303.

Li, C., and M. Yanai, 1996: The onset and interannual variability of the Asian summer monsoon in relation to land-sea thermal contrast. *Journal of Climate*, **9**, 358-375, https://doi.org/10.1175/1520-0442(1996)009<0358:TOAIVO>2.0.CO;2.

Li, J., Y.-M. Yang, and B. Wang, 2018: Evaluation of NESMv3 and CMIP5 Models' Performance on Simulation of Asian-Australian Monsoon. *Atmosphere* 9, 327, https://doi.org/10.3390/atmos9090327.

Li, G., T. Duan, and Y. Gong, 2000: The bulk transfer coefficients and surface fluxes on the western Tibetan Plateau. *Chin. Sci. Bull.*, **45**, 1221–1226, https://doi.org/10.1007/BF02886084.

Lin, C., K. Yang, J. Qin, R. Fu, 2013: Observed coherent trends of surface and upper-air wind speed over China since 1960. *J. Climate*. **26**, 2891–2903. https://doi.org/10.1175/JCLI-D-12-00093.1.

Liu, X., and B. Chen, 2000: Climatic warming in the Tibetan Plateau during recent decades. *International Journal of Climatology: A Journal of the Royal Meteorological Society*, **20**, 1729-1742, https://doi.org/10.1002/1097-0088(20001130)20:14<1729::AID-JOC556>3.0.CO;2-Y.

Liu, X., W. Li, and G. Wu, 2002: Interannual variation of the diabatic heating over the Tibetan plateau and the Northern Hemispheric circulation in summer. *Acta Meteor. Sin*, **60**, 267-277.

Liu, X., G. Wu, and W. Li, 2001: Thermal adaptation of the large-scale circulation to the summer heating over the Tibetan Plateau. *Prog. Nat. Sci.*, **11**, 207-214.

Liu, X., and Z. Yin, 2001: Spatial and temporal variation of summer precipitation over the eastern Tibetan Plateau and the North Atlantic oscillation *J. Climate*, **14**, 2896-2909, https://doi.org/10.1175/1520-0442(2001)014<2896:SATVOS>2.0.CO;2.

Loeb, N. G., and Coauthors, 2018: Clouds and the Earth's Radiant Energy System (CERES) Energy Balanced and Filled (EBAF) Top-of-Atmosphere (TOA) Edition-4.0 Data Product. *J. Climate*, **31**, 895-918, https://doi.org/10.1175/JCLI-D-17-0208.1.

Lu, M., S. Yang, Z. Li, B. He, S. He, and Z. Wang, 2018: Possible effect of the Tibetan Plateau on the "upstream" climate over West Asia, North Africa, South Europe and the North Atlantic. *Climate Dyn.*, **51**, 1485-1498, https://doi.org/10.1007/s00382-017-3966-5.

Luo, H., and M. Yanai, 1984: The large-scale circulation and heat sources over the Tibetan Plateau and surrounding areas during the early summer of 1979. Part II: Heat and moisture budgets. *Mon. Wea. Rev.*, **112**, 966–989, https://doi.org/10.1175/1520-0493(1984)112<0966:TLSCAH>2.0.CO;2.

Ma, J., X. Guan, R. Guo, Z. Gan, and Y. Xie, 2017: Mechanism of non-appearance of hiatus in Tibetan Plateau. *Sci. Rep.*, **7**, 4421, https://doi.org/10.1038/s41598-017-04615-7.

Mastrandrea, M. D., and Coauthors, 2010: Guidance note for lead authors of the IPCC fifth assessment report on consistent treatment of uncertainties. *Intergovernmental Panel on Climate Change (IPCC)*, http://www.ipcc.ch.

Murakami, T., and H. Nakamura, 1983: Orographic Effects on Cold Surges and Lee-Cyclogenesis as Revealed by a Numerical Experiment Part II. Transient Aspects. *J. Meteor. Soc. Japan, Ser. II*, **61**, 547-567, https://doi.org/10.2151/jmsj1965.61.4_547.

Neale, R. B., and Coauthors, 2010: Description of the NCAR Community Atmosphere Model (CAM 4.0). NCAR Tech. Note, NCAR/TN-4851STR. [Available online at http://www.cesm.ucar.edu/models/ccsm4.0/cam/docs/description/cam4_desc.pdf.]

Neale, R. B., J. H. Richter, and M. Jochum, 2008: The impact of convection on ENSO: From a delayed oscillator to a series of events. *J. Climate*, **21**, 5904–5924, https://doi.org/10.1175/2008JCLI2244.1.

Neelin, J. D., A. Bracco, H. Luo, J. C. McWilliams, and J. E. Meyerson, 2010: Considerations for parameter optimization and sensitivity in climate models. *Pro. Natl. Acad. Sci.*, **107**, 21349-21354, https://doi.org/10.1073/pnas.1015473107.

O'Neill, B.C., C. Tebaldi, D.P. van Vuuren, V. Eyring, P. Friedlingstein, G. Hurtt, R. Knutti, E. Kriegler, J.F. Lamarque, J. Lowe, and G.A. Meehl, 2016: The scenario model intercomparison project (ScenarioMIP) for CMIP6. *Geosci. Model Dev.*, **9**, 3461–3482, https://doi.org/10.5194/gmd-9-3461-2016.

Rajagopalan, B., and P. Molnar, 2013: Signatures of Tibetan Plateau heating on Indian summer monsoon rainfall variability. *Journal of Geophysical Research: Atmospheres*, **118**, 1170-1178, https://doi.org/10.1002/jgrd.50124.

Rasch, P. J., and J. E. Kristjansson, 1998: A comparison of the CCM3 model climate using diagnosed and predicted condensate parameterizations. *J. Climate*, **11**, 1587–1613, https://doi.org/10.1175/1520-0442(1998)011<1587:ACOTCM>2.0.CO;2.

Raschke, E. A., and P. W. Stackhouse Jr., 2011: GEWEX Radiation Flux Assessment Status and Early Results. *GEWEX News*, **21**(1), 4–5, https://www.gewex.org/gewex-content/files_mf/1432209318Feb2011.pdf.

Reichle, R. H., and Q. Liu, 2014: Observation-corrected precipitation estimates in GEOS-5. Technical Report Series on Global Modelling and Data Assimilation, Vol. 35, NASA Tech. Rep. NASA/TM–2014–104606, 24 pp. [Available on-line at https://ntrs.nasa.gov/archive/nasa/casi.ntrs.nasa.gov/20150000725.pdf.]

Riahi, K., D.P. van Vuuren, E. Kriegler, J. Edmonds, B.C. O'neill, S. Fujimori, N. Bauer, K. Calvin, R. Dellink, O. Fricko, and W. Lutz, 2017: The shared socioeconomic pathways and their energy, land use, and greenhouse gas emissions implications: an overview. *Global Environmental Change*, **42**, 153-168, https://doi.org/10.1016/j.gloenvcha.2016.05.009.

Rodell, M., and Coauthors, 2004: The Global Land Data Assimilation System. *Bull. Amer. Meteor. Soc.*, **85**, 381-394, https://doi.org/10.1175/BAMS-85-3-381.

Rui, H., and H. Beaudoing, 2018: README Document for NASA GLDAS Version 2 Data Products. GES DISC. [Available on-line at https://hydro1.gesdisc.eosdis.nasa.gov/data/GLDAS/README_GLDAS2.pdf]

Saha, S., and Coauthors, 2010: NCEP CFSR Monthly Products, January 1979 to December 2010. NCAR Computational and Information Systems Laboratory Research Data Archive, accessed 16 May 2016, https://doi.org/10.5065/D6DN438J.

Salunke, P., S. Jain, and S.K. Mishra, 2018: Performance of the CMIP5 models in the simulation of the Himalaya-Tibetan Plateau monsoon. *Theoretical and Applied Climatology*, *137*(1-2), https://doi. org/10.1007/s00704-018-2644-9.

Schneider, U., A. Becker, P. Finger, A. Meyer-Christoffer, B. Rudolf, M. Ziese, 2011: GPCC Full Data Reanalysis Version 6.0 at 1.0°: Monthly Land-Surface Precipitation from Rain-Gauges built on GTS-based and Historic Data. https://doi.org/10.5676/DWD_GPCC/FD_M_V7_100.

Shi, Q., and S. Liang, 2014: Surface-sensible and latent heat fluxes over the Tibetan Plateau from ground measurements, reanalysis, and satellite data. *Atmos. Chem. Phys.*, **14**, 5659–5677, https://doi.org/10.5194/acp-14-5659-2014.

Song, C., B. Huang, L. Ke, and Q. Ye, 2016: Precipitation variability in High Mountain Asia from multiple datasets and implication for water balance analysis in large lake basins. *Global Planet. Change*, **145**, 20-29, https://doi.org/10.1016/j.gloplacha.2016.08.005.

SRB Science Team, 2010: NASA/GEWAX SRB, Release 3.0. NASA ASDC, accessed 13 November 2015, https://doi.org/10.5067/SRB/REL3.0_SW_MONTHLY_UTC_NC_L3.

SRB Science Team, 2012: NASA/GEWAX SRB, Release 3.1. NASA ASDC, accessed 13 November 2015, https://doi.org/10.5067/SRB/REL3.1_LW_MONTHLY_NC_L2.

Stackhouse Jr., P. W., S. K. Gupta, S. J. Cox, and T. Zhang, J. C. Mikovitz, and L. M. Hinkelman, 2011: The NASA/GEWEX surface radiation budget release 3.0: 24.5-year

dataset. *GEWEX News*, **21**(1), 10–12, https://www.gewex.org/gewex-content/files_mf/1432209318Feb2011.pdf.

Stevens, B., and Coauthors, 2013: Atmospheric component of the MPI-M earth system model: ECHAM6. *J. Adv. Modeling Earth Systems*, **5**, 146-172, https://doi.org/10.1002/jame.20015.

Su, F., X. Duan, D. Chen, Z. Hao, and L. Cuo, 2013: Evaluation of the global climate models in the CMIP5 over the Tibetan Plateau. *Journal of Climate*, **26**, 3187-3208, https://doi.org/10.1175/JCLI-D-12-00321.1.

Takaya, K., and H. Nakamura, 2001: A formulation of a phase-independent wave-activity flux for stationary and migratory quasigeostrophic eddies on a zonally varying basic flow. *J. Atmos. Sci.*, **58**, 608-627, https://doi.org/10.1175/1520-0469(2001)058<0608:AFOAPI>2.0.CO;2.

Tebaldi, C., and R. Knutti, 2007: The use of the multi-model ensemble in probabilistic climate projections. *Philosophical transactions of the royal society A: mathematical, physical and engineering sciences*, **365**, 2053-2075, https://doi.org/10.1098/rsta.2007.2076.

Ting, M., and L. Yu, 1998: Steady response to tropical heating in wavy linear and nonlinear baroclinic models. *J. Atmos. Sci*., **55**, 3565-3582, https://doi.org/10.1175/1520-0469(1998)055<3565:SRTTHI>2.0.CO;2.

Tong, K., F. Su, D. Yang, L. Zhang, and Z. Hao, 2014: Tibetan Plateau precipitation as depicted by gauge observations, reanalyses and satellite retrievals. *Int. J. Climatol.*, **34**, 265-285, https://doi.org/10.1002/joc.3682.

Ueda, H., and T. Yasunari, 1998: Role of warming over the Tibetan Plateau in early onset of the summer monsoon over the Bay of Bengal and the South China Sea. *Journal of the Meteorological Society of Japan. Ser. II*, **76**, 1-12, https://doi.org/10.2151/jmsj1965.76.1_1.

Veettil, B. K., 2012: A remote sensing approach for monitoring debris-covered glaciers in the high altitude Karakoram Himalayas. *Int. J. Geomatics Geosci.*, **2**, 833-841.

Wang, B., Q. Bao, B. Hoskins, G. Wu, and Y. Liu, 2008: Tibetan Plateau warming and precipitation changes in East Asia. *Geophys. Res. Lett.*, **35**, L14702, https://doi.org/10.1029/2008GL034330.

Wang B., C. Jin, and J. Liu, 2020: Understanding Future Change of Global Monsoons Projected by CMIP6 Models. *J. Clim.*, **33**, 6471–6489, https://doi.org/10.1175/JCLI-D-19-0993.1.

Wang, M., S. Zhou, and A. Duan, 2012: Trend in the atmospheric heat source over the central and eastern Tibetan Plateau during recent decades: Comparison of observations and reanalysis data. *Chin. Sci. Bull.*, **57**, 548–557, https://doi.org/10.1007/s11434-011-4838-8.

Wang, M., J. Wang, D. Chen, A. Duan, Y. Liu, S. Zhou, D. Guo, H. Wang, and W. Ju, 2019: Recent recovery of the boreal spring sensible heating over the Tibetan Plateau will continue in CMIP6 future projections. *Environ. Res. Lett.*, **14**, 124066, https://doi.org/10.1088/1748-9326/ab57a3.

Wang, Z., A. Duan, M. Li, and B. He, 2016: Influences of thermal forcing over the slope/platform of the Tibetan Plateau on Asian summer monsoon: Numerical studies with the WRF model. *Chinese J. Geophys.*, **59**, 474-487, https://doi.org/10.1002/cjg2.30007.

Wang, Z., A. Duan, and G. Wu, 2014: Time-lagged impact of spring sensible heat over the Tibetan Plateau on the summer rainfall anomaly in East China: case studies using the WRF model. *Climate Dyn.*, **42**, 2885–2898, https://doi.org/10.1007/s00382-013-1800-2.

Wang, Z., S. Yang, N. C. Lau, and A. Duan, 2018: Teleconnection between summer NAO and East China rainfall variations: a bridge effect of the Tibetan Plateau. *J. Climate*, **31**, 6433-6444, https://doi.org/10.1175/JCLI-D-17-0413.1.

Watanabe, M., and M. Kimoto, 2000: Atmosphere-ocean thermal coupling in the North Atlantic: A positive feedback. *Quart. J. Roy. Meteor. Soc.*, **126**, 3343–3369, https://doi.org/10.1002/qj.49712657017.

Wu, G., and Coauthors, 2007: The influence of mechanical and thermal forcing by the Tibetan Plateau on Asian climate. *J. Hydrometeor.*, **8**, 770–789, https://doi.org/10.1175/JHM609.1.

Wu, G., and Coauthors, 2015: Tibetan Plateau climate dynamics: recent research progress and outlook. *Natl. Sci. Rev.*, **2**, 100-116, https://doi.org/10.1093/nsr/nwu045.

Wu, G., B. He, A. Duan, Y. Liu, and W. Yu, 2017: Formation and variation of the atmospheric heat source over the Tibetan Plateau and its climate effects. *Adv. Atmos. Sci.*, **34**, 1169–1184, https://doi.org/10.1007/s00376-017-7014-5.

Wu, G., W. Li, H. Guo, H. Liu, J. Xue, and Z. Wang, 1997: Sensible heat driven air-pump over the Tibetan Plateau and its impacts on the Asian Summer Monsoon. *Collections on the Memory of Zhao Jiuzhang,* D. Ye, Ed., Chinese Science Press, 116-126.

Wu, G., Y. Liu, J. Mao, X. Liu, and W. Li, 2004: Adaptation of the atmospheric circulation to thermal forcing over the Tibetan Plateau. In *Observation, Theory and Modeling of Atmospheric Variability* (selected Papers of Nanjing Institute of Meteorology Alumni in Commemoration of Professor Jijia Zhang). World Scientific, Singapore, 92-114.

Wu, G., Y. Liu, B. He, Q. Bao, A. Duan, and F.F. Jin, 2012: Thermal controls on the Asian summer monsoon. *Scientific reports*, **2**, 404, https://doi.org/10.1038/srep00404.

Wu G., and Y. Zhang, 1998: Thermal and mechanical forcing of the Tibetan Plateau and Asian monsoon onset. Part I: Situating of the onset (in Chinese). *Chinese J. Atmos. Sci.*, **22,** 825-838, https://doi.org/10.3878/j.issn.1006-9895.1998.06.03.

Wu G, and Y. Zhang, 1999: Thermal and mechanical forcing of the Tibetan Plateau and Asian monsoon onset. Part II: Timing of the onset (in Chinese). *Chinese J. Atmos. Sci.*, **23,** 51-61, https://doi.org/10.3878/j.issn.1006-9895.1999.01.07.

Wu, G., H. Zhuo, Z. Wang, and Y. Liu, 2016: Two types of summertime heating over the Asian large-scale orography and excitation of potential-vorticity forcing I. Over Tibetan Plateau. *Science China Earth Sciences*, **59**,1996-2008, https://doi.org/10.1007/s11430-016-5328-2.

Wu, H., K. Yang, X. Niu, and Y. Chen, 2015: The role of cloud height and warming in the decadal weakening of atmospheric heat source over the Tibetan Plateau. *Sci. China Earth Sci.*, **58**, 395-403, https://doi.org/10.1007/s11430-014-4973-6.

Wu, J., and X.J. Gao, 2013: A gridded daily observation dataset over China region and comparison with the other datasets (in Chinese). *Chinese J. Geophys*, **56**, 1102-1111, https://doi.org/10.6038/cjg20130406.

Wu, Z., J. Li, Z. Jiang, and T. Ma, 2012: Modulation of the Tibetan Plateau snow cover on the ENSO teleconnections: From the East Asian summer monsoon perspective. *J. Climate*, **25**, 2481–2489, https://doi.org/10.1175/JCLI-D-11-00135.1.

Wu, Z., P. Zhang, H. Chen, and Y. Li, 2016: Can the Tibetan Plateau snow cover influence the interannual variations of Eurasian heat wave frequency? *Climate Dyn.*, **46**, 3405-3417, https://doi.org/10.1007/s00382-015-2775-y.

Xiao, Z., and A. Duan, 2016: Impacts of Tibetan Plateau snow cover on the interannual variability of the East Asia summer monsoon. *J. Climate*, **29**, 8495-8514, https://doi.org/10.1175/JCLI-D-16-0029.1.

Xiao, Z., W. Shi, and P. Yang, 2015: Possible causes of the interdecadal transition of the Somali jet around the late 1990s. *J. Meteor. Res.*, **29**, 214-227, https://doi.org/10.1007/s13351-015-4103-1.

Xie, P., and P.A. Arkin, 1997: CMAP. NOAA/OAR/ESRL PSD, accessed 25 September 2017, https://www.esrl.noaa.gov/psd/data/gridded/data.cmap.html.

Xie, Z., and B. Wang, 2019: Summer Atmospheric Heat Sources over the Western–Central Tibetan Plateau: An Integrated Analysis of Multiple Reanalysis and Satellite Datasets. *J. Climate*, **32**, 1181-1202, https://doi.org/10.1175/JCLI-D-18-0176.1.

Xie, Z., and B. Wang, 2021: Summer Heat Sources Changes over the Tibetan Plateau in CMIP6. *Environ. Res. Lett*, **16**, 064060, https://doi.org/10.1088/1748-9326/ac0279.

Xu, W., L. Ma, M. Ma, H. Zhang, and W. Yuan, 2017: Spatial–temporal variability of snow cover and depth in the Qinghai–Tibetan Plateau. *J. Climate*, **30**, 1521-1533, https://doi.org/10.1175/JCLI-D-15-0732.1.

Xu, X., C. Lu, Y. Ding, X. Shi, Y. Guo, and W. Zhu, 2013: What is the relationship between China summer precipitation and the change of apparent heat source over the Tibetan Plateau? *Atmos. Sci. Lett.*, **14**, 227–234, https://doi.org/10.1002/asl2.444.

Xu, Z., T. Gong, and J. Li, 2008: Decadal trend of climate in the Tibetan Plateau - regional temperature and precipitation. *Hydrological Processes: An International Journal*, **22**, 3056-3065, https://doi.org/10.1002/hyp.6892.

Yanai, M., S. Esbensen, and J. H. Chu, 1973: Determination of bulk properties of tropical cloud clusters from large-scale heat and moisture budgets. *J. Atmos. Sci*., **30**, 611-627, https://doi.org/10.1175/1520-0469(1973)030<0611:DOBPOT>2.0.CO;2.

Yanai, M., C. Li, and Z. Song, 1992: Seasonal heating of the Tibetan Plateau and its effects on the evolution of the Asian summer monsoon. *J. Meteor. Soc. Japan*, **70**, 319–351, https://doi.org/10.2151/ jmsj1965.70.1B_319.

Yanai, M., and C. Li, 1994: Mechanism of heating and the boundary layer over the Tibetan Plateau. *Mon. Wea. Rev.*, **122**, 305–323, https://doi.org/10.1175/1520-0493(1994)122<0305:MOHATB>2.0.CO;2.

Yanai, M., and G. Wu, 2006: Effects of the Tibetan Plateau. *The Asian Monsoon*, B. Wang, Ed., Springer, 513–549.

Yang, K., T. Koike, and D. Yang, 2003: Surface Flux Parameterization in the Tibetan Plateau. *Boundary-Layer Meteorology*, 106, 245–262. https://doi.org/10.1023/A:1021152407334.

Yang, K., T. Koike, P. Stackhouse, C. Mikovitz, and S. J. Cox, 2006: An assessment of satellite surface radiation products for highlands with Tibet instrumental data. *Geophys. Res. Lett.*, **33**, L22403, https://doi.org/10.1029/2006GL027640.

Yang, K., X. Guo, and B. Wu, 2010: Recent trends in surface sensible heat flux on the Tibetan Plateau. *Sci. China Earth Sci.*, **54**, 19–28, https://doi.org/10.1007/s11430-010-4036-6.

Yang, K., X. Guo, J. He, J. Qin, and T. Koike, 2011: On the Climatology and Trend of the Atmospheric Heat Source over the Tibetan Plateau: An Experiments-Supported Revisit. *J. Climate*, **24**, 1525–1541, https://doi.org/10.1175/2010JCLI3848.1.

Yang, K., H. Wu, J. Qin, C. Lin, W. Tang, and Y. Chen, 2014: Recent climate changes over the Tibetan Plateau and their impacts on energy and water cycle: A review. *Global Planet. Change*, **112**, 79-91, https://doi.org/10.1016/j.gloplacha.2013.12.001.

Yao, T., and Coauthors, 2019: Recent third pole's rapid warming accompanies cryospheric melt and water cycle intensification and interactions between monsoon and environment: Multidisciplinary approach with observations, modeling, and analysis. *Bull. Amer. Meteor. Soc.*, **100**, 423-444, https://doi.org/10.1175/BAMS-D-17-0057.1.

Yatagai, A., K. Kamiguchi, O. Arakawa, A. Hamada, N. Yasutomi, and A. Kitoh, 2012: APHRODITE. Subset used: Monsoon Asia Precipitation (APHRO_MA), APHRODITE's Water Resources, accessed 10 November 2015, http://www.chikyu.ac.jp/precip/english/products.html.

Ye, D., and Y. Gao, 1979: *The Meteorology of the Qinghai-Xizang (Tibet) Plateau* (in Chinese). Science Press, 278 pp.

Ye, D., and G. Wu, 1998: The role of the heat source of the Tibetan Plateau in the general circulation. *Meteorology and Atmospheric Physics,* **67**, 181–198, https://doi.org/10.1007/BF01277509.

Yeh, T.-C., 1950: The circulation of the high troposphere over China in the winter of 1945–46. *Tellus*, **2**, 173-183, https://doi.org/10.1111/j.2153-3490.1950.tb00329.x.

Yeh, T.-C., S.-W. Lo, and P.-C. Chu, 1957: The wind structure and heat balance in the lower troposphere over the Tibetan Plateau and its surroundings (in Chinese). *Acta. Meteor. Sinica*, **28**, 108-121, https://doi.org/10.11676/qxxb1957.010.

You, Q., J. Min, W. Zhang, N. Pepin, and S. Kang, 2015: Comparison of multiple datasets with gridded precipitation observations over the Tibetan Plateau. *Climate Dyn.*, **45**, 1–16, https://doi.org/10.1007/s00382-014-2310-6.

You, Q., J. Min, S. Kang, 2016: Rapid warming in the Tibetan Plateau from observations and CMIP5 models in recent decades. *International Journal of Climatology*, **36**, 2660-70, https://doi.org/10.1002/joc.4520.

You, Q., D. Wang, Z. Jiang, and S. Kang, 2017: Diurnal temperature range in CMIP5 models and observations on the Tibetan Plateau. *Quarterly Journal of the Royal Meteorological Society*, **143**, 1978-1989, https://doi.org/10.1002/qj.3057.

Zhang, G. J., and N. A. McFarlane, 1995: Sensitivity of climate simulations to the parameterization of cumulus convection in the Canadian Climate Centre general circulation model. *Atmosphere-Ocean*, **33**, 407–446, https://doi.org/10.1080/07055900.1995.9649539.

Zhang, M., W. Lin, C. S. Bretherton, J. J. Hack, and P. J. Rasch, 2003: A modified formulation of fractional stratiform condensation rate in the NCAR Community Atmospheric Model (CAM2). *J. Geophys. Res*., **108**, 4035, doi:10.1029/2002JD002523.

Zhang, Q., G. Wu, and Y. Qian, 2002: The Bimodality of the 100 hPa South Asia High and its Relationship to the Climate Anomaly over East Asia in Summer. *Journal of the Meteorological Society of Japan*, **80**, 733-744. https://doi.org/10.2151/jmsj.80.733.

Zhang, Q., H. Körnich, and K. Holmgren, 2013: How well do reanalyses represent the southern African precipitation? *Climate Dyn.*, **40**, 951-962, https://doi.org/10.1007/s00382-012-1423-z.

Zhang, Y.-C., W. B. Rossow, A. A. Lacis, V. Oinas, and M. I. Mishchenko, 2004: Calculation of radiative fluxes from the surface to top of atmosphere based on ISCCP and other global data sets: Refinements of the radiative transfer model and the input data. *J. Geophys. Res.: Atmos.*, **109**, D19105, https://doi.org/10.1029/2003JD004457.

Zhang, Y.-C., W. B. Rossow, and P. W. Stackhouse, 2006: Comparison of different global information sources used in surface radiative flux calculation: Radiative properties of the near-surface atmosphere. *J. Geophys. Res.: Atmos.*, **111**, D13106, https://doi.org/10.1029/2005JD006873.

Zhang, Y.-C., W. B. Rossow, and P. W. Stackhouse, 2007: Comparison of different global information sources used in surface radiative flux calculation: Radiative properties of the surface. *J. Geophys. Res.: Atmos.*, **112**, D01102, https://doi.org/10.1029/2005JD007008.

Zhang, Y.-S., T. Li, and B. Wang, 2004: Decadal change of the spring snow depth over the Tibetan Plateau: The associated circulation and influence on the East Asian summer monsoon. *J. Climate*, **17**, 2780-2793, https://doi.org/10.1175/1520-0442(2004)017<2780:DCOTSS>2.0.CO;2.

Zhao, P. and L. Chen, 2001: Interannual variability of atmospheric heat source/sink over the Qinghai—Xizang (Tibetan) Plateau and its relation to circulation. *Adv. Atmos. Sci.*, **18**, 106–116, https://doi.org/10.1007/s00376-001-0007-3.

Zhou, X., P. Zhao, J. Chen, L. Chen, and W. Li, 2009: Impacts of thermodynamic processes over the Tibetan Plateau on the Northern Hemispheric climate. *Sci. China Ser. D-Earth Sci.*, **52**, 1679–1693, https://doi.org/10.1007/s11430-009-0194-9.

Zhu, L., G. Huang, G. Fan, X. Qu, G. Zhao, and W. Hua, 2017: Evolution of surface sensible heat over the Tibetan Plateau under the recent global warming hiatus. *Adv. Atmos. Sci.*, **34**, 1249-1262, https://doi.org/10.1007/s00376-017-6298-9.

Zhu, X., Y. Liu, and G. Wu, 2012: An assessment of summer sensible heat flux on the Tibetan Plateau from eight data sets. *Sci. China Earth Sci.*, **55**, 779–786, https://doi.org/10.1007/s11430-012-4379-2.